Karlsruhe Institute of Technology

FACULTY OF PHYSICS
Institute of Experimental Particle Physics (ETP)

Optimization of the Integral Measurement of the Electron Energy Loss Function at KATRIN

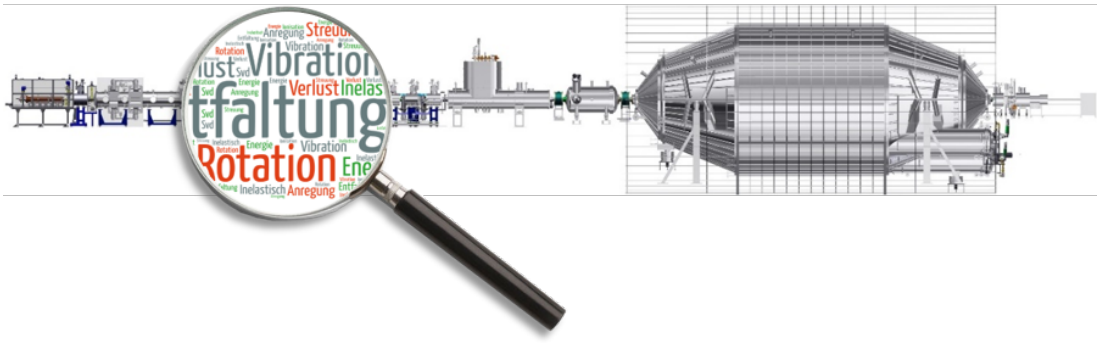

Master's Thesis
of

Karol Debowski

at the Institute of Experimental Particle Physics (ETP)

Reviewer:	Prof. Dr. G. Drexlin
Second Reviewer:	Prof. Dr. U. Husemann
Advisor:	M. Sc. L. Schimpf
Second Advisor:	Dr. Kathrin Valerius

April 9, 2018 – April 8, 2019

ERKLÄRUNG ZUR SELBSTSTÄNDIGKEIT

Ich versichere, dass ich diese Arbeit selbstständig verfasst habe und keine anderen als die angegebenen Quellen und Hilfsmittel benutzt habe, die wörtlich oder inhaltlich übernommenen Stellen als solche kenntlich gemacht und die Satzung des KIT zur Sicherung guter wissenschaftlicher Praxis in der gültigen Fassung vom 17.05.2010 beachtet habe.

Karlsruhe, den 08.04.2019, _____

Karol Debowski

Als Ansichtsexemplar genehmigt von

Karlsruhe, den 08.04.2019, _____

Prof. Dr. G. Drexlin

CONTENTS

1. Introduction **1**

I. Theoretical Background and Underlying Physics **3**

2. Neutrino Physics **5**
2.1. The History of Neutrino Physics 5
2.2. Neutrinos in the Standard Model 7
2.3. Neutrino Physics Beyond the Standard Model 8
2.4. Neutrino Mass Measurement 11
2.4.1. Indirect ν-Mass Measurement 12
2.4.2. Direct ν-Mass Measurement 14

3. The KATRIN Experiment **17**
3.1. Motivation for the KATRIN Experiment 17
3.2. The MAC-E Filter Principle 18
3.3. The KATRIN Experimental Setup 20
3.3.1. Source and Transport Section - STS 21
3.3.2. Spectrometer and Detector Section - SDS 25
3.4. KATRIN Rear Section E-Gun 27
3.4.1. Creation of Monoenergetic Electrons 27
3.4.2. The Optical System for E-Gun Illumination 29
3.5. Current Status and Milestones of the KATRIN Experiment 29

4. Energy Loss of Electrons in Tritium **31**
4.1. The Energy Loss Process 31
4.2. Energy Loss Models and Parameterizations 32
4.3. Energy Loss Measurement 34
4.3.1. Integral Measurements to Generate the Energy Loss Function 35
4.3.2. Deconvolution of the Energy Loss Function 36
4.3.3. Singular Value Decomposition 37
4.4. The KEloss Software Package 37
4.5. KATRIN Energy Loss Simulation Results 40

II. Energy Loss Simulations and Measurements **43**

5. Optimization of the Measurement Strategy **45**
5.1. The Simulation and Analysis Interface 45

5.2. Deconvolution Results for Default Settings . . . 48
5.3. Variation of Simulation Parameters . . . 49
5.3.1. Variation of the Overall Statistics . . . 50
5.3.2. Sensitive Region Investigation . . . 52
5.3.3. Non-Flat Measurement Time Distributions . . . 53
5.3.4. Variation of Voltage Steps in Scanning . . . 56
5.3.5. Interpolation of the Zero Column Density Measurement . . . 58
5.4. Summary of Different Optimization Approaches . . . 59

6. Energy Loss Measurement During the STS-IIIa Campaign **61**
6.1. Preparations for STS-IIIa . . . 61
6.2. STS-IIIa Setup . . . 63
6.2.1. E-Gun Characterization . . . 63
6.2.2. Fast Scanning Mode . . . 64
6.2.3. Simulations with STS-IIIa Settings . . . 66
6.3. Preliminary Energy Loss Results . . . 67
6.3.1. Analysis Strategy and Deconvolution Process . . . 67
6.3.2. Raw Data Analysis . . . 68
6.3.3. Data Post-Processing and Correction to Systematic Effects . . . 70
6.3.4. Deconvolution of Processed Data . . . 72
6.4. Conclusions from STS-IIIa . . . 74

7. Conclusion and Outlook **75**

A. Appendix **79**
A.1. Parameters in Default Setup Analysis . . . 79
A.2. Energy Loss Model Comparison to Deconvolution . . . 79
A.3. NoiseEater . . . 80
A.4. Optical Test Setup . . . 80
A.5. Time Synchronization . . . 80
A.6. Different Tested Measurement Time Distributions . . . 80

Bibliography **87**

LIST OF FIGURES

2.1. Standard Model of Particle Physics 7
2.2. Neutrino Mass Hierarchies 12
2.3. Feynman Graphs of Double-β Decays 13
2.4. Beta Spectrum of Tritium 15

3.1. Schematic Drawing of a MAC-E Filter 18
3.2. The Spectrometer Transmission Function 20
3.3. Overview of the Full KATRIN Beamline 20
3.4. Schematic View of the Rear section 21
3.5. Schematic View of the WGTS 22
3.6. Schematic View of the DPS 23
3.7. Schematic View of the CPS 24
3.8. CAD Drawing of the Main Spectrometer 25
3.9. Schematic View of the Focal Plane Detector System 26
3.10. Electron Acceleration in the E-Gun 28

4.1. Energy Loss Models 33
4.2. Simulated Response and Scattering Functions 36
4.3. Deconvolution of Energy Loss Function 37
4.4. Ensemble Test of a Deconvolved Energy Loss Function 40
4.5. Previous KATRIN Energy Loss Deconvolution Simulations 41

5.1. Schematic View of the Merging Process During Simulation 46
5.2. Energy Loss Deconvolution with Error Band 48
5.3. Ensemble Test of Simulations under Default Settings 49
5.4. Statistical Variations of Energy Loss Function Deconvolution 50
5.5. Neutrino Mass Square Fits for High and Low Statistics 51
5.6. Influence of Overall Statistics on Fit Results 51
5.7. Search for Sensitive Regions in Response Functions - 1 52
5.8. Search for Sensitive Regions - 2 53
5.9. Focused Measurement Time Distribution - 1 55
5.10. Focused Measurement Time Distribution - 2 56
5.11. Influence of Voltage Step Size on Fit Results 57
5.12. Ensemble Test Results for Constant Measurement Time 58
5.13. Results for the Best Combination of Voltage Steps and Statistics 59
5.14. Influence of Interpolation on the Deconvolution 60

6.1. Effect of the NoiseEater System 62
6.2. Column Densities Comparison 66
6.3. Ensembletest for Different Column Densities 66

6.4. Raw Data Response and Scattering Functions 68
6.5. First Deconvolution of Raw Data 69
6.6. Diode Signal Correlation to Electron Rate 70
6.7. Time Synchronization in STS-IIIa Data 71
6.8. Influence of Pile-Up Correction 72
6.9. Corrected STS-IIIa Data 72
6.10. Deconvolution with Data Corrections 73

A.1. Energy Loss Model Comparison to Deconvolution 79
A.2. The NoiseEater Hardware 80
A.3. Optic Box Test Setup 81
A.4. Time Synchronization Problem 81
A.5. Tested Setups and Results - A-D 82
A.6. Tested Setups and Results - E-H 83
A.7. Tested Setups and Results - I-K+ 84

LIST OF TABLES

2.1. Neutrino Oscillation Parameters 11

4.1. Parameters for Response Function Simulation 39

5.1. Ensemble Test Results for 10^6 and 10^8 Electrons in every Voltage Step . . . 51

6.1. Numbers of Runs During STS-IIIa 68

A.1. Parameters in Default Setup Analysis 79
A.2. NoiseEater Settings 80
A.3. Different Tested Settings 85

Chapter 1

INTRODUCTION

The standard model of particle physics describes the elementary particles that make up matter and their interactions. One of the most fundamental properties of any particle is its mass. Almost all of the known particles have a very precisely calculated and the experimentally proven mass, except for the neutrinos. A long time since its first postulation almost 90 years ago and experimental proof of existence in the 1950s, the neutrino was assumed to be massless until the late 1990s. After the observation of neutrino flavor oscillations, it was proven that the three mass eigenstates of neutrinos have different mass eigenvalues, yielding a non-vanishing effective mass also for the electron (anti)neutrino. From oscillation experiments, the two independent mass-square differences and three mixing angles can be measured precisely, but still these cannot address the absolute mass scale. Hence, one of the key open questions in physics beyond the standard model is related to neutrino masses. The determination of the absolute mass scale of neutrinos could bring new insights into cosmology as well as particle and astroparticle physics.
A measurement of the effective electron antineutrino mass can be performed by precise investigation of the kinematics of weak decays (notably, β-decay and electron capture). The neutrino mass squared is one of the parameters in the energy spectrum of the electrons produced in these decays. Therefore, measuring the spectrum at great accuracy is a means to solve the mystery of the neutrino mass.
Today's leading experiment for the direct neutrino mass measurement is the **KA**rlsruhe **TRI**tium **N**eutrino experiment (KATRIN), which aims to measure the electron antineutrino mass with a sensitivity of

$$m_\nu = 200\,\mathrm{meV}$$

at 90 % confidence level. This is done by investigating the endpoint region of the β-spectrum of tritium with an electromagnetic spectrometer. To achieve this low mass sensitivity, a MAC-E filter is used to measure the integral β-energy spectrum of tritium. In order to perform a measurement yielding the desired neutrino mass sensitivity, all systematic effects need to be known and understood very precisely.
One of the dominant systematic effects is the energy loss of the emitted electrons by scattering off tritium molecules in the source. Any energy losse occurring between the decay and passing the analyzing plane of the spectrometer causes a distortion of the recorded β-spectrum. Therefore a detailed measurement of the scattering processes inside the tritium source is needed, to which purpose a measurement and deconvolution approach was developed in the KATRIN design report [KAT05] and subsequent work (see e.g. Hannen et al. [HHW$^+$17]). As shown by N. Trost [Tro18], the measurement principle still needs to be improved to meet the sensitivity requirements of KATRIN. Therefore an optimization of the measurement method with respect to measurement time, precision and the given

hardware limitations is needed.
This thesis is focused on the optimization by simulations and by the first analysis of measurement data taken with the KATRIN source filled with deuterium. The electrons for this measurement are produced using an e-gun consisting of a photocathode and an acceleration chain. This instrument follows a novel concept that had not been used in KATRIN before and is put to work and characterized for the first time during the STS-IIIa measurement campaign in fall of 2018.

Chapter 2 briefly summarizes the historical development of neutrino physics, and explains its most important concepts. After this introduction to neutrino physics, the approaches of direct and indirect neutrino mass measurement are explained.
Chapter 3 motivates and describes the KATRIN experiment. From the working principle of the electromagnetic spectrometer, through the specification of the overall experimental setup to the more detailed consideration of the rear section and the e-gun used as electron source for energy loss measurements.
Chapter 4 discusses the process of energy loss of electrons in tritium, and the measurement and deconvolution method of this important systematic. In this chapter, also the existing energy loss models are briefly described, as well as the software package used for the simulations in this thesis and the latest investigations of the deconvolution method for the energy loss function, which are the basis of this work.
In **Chapter 5** the results of the optimization simulations are presented. After tracing the default strategy proposed in the KATRIN design report, different investigations to optimize this measurement are presented here. Varying the parameters of the simulation shows that an increase of the overall statistics in the measurement does not yield a significant improvement, and thus a different approach of optimization is needed and found in the finer scanning of the response functions with voltage steps below 0.1 V. This method was tested in the STS-IIIa measurements.
In **Chapter 6** the STS-IIIa e-gun characterization and energy loss measurements are briefly described, discussing difficulties occurring in the measurement campaign, and solutions worked out to amend these problems. Further, preliminary results of deconvolving the measured data are presented, including a discussion of systematic effects and corrections to them.
In **Chapter 7** the results of this thesis are summarized and an outlook to future energy loss measurements is given.

Part I.

Theoretical Background and Underlying Physics

Chapter 2

INTRODUCTION INTO THE BASIC CONCEPTS OF NEUTRINO PHYSICS

After its postulation in 1930 [PKW64] and its first experimental detection in 1956 [RC53], the neutrino gained more and more attention in the scientific investigation of the Universe. Physicists from different fields of research are interested in further knowledge about these 'ghost particles', as they can provide important information about the origin of the Universe. Therefore, the properties of neutrinos are important for cosmology and astroparticle physics as well as for understanding Dark Matter, which makes up about 27 % of the Universe[1].
One of the major challenges of today's neutrino physics is to measure the neutrino mass. Many observations in high-energy particle physics can be described by massless neutrinos, but today we know that although the mass of neutrinos is very small, it is finite[2]. Until today, only an upper limit for the mass could be established, yielding to neutrinos being the last particles in the standard model with unknown mass, as shown in Fig. 2.1.
In this chapter, the historical development of neutrino physics will be briefly summarized in Sec. 2.1. In the following Sec. 2.2 and 2.3 a short introduction about neutrino physics in the standard model will be provided, as well as the physical background of the beyond standard model theory of neutrino oscillations, which lead to the introduction of massive neutrinos. This chapter will close with the description of indirect and direct neutrino mass measurements. This introduction of direct neutrino mass measurements is the connection to the KATRIN experiment, with its primary goal of measuring the mass of the electron antineutrino.

2.1. The History of Neutrino Physics

This section aims to give a brief historical overview of the neutrino, from its first postulation in 1930 to the discovery of the third and last neutrino flavor in 2001, completing the leptons in the standard model (see Fig. 2.1).

Postulation

One of the first steps into modern particle physics was the discovery of the electron by Joseph J. Thomson in 1897 [Tho97]. Two years later, in 1899, Ernest Rutherford separated

[1] Compared to roughly 5 % of visible matter, this is about five times more.
[2] The non-vanishing neutrino mass was experimentally proven by the observation of neutrino flavor oscillations in the 1990s [Kaj99].

the radioactive α- and β-decay by investigating the penetration and ionization properties of radioactive rays [Rut99], proving that β-radiation is made of electrons.
Further investigations of the emitted β-electrons by James Chadwick in 1914 did not show the expected discrete energy spectrum, but a continuous distribution instead [Cha14]. As in this time β-disintegration of a nucleus was assumed to be a two-body decay, where the nucleus emits only an electron according to

$$\mathrm{X} \rightarrow \mathrm{Y} + \mathrm{e}^{-}. \tag{2.1}$$

Therefore the measurement result seemingly violated energy and momentum conservation. This problem was solved by Wolfgang Pauli in 1930 by postulating the existence of a new particle. He introduced a particle with no electrical charge and a spin of $\hbar/2$ [PKW64][3]. This *Neutron*, as he called it before the discovery of the nucleon we nowadays know as neutron, was assumed to also take part in the process of β-decay, carrying a certain energy and therefore allowing the continuous energy spectrum in a three-body decay, according to

$$\mathrm{X} \rightarrow \mathrm{Y} + \mathrm{e}^{-} + \nu. \tag{2.2}$$

A quantitative calculation of this process was done by Enrico Fermi in the following years [Fer34], which were fundamental for the later development of the weak interaction.
Following Fermi's approach, Bethe and Peierls estimated the theoretical cross section of this new particle with atomic nuclei to be $\sigma \approx 10^{-44}\,\mathrm{cm}^2$ [BP34]. Due to this tiny cross section, it took scientists over 20 years to experimentally prove the existence of this particle, and even longer to detect the muon and tau neutrino.

Discovery of Neutrino Flavors

In the standard model three flavors of neutrinos and their antineutrinos are described, namely the electron, muon and tau neutrino, ν_e, ν_μ, ν_τ and $\bar{\nu}_\alpha$, respectively (see Fig. 2.1). Taking into account lepton-number conservation for all flavors separately, it can be simply derived, that the neutrino emitted in β-decays must be the electron antineutrino $\bar{\nu}_e$.
The existence of this predicted particle was proven in 1956 by Clyde Cowan and Frederick Reines [RC53]. The underlying reaction in their experiment was an inelastic scattering process between a proton and an electron antineutrino, producing a neutron and a positron, also referred to as inverse β-decay,

$$\bar{\nu}_\mathrm{e} + \mathrm{p} \rightarrow \mathrm{n} + \mathrm{e}^{+}. \tag{2.3}$$

This experiment used a nuclear reactor as a neutrino source, providing a much larger neutrino flux compared to radioactive sources, which is required for high statistics. Due to the small cross section, two vessels with a total filling of 200 l of water were used as proton target. The positrons created in this reaction annihilate with an electron from the water and thus create two back-to-back photons of 511 keV each, which are detected by scintillating detectors.
Investigating pion decays at Brookhaven National Laboratory in the early 1960s, Ledermann, Schwartz and Steinberger [DGG+62] found that neutrinos produced in the decays

$$\pi^{+} \rightarrow \mu^{+} + \nu_\mu \text{ and } \pi^{-} \rightarrow \mu^{-} + \bar{\nu}_\mu$$

can only interact with matter producing muons in the final state:

$$\nu_\mu + \mathrm{n} \rightarrow \mathrm{p} + \mu^{-} \text{ and } \bar{\nu}_\mu + \mathrm{p} \rightarrow \mathrm{n} + \mu^{+}.$$

[3] *"Today I have done something which you never should do in theoretical physics. I have explained something which is not understood by something which can never be observed!"*, W. Pauli [Pov15].

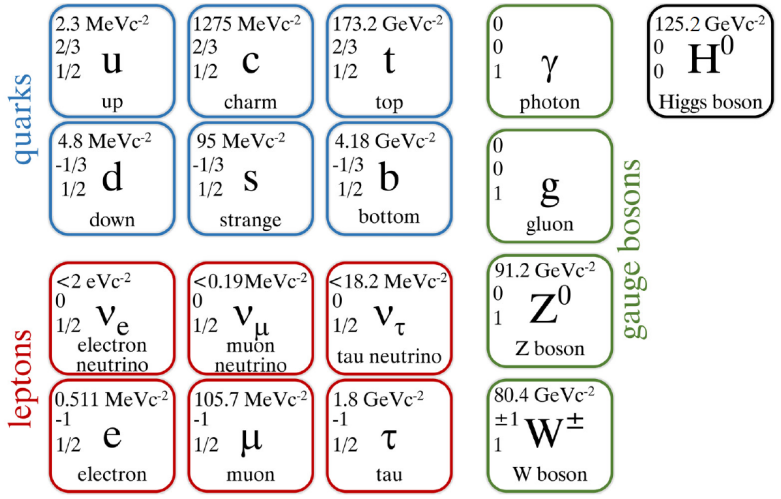

Figure 2.1.: Standard Model of Particle Physics: This graphic shows the 18 basic elementary particles of the standard model of particle physics, including six quarks, six leptons, five gauge bosons and the Higgs boson. The particles in the graphic are shown grouped into quarks (blue), leptons (red) and gauge bosons (green). The first value given in the upper-left corner denotes the mass of the particle, the second and third values denote the electrical charge in units of the elementary charge and the particles spin in units of $\hbar$, respectively. Graphic adapted from [Sch16].

The fact that only muons are produced in the final states shows that these particles can not be the same as the ones produced in the β-decay, proving the existence of a second family of neutrinos. According to their interaction with muons, the second generation neutrinos are dubbed muon neutrinos. The three scientists were awarded the Nobel prize in physics in 1988 *for the neutrino beam method and the demonstration of the doublet structure of the leptons through the discovery of the muon neutrino* [Noba].
In 2001 the τ-neutrino was detected, by investigating the D_S meson decay

$$D_S \rightarrow \tau + \bar{\nu}_\tau$$

at Fermilab Tevatron by the DONUT[4] Collaboration (Kodama et al., [KUA+01]).

2.2. Neutrinos in the Standard Model

In particle physics, the three fundamental interactions (electromagnetic, weak and strong interaction) are well described in the standard model of particle physics. This theory describes the most fundamental and elementary particles as well as the interactions between these particles [PHM17, Pov15].
After experimentally proving the existence of the Higgs boson at CERN in 2012 [A+12], the standard model is assumed to be complete.
Important for the interactions of particles with neutrinos is the weak interaction, with its exchange particles, the $W^\pm$ and Z^0 bosons [Pov15]. The weak interaction is the only one of the three fundamental forces that can change flavors of quarks and leptons.
Fig. 2.1 shows the elementary particles of the standard model, namely six quarks, six leptons (including neutrinos), as well as five types of gauge bosons describing the interaction between these particles and the Higgs boson generating masses.

Neutrinos are electrically neutral particles, and thus cannot interact via electromagnetic

[4] **D**irect **O**bservation of the **NU** **T**au

interaction, like charged leptons, but only through weak interaction. In the theory of weak interaction the concept of handedness is introduced, which is the direction of the particle's spin in relation to its momentum, and makes the bosons couple only to left-handed particles and right-handed antiparticles (for neutrinos ν_L and $\bar{\nu}_R$). Assuming that neutrinos are massless, and thus travel at the speed of light, it is not possible for neutrinos in the standard model to change their handedness, according to the probability of such a changing process being

$$P(L \to R) \propto 1 - \beta \text{ [Pov15].} \tag{2.4}$$

The left-handedness of neutrinos was experimentally proven by [GGS58]. The Goldhaber experiment measured the helicity of neutrinos to be -1.0 ± 0.3.

2.3. Neutrino Physics Beyond the Standard Model

In the late 1990s, the effect of neutrino flavor transformation was discovered and investigated by the Kamiokande experiment as well as the SNO Collaboration [Kaj99, A$^+$01], after the flux of solar neutrinos was measured to be a factor of 3 less than predicted by solar models [DHH68]. From the oscillation parameters measured by SNO, a non-vanishing neutrino mass can be extracted, as mass differences between the three neutrino states are needed to make flavor oscillations possible. These neutrino masses contradict the standard model assumption of massless neutrinos, opening the way to new physical theories and research beyond the standard model.
This section describes the beyond standard model effect of neutrino oscillations, that led to the discovery of the non-vanishing neutrino mass that is to be determined by the KATRIN experiment.

Solar Neutrino Problem

By investigating the solar neutrino flux in the 1960's, Ray Davis found in the Homestake experiment, that the detected solar neutrino flux did not match the solar model predictions [DHH68].
Neutrinos coming from the Sun entered an underground detector which was made of a large tank filled with $390\,\mathrm{m}^3$ tetrachloroethylene. From the reaction

$$\nu_e + {}^{37}\mathrm{Cl} \to {}^{37}\mathrm{Ar} + \mathrm{e}^- \tag{2.5}$$

Davis was able to reconstruct the neutrino flux by extracting the small amount of the produced ^{37}Ar and measuring the decay rate of this unstable isotope. After 24 years of operation the Homestake experiment reported a measured neutrino flux of [DHH68]

$$\Phi_{\nu_e} = (2.55 \pm 0.25)\ \text{SNU}, \tag{2.6}$$

which is only about one third compared to the expected flux of (7 ± 1.5) SNU[5] [Bah64].
After excluding all systematic effects, still not finding a reason for the discrepancy, some physicists began to doubt fundamental concepts and models due to this significant mismatch between theory and experiment. After further investigation, it turned out, neither the solar model is wrong, nor do neutrinos totally disappear, but in fact the measured flux is correct. As Eq. (2.5) and lepton-flavor conservation indicate, the experiment is only sensitive to electron neutrinos, and not to the two other flavors. If solar neutrinos happen to change their flavor during their travel to the Earth, they could not be detected with this method. As an approach to describe the lack of measured neutrinos, the theory of neutrino oscillations was developed.
Davis was rewarded the 2002 Nobel prize in physics *for pioneering contributions to astrophysics, in particular for the detection of cosmic neutrinos* [Nobb].

[5]SNU: Solar Neutrino Unit, one SNU is equal to a Neutrino flux producing 10^{-36} captures per target atom per second [BEL04].

Mass and Flavor Eigenstates

The first important ansatz for the theory of neutrino oscillations is that the observed neutrino states (ν_e, ν_μ and ν_τ) are not the mass eigenstates of the wavefunction, but can be described as a linear superposition of three mass eigenstates [Zub12]:

$$|\nu_\alpha\rangle = \sum_{i=1}^{3} U_{\alpha i} |\nu_i\rangle \tag{2.7}$$

In this equation, ν_α describes the flavor eigenstates and ν_i the mass eigenstates. The mixing coefficients $U^*_{\alpha i}$ are the elements of the PMNS[6] matrix, describing a rotation between the bases of flavor and mass eigenstates. For the full description including three flavors, three mixing angles Θ_{ij} and one CP-violating phase $e^{-i\delta}$ are needed as free parameters. This yields a matrix of the following form, where c_{ij} and s_{ij} denote $\cos(\Theta_{ij})$ and $\sin(\Theta_{ij})$ respectively:

$$\begin{aligned} U &= \begin{pmatrix} 1 & 0 & 0 \\ 0 & c_{23} & s_{23} \\ 0 & -s_{23} & c_{23} \end{pmatrix} \begin{pmatrix} c_{13} & 0 & s_{13}e^{-i\delta} \\ 0 & 1 & 0 \\ -s_{13}e^{-i\delta} & 0 & c_{13} \end{pmatrix} \begin{pmatrix} c_{12} & s_{12} & 0 \\ -s_{12} & c_{12} & 0 \\ 0 & 0 & 1 \end{pmatrix} \\ &= \begin{pmatrix} c_{12}c_{23} & c_{13}s_{12} & s_{13}e^{-i\delta} \\ -c_{23}s_{12} - s_{13}s_{23}e^{-i\delta} & c_{12}c_{23} - s_{12}s_{13}s_{23}e^{-i\delta} & c_{13}s_{23} \\ s_{12}s_{23} - c_{12}c_{23}s_{13}e^{-i\delta} & -c_{12}s_{23} - c_{23}s_{12}s_{13}e^{-i\delta} & c_{13}c_{23} \end{pmatrix}. \end{aligned} \tag{2.8}$$

When created in a weak-interaction process, neutrinos are in a well-defined flavor eigenstate, i.e. a well-defined mixing of the three mass eigenstates. The time evolution of a certain state $|\psi\rangle$ is given by

$$|\psi(t)\rangle = e^{-iHt} |\psi(0)\rangle , \tag{2.9}$$

where H denotes the Hamiltonian. Applying this rule to the superposition of the three mass eigenstates yields a time-evolution of the neutrino-flavor state given by

$$|\nu_\alpha(t)\rangle = e^{-iHt} |\nu_\alpha\rangle = \sum_{j=1}^{3} e^{-\frac{i}{\hbar}E_j t} U_{\alpha j} |\nu_j\rangle , \tag{2.10}$$

where $E_j = \sqrt{m_j^2 + p_j^2}$ [7] is the energy of the mass eigenstate j [A+18a].

In quantum mechanics, the probability to measure some state $|\psi'\rangle$ after initiating a state $|\psi\rangle$ with the time-evaluation operator T is given by

$$P(\psi \to \psi') = \left|\langle\psi'| T |\psi\rangle\right|^2 . \tag{2.11}$$

Applying this relation to the neutrino flavor states in Eq. (2.10) yields

$$P(\nu_\alpha \to \nu_\beta) = \left|\langle\nu_\beta| e^{-iHt} |\nu_\alpha\rangle\right|^2 = \left|\sum_{j=1}^{3} \langle\nu_i| U_{\beta j} e^{-\frac{i}{\hbar}E_j t} U^*_{\alpha j} |\nu_j\rangle\right|^2 , \tag{2.12}$$

for a detailed derivation and calculation see e.g. [Zub12, Ber14, Pov15].

[6] Named after Pontecorvo, Maki, Nakagawa and Sakata

[7] In this thesis, natural units are used with $c = 1$ and $\hbar = 1$.

Two Flavor Oscillations

In the case of only two neutrino flavors the transition between mass and flavor eigenstates can be written with a simplified 2×2 PMNS matrix, with the resulting mixing:

$$\begin{pmatrix} |\nu_e\rangle \\ |\nu_\mu\rangle \end{pmatrix} = \begin{pmatrix} \cos(\Theta_{12}) & \sin(\Theta_{12}) \\ -\sin(\Theta_{12}) & \cos(\Theta_{12}) \end{pmatrix} \begin{pmatrix} |\nu_1\rangle \\ |\nu_2\rangle \end{pmatrix}. \tag{2.13}$$

This limited case of only two neutrino flavors simplifies the calculation of the transition probability from an initially created electron neutrino to a detected muon neutrino, i.e. the probability of a muon neutrino appearing or an electron neutrino disappearing

$$P(\nu_e \to \nu_\mu) = \left| \sum_{j=1}^{2} U_{\nu_\mu j}\, \mathrm{e}^{-\frac{i}{\hbar} E_j t}\, U^*_{\nu_e j}\, |\nu_j\rangle \right|^2 = \sin^2(2\Theta_{12}) \sin^2\left(\frac{E_1 - E_2}{2\hbar} t\right), \tag{2.14}$$

according to Eq. (2.12). As can be seen in Eq. (2.14), an oscillation in time with the period of $\frac{E_1 - E_2}{2\hbar}$ occurs. Taking into account that $\sum_\psi P(\nu_\mathrm{e} \to \psi) = 1$ and only oscillations between neutrinos are possible, yields $P(\nu_\mathrm{e} \to \nu_\mathrm{e}) = 1 - P(\nu_\mathrm{e} \to \nu_\mu)$.
More fundamental than the energy difference in Eq. (2.14) are characteristic properties such as the masses of the two particles. Assuming highly relativistic particles, the mass difference can be calculated as

$$E_1 - E_2 = \frac{m_2^2 - m_1^2}{2E} =: \frac{\Delta m_{21}^2}{2E}. \tag{2.15}$$

Further, the time variable can be replaced by the propagation length[8] L through $L = t \cdot c$. To express the results in numbers, $\hbar c = 1.97 \times 10^{-11}\,\mathrm{MeV\,cm}$ is used, as well as the difference of squared masses Δm_{21}^2 in eV^2, the neutrino energy in GeV and the length L in km.
The transition probability from Eq. (2.14) can now be expressed as

$$P(\nu_e \to \nu_\mu) = \sin^2(\Theta_{12}) \sin^2\left(1.27 \frac{\Delta m_{21}^2}{E} L\right) \tag{2.16}$$

With this formula, it is possible to calculate the expected rate of electron neutrinos arriving at the detector. From a measurement of the transition probability one can therefore calculate the difference of neutrino mass squares between different flavors. The relation in Eq. (2.16) is only valid for a well-defined source and detector, and needs additional terms describing the source and detector properties as e.g. finite detector and source volume.

Measurements of Δm_{ij}^2 and the Mixing Angles Θ_{ij}

The first experimental results for Δm_{23} and Θ_{23} were delivered by the Super-Kamiokande collaboration in 1998 [Kaj99]. Measuring atmospheric muon neutrinos, created in the decay of pions produced by cosmic rays scattering off nucleons in the upper atmosphere,

$$\pi^+ \to \mu^+ + \nu_\mu \tag{2.17}$$
$$\pi^- \to \mu^- + \bar{\nu}_\mu \tag{2.18}$$

As the produced muon or antimuon further decay into an electron or a positron and two neutrinos, respectively

$$\mu^+ \to \bar{\nu}_\mu + \mathrm{e}^+ + \nu_\mathrm{e} \tag{2.19}$$
$$\mu^- \to \nu_\mu + \mathrm{e}^- + \bar{\nu}_\mathrm{e}, \tag{2.20}$$

[8] Experimentally this is the distance from the source, where the neutrinos are produced, to the detector.

Table 2.1.: Today's neutrino oscillation parameters assuming a 'normal' mass hierarchy ($m_1 < m_2 < m_3$), see [Oli16].

Parameter	Best Fit	3σ Range
Δm^2_{21}	$7.37 \times 10^{-5}\,\mathrm{eV}^2$	$6.93 \times 10^{-5}\,\mathrm{eV}^2$ to $7.97 \times 10^{-3}\,\mathrm{eV}^2$
$\lvert\Delta m^2_{31}\rvert$	$2.46 \times 10^{-3}\,\mathrm{eV}^2$	$2.33 \times 10^{-3}\,\mathrm{eV}^2$ to $2.60 \times 10^{-3}\,\mathrm{eV}^2$
$\sin^2\Theta_{12}$	0.297	$0.250 - 0.354$
$\sin^2\Theta_{23}$	0.437	$0.379 - 0.616$
$\sin^2\Theta_{13}$	0.0214	$0.0185 - 0.0246$

the fraction of produced muon and electron neutrinos is $N_{\nu_\mu}/N_{\nu_e} = 2$. Detecting the produced leptons during the interaction with a set of photo multiplier tubes using the emitted Cherenkov light [Kaj99] allowed to reconstruct the incoming direction of the neutrinos. This also allowed the calculation of the oscillation length of the incoming neutrinos. Neutrinos detected as coming from above pass only the atmosphere, whereas neutrinos from below pass the atmosphere and the entire diameter of the Earth. Measuring the rate difference between neutrinos coming directly from the atmosphere above the detector and the rate of neutrinos measured with a direction coming from below the detector and thus crossing the Earth, the Super-Kamiokande collaboration was able to reconstruct the oscillation length and further the mass difference and mixing angles. In experiments like Super-Kamiokande and SNO, also the mixing angle Θ_{12} was measured and the mass difference between the squared mass eigenvalues of ν_1 and ν_2, Δm^2_{21}, could be determined [Kaj99, A$^+$01].
Further, more precise measurements were performed in reactor and accelerator experiments, where the energy of the neutrinos is known to a better accuracy. The second big advantage of reactor experiments, compared to solar neutrino experiments, is the precise knowledge of the neutrinos travel distance from the production site to the detector, i.e., the oscillation length. The SNO and Super-Kamiokande experiments reported the values listed in Tab. 2.1 for the neutrino oscillation parameters. The values in Tab. 2.1 are valid under the assumption of the normal mass hierarchy (see following section). Assuming inverted mass hierarchy, the values for Δm^2_{31} and the angles Θ_{23} and Θ_{13} would be slightly different.

As shown in Tab. 2.1, only the absolute value of Δm^2_{32} is known. As the sign could be either positive or negative, there are two possible mass hierarchies, as shown in Fig. 2.2. The first one, what is called the normal mass hierarchy, assumes $m_1 < m_2 < m_3$, where the inverted mass hierarchy assumes a negative difference of squared mass Δm^2_{23}, leading to $m_3 < m_1 < m_2$.
To measure a precise squared mass difference and mixing angle for two neutrino flavors, the MSW-effect[9] needs to be taken into account. This effect describes an additional potential on electron neutrinos, due to a surrounding, non-vanishing electron density. This effect can be explained with weak interaction charge-current reactions [MS86, Wol78].

2.4. Neutrino Mass Measurement

The above-mentioned oscillation experiments are only sensitive to differences of squared masses, and not to the absolute mass scale of neutrinos. Therefore another method is needed in order to experimentally determine the mass of a neutrino state.
There are two approaches of measuring the neutrino mass: the indirect mass measurement described in Sec. 2.4.1 and the direct mass measurement described in Sec. 2.4.2. As these two approaches have a different physics background they are also sensitive to different observable quantities. Direct neutrino mass measurement (performed for instance at

[9] Named after Mikheyev, Smirnov and Wolfenstein

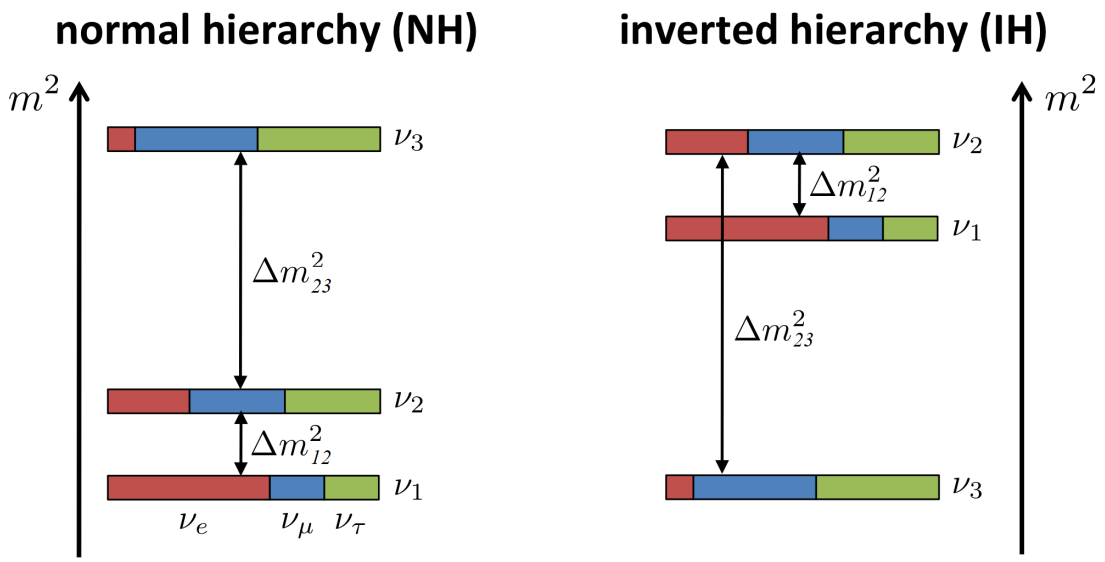

Figure 2.2.: Neutrino Mass Hierarchies: As the sign of Δm^2_{23} is not known, there are two possibilities for the neutrino mass hierarchy. **Left:** The normal hierarchy with $m_1 < m_2 < m_3$. **Right:** the inverted hierarchy with $m_3 < m_1 < m_2$. For both orderings, the absolute mass scale is still unknown. Graphic adapted from [A+16a].

KATRIN) aims to determine the effective mass of flavor eigenstates, whereas indirect mass measurements are sensitive to the sum of all mass eigenstates.

2.4.1. Indirect Neutrino Mass Measurements

Indirect neutrino mass determination is strongly model dependent, yielding the determined neutrino mass is only correct, if the underlying model is. Today there are two approaches for indirect neutrino mass inference: the search for neutrinoless double beta decay ($0\nu\beta\beta$) and the determination of m_ν via observational cosmology.

Neutrinoless Double Beta Decay

Unlike the usual β-decay, where an electron and an antineutrino are emitted, the double-β decay creates two of each of them. First discovered in 1987 by Elliott, Hahn and Moe by investigating the decay process of ^{82}Se [EHM87], the double-β decay was found in the following processes:

$$2\nu\beta^+\beta^+ : \ {}^{A}_{Z}\mathrm{X} \rightarrow {}^{A}_{Z-2}\mathrm{X} + 2\mathrm{e}^+ + 2\nu_\mathrm{e} \tag{2.21}$$

$$2\nu\beta^-\beta^- : \ {}^{A}_{Z}\mathrm{X} \rightarrow {}^{A}_{Z+2}\mathrm{X} + 2\mathrm{e}^- + 2\bar{\nu}_\mathrm{e} \tag{2.22}$$

These processes occur only very rarely, as the half-life time of ^{48}Ca, for example, is in the order of 6×10^{19} years [A+16c].
The most suitable isotopes to measure double-β decays are the ones where the single-β decay is forbidden due to energy conservation. As can be derived from the Bethe-Weizsäcker formula, there are some isotopes for which a daughter nucleus would have a higher energy after a β-decay process, which can be explained with the pairing term which can be positive, negative or zero in dependence of the number of protons and neutrons in the nucleus[10]

[10] For an even number of protons and an even number of neutrons the pairing term becomes positive, for odd-odd negative, and for odd-even or even-odd it is 0.

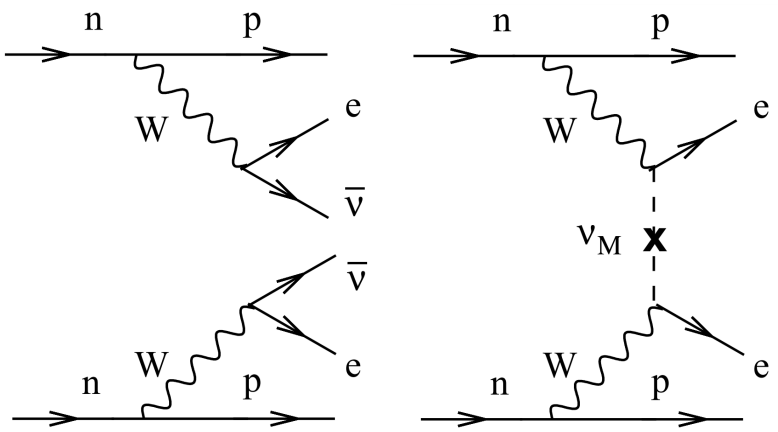

Figure 2.3.: Feynman Graphs of Double-β Decays: This graphic shows the two possibilities for double-β decays. **Left:** the usual 2νββ decay emitting two neutrinos, **Right:** the neutrinoless double-β decay (0νββ), assuming Majorana type neutrinos annihilating at the vertex. Graphic from [AEE08].

[Pov15]. These nuclei can only decay with two simultaneously emitted electrons/positrons with the double-β decay, without being in the forbidden state of a nucleus with higher binding energy.
Only 35 isotopes are known to have these forbidden single-βdecay daughter isotopes.

By detecting the 0νββ decay and measuring its decay rate, the so-called Majorana mass can be determined as

$$m_{\mathrm{ee}} = \left| \sum_{i=1}^{3} U_{ei}^2 m_i \right| \propto \Gamma_{0\nu\beta\beta}, \tag{2.23}$$

being proportional to the neutrinoless double-β decay probability $\Gamma_{0\nu\beta\beta}$ [VEŠ16]. With no neutrino emitted, the spectrum of the neutrinoless double-β decay is a sharp line located two neutrino masses above the endpoint energy of the double-β spectrum. The important difference compared to direct neutrino mass measurement is the coherent sum in this case, meaning that the effective mass can be vanishing, depending on the phase relations in the elements of the PMNS matrix U_{ei}.
Despite long-standing experimental efforts, 0νββ has remained undetected as of yet. The GERDA[11] experiment thus constrained the Majorana mass of the electron-neutrino to an upper limit of [A+13]

$$m_{\mathrm{ee}} < 0.2 \text{ to } 0.4\,\mathrm{eV},\ 90\,\%\,\mathrm{CL}.. \tag{2.24}$$

Cosmological Observations and Model Comparison

Investigations of cosmic microwave background (CMB) can also provide information about the neutrino mass. Neutrinos played a significant role in the formation of the Universe's structure, as they are the major contribution to the amount of fermionic matter in the Universe. The structures we observe today evolved from fluctuations in the energy density in the early Universe, that can be measured in the temperature anisotropy of the CMB. This anisotropy is affected by the mass of neutrinos. Today's cosmological models use the sum of all neutrino mass eigenvalues as a parameter

$$M_\nu = \sum_i m_i. \tag{2.25}$$

[11] **GER**manium **D**etector **A**rray for search for neutrinoless double-β decay. Experiment performed at Gran Sasso National Laboratory.

Studying the CMB anisotropies, experiments like WMAP or Planck[12] [Ade14] can investigate this sum, and thus with the mass differences from oscillation experiments determine the individual masses of the m_i, i.e. also the effective masses of the individual flavor eigenstates of neutrinos, using Eq. (2.10).
The most recent results from Planck data analysis yields constraint on the sum of neutrino masses of [A$^+$18b]

$$M_\nu \leq 0.12\,\mathrm{eV}. \tag{2.26}$$

As mentioned already, the largest uncertainty on cosmological neutrino mass measurement is the uncertainty of the underlying model and the data sets combined in the analysis, which is the reason why the Particle Data Group does not accept these results as neutrino mass limit [Oli16].

2.4.2. Direct Neutrino Mass Measurements

A model-independent way of measuring the neutrino mass is introduced by direct neutrino mass measurements. This concept, which is also used in the KATRIN experiment, uses the relativistic energy-momentum relation and the equivalence of mass and energy:

$$E = \sqrt{m^2 + p^2}, \tag{2.27}$$

where E, m and p are denoted in natural units. Direct ν-mass measurements usually, also in the case of KATRIN, work with β-emitters. The energy of the emitted electron is measured very precisely close to the endpoint, where the rate is low, and small spectral deformations due to the neutrino mass can be spotted well. As the total energy of the electron and the neutrino is known, measuring the energy spectrum of the electron gives us information about the energy spectrum of the neutrino. With maximum electron energy, the neutrino carries the least possible amount of energy, which can be translated directly into its rest mass via Eq. (2.27). In the case of tritium, the spectrum is shown in Fig. 2.4. The difference between the spectrum with and without non-vanishing neutrino mass does not show any large difference along most of its energy range. Only the endpoint region exhibits a noticeable imprint.
The main aspect about direct neutrino mass measurement is energy conservation. If a nucleus decays via β-decay, the electron and the neutrino can have a certain amount of energy, which corresponds to the mass difference between mother and daughter molecule

$$E_\mathrm{e} + E_\nu = M_i - M_f, \tag{2.28}$$

where the indices i and f denote the initial and final nucleus, respectively. From this relation a maximum electron energy can be derived using Eq. (2.27):

$$E_e^\mathrm{max} = \frac{M_i^2 + m_e^2 - (M_f + m_\nu)^2}{2M_i} \approx M_i - M_f - m_\nu \tag{2.29}$$

This approximation can be assumed, as the masses of the initial and final molecules are large enough to neglect the recoil, also we can assume the neutrino to be created at rest with no kinetic energy.
This method measures the incoherent sum of mass eigenstates

$$m(\nu_\mathrm{e})^2 = \sum_i \left|U_{\mathrm{e}i}^2\right| m(\nu_i)^2. \tag{2.30}$$

This yields a non-vanishing neutrino mass which is independent of the CP-violating phase from Eq. (2.8). Tritium has some properties that are beneficial for the kinematic neutrino mass search, as described in more detail in the next paragraph.

[12] The **W**ilkinson **M**icrowave **A**nisotropy **P**robe and its successor, the Planck space telescope, are satellites measuring the temperature anisotropies of the CMB.

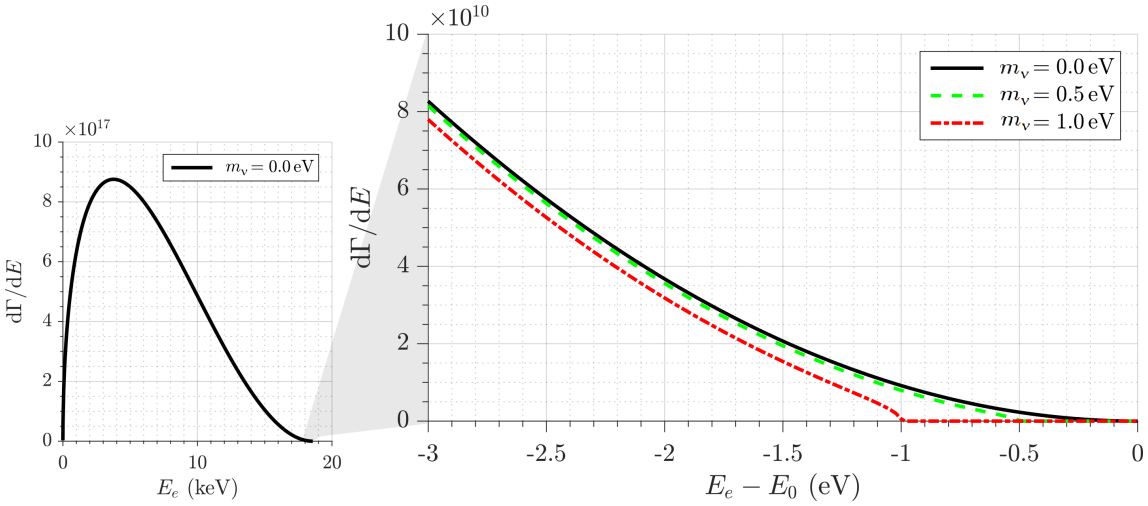

Figure 2.4.: Beta Spectrum of Tritium: Impact of non-vanishing neutrino mass on the differential β-decay spectrum of T_2. **Left:** The total energy spectrum of electrons emitted in tritium decays. **Right:** The spectrum close to the endpoint energy of 18.6 keV, assuming three different neutrino masses yielding endpoint shifts. The x-axis shows the energy of the electrons, shifted towards the tritium endpoint, where E_e denotes the electron energy and E_0 the tritium endpoint. Graphic taken from [Wik].

Tritium as Radiative Source

The decay properties of tritium make this particular nuclide suitable for precise kinematic studies of β-decay. It decays via

$$^3\mathrm{H} \rightarrow {}^3\mathrm{He}^+ + e^- + \bar{\nu}_e \tag{2.31}$$

into the lighter $^3He^+$ isotope. This decay has the following advantages compared to most other β-emitters [KAT05]:

- **Simple Structure:** The structure of only one proton and two neutrons in the nucleus simplifies the calculations and predictions of the decay, as the matrix element in Fermi's golden rule is energy independent.
- **Low Endpoint:** The low endpoint of the electron spectrum of $E_0 = (18.577 \pm 0.007)$ keV of tritium [SDS85] yields a stronger relative influence of the neutrino mass on the spectrum.
- **Short Half-Life:** The short half-life of tritium of 12.3 years allows a reasonably high rate of events even with a small amount of source material.
- **Gaseous State:** Gaseous sources have the advantage, that there are no solid-state effects which can lead to a significant smearing in the spectrum, such as work-functions of electrons in solid materials, as well as scattering effects in solid bodies.

Despite these positive aspects about tritium as source material, it also has some disadvantages.
Tritium, as usual hydrogen also, does not occur in an atomic form but in different isotopologues[13]. The T_2 molecules decay into molecular ions consisting of tritium and helium:

$$\mathrm{T_2} \rightarrow {}^3\mathrm{HeT}^+ + \mathrm{e}^- + \bar{\nu}_\mathrm{e}. \tag{2.32}$$

If the molecule consists of a different composition of tritium, deuterium and hydrogen, the daughter molecule after the decay of the molecules consisting of tritium also can vary.

[13]The gas used in the KATRIN experiment consists of >95 % of T_2, <5 % DT and <1 % HT [KAT05].

Thus, the exact distribution of the final states is not known. Further, also for a known final state distribution, the energetic distribution of mother and daughter molecules introduces additional uncertainties on the measurement. These uncertainties of the distribution of the final states have a significant contribution to the total experimental uncertainty of the measurement.
The tritium spectrum can be calculated to

$$\frac{dN}{dE} = R \cdot (E_0 - E_e)\sqrt{(E_0 - E_e)^2 - m_\nu^2}, \tag{2.33}$$

with the endpoint energy E_0, the electron energy E_e and a normalization factor R, depending on the Fermi constant and the nuclear matrix element for this process [SZ01].

Chapter 3

INTRODUCTION INTO THE KATRIN EXPERIMENT

The **KA**rlsruhe **TRI**tium **N**eutrino Experiment (KATRIN) is operated by an international collaboration of scientists at 20 institutes from Europe and the USA with the main goal to measure the electron antineutrino mass with a precision of 200 meV at 90 % CL [KAT05]. The determination of the very small mass is a huge challenge to the whole collaboration, starting with the handling a daily throughput of up to 40 g of tritium, over to controlling the systematic effects occurring in the 70 m long beam line and finally analyzing the measured electron flux from the tritium β decays. The electrons are emitted inside the Windowless Gaseous Tritium Source (WGTS), travel through the transport sections where the amount of tritium molecules and ions inside the beam tube is reduced by fourteen orders of magnitude to reduce background effects. Finally these electrons are accepted or rejected by the electrostatic spectrometer and counted in the detector according to their kinetic energy, ending up in the complex analysis of the data measured in three net years of data taking.
This chapter deals with the complex experimental setup, located at Tritium Laboratory Karlsruhe (TLK)[1], as well as the main challenges of the experiment and the systematic effects occurring in the measurement. Further, some basic requirements for a successful measurement of the neutrino mass are introduced. First, the motivation and target of the KATRIN experiment is described in Sec. 3.1. Section 3.2 explains the basic principle of the MAC-E filter, which is used as spectrometer for analyzing the electron energy. The Sections 3.3 and 3.4 show the experimental setup of KATRIN. The former gives a brief overview of the individual parts of the tritium-related source and transport section STS and the tritium free spectrometer and detector section SDS, the latter gives a more detailed description of the rear section and the e-gun used as electron source for commissioning measurements, such as the energy loss measurement which is the main topic of this thesis.

3.1. Motivation for the KATRIN Experiment

As discussed in Ch. 2, a non-vanishing neutrino mass has noticeable implications on cosmology and particle physics, as it is an important parameter in cosmological models.
Due to the strong dependence on the input model and used data in indirect neutrino mass measurements, a direct method for a precise determination of m_ν is needed. This was done by experiments such as the ones in Mainz and Troitsk, yielding an upper limit for

[1] Tritium Laboratory Karlsruhe at the Karlsruhe Institute of Technology

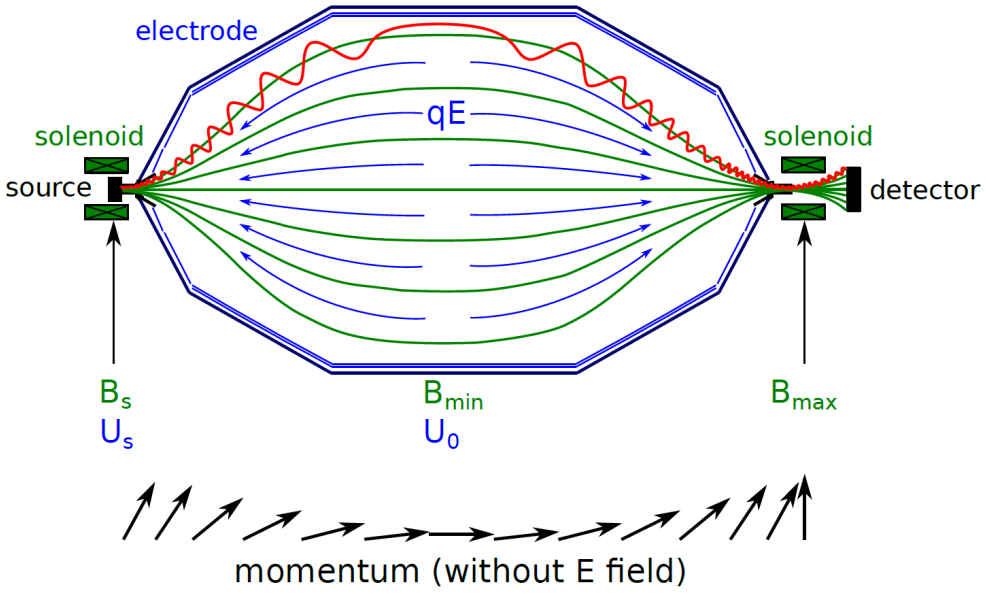

Figure 3.1.: Schematic drawing of a MAC-E filter: The solenoids at the entrance and exit of the vessel provide a magnetic field $B_{\max}$ (green lines), the strength of which decreases towards the center of the vessel ($B_{\min}$). The electrostatic retardation field (blue lines) is created and controlled by the electrodes and the vessel itself. The red spiral line shows a schematic view of the electron tracks through the spectrometer vessel. In the lower part of the graphic, the transformation of transversal into longitudinal momentum is sketched. Graphic from [Wan13].

the electron antineutrino mass of $m_{\nu_e}^{\text{Mainz}} \leq 2.3\,\text{eV}$ and $m_{\nu_e}^{\text{Troitsk}} \leq 2.05\,\text{eV}$ both at 95 % CL [KBB+05, ABB+11].
Using the same measurement principle as the Mainz and Troitsk experiments, the MAC-E filter (see Sec. 3.2), for the spectroscopy of the tritium decay electrons, a precise neutrino mass measurement can be performed, at the target of

$$m_{\nu_e} = 200\,\text{meV}\ 90\,\%\ \text{CL},$$

after three net years worth of data taking. This sensitivity goal means an improvement by a factor of 100 on the measured observable m_ν^2, see Eq. (2.33), compared to the results of Mainz and Troitsk and thus yields strict requirements to the experiment's systematic effects, as described in Sec. 3.3.

3.2. The Spectrometer Principle of the KATRIN Experiment: The MAC-E Filter

To measure the mass of the electron antineutrino from β-decay, the precise investigation of the endpoint of the spectrum is necessary. In the KATRIN experiment, an energy resolution of 0.93 eV [KAT05] is achieved by a MAC-E Filter (**M**agnetic **A**diabatic **C**ollimation combined with an **E**lectrostatic filter) [BPT80]. A MAC-E filter consists of two elementary features. The first is the electrostatic retardation potential, to filter the incoming electrons in the manner of a high pass filter leading to an integral spectrum by successively scanning through many voltage steps. The second one is the magnetic field to guide the electrons and to define the resolution. These two components are described in the following and shown in Fig. 3.1.

Since electrons are charged particles, they can gain or lose kinetic energy while traveling through an electric field, and thus get accelerated or retarded according to

$$\Delta E = e \cdot \Delta\Phi, \tag{3.1}$$

where E denotes the particle energy, e is the electron charge and Φ is the electric potential. This retardation is used to block electrons with low kinetic energy than the retardation potential.
As the electrons are emitted isotropic in the WGTS, the direction of the electrons do not form a linear beam from the source to the detector. To guide the electrons emitted not directly pointing towards the detector, a strong magnetic field is used. Due to the Lorentz force

$$\vec{F_L} = q\left(\vec{v} \times \vec{B}\right) \tag{3.2}$$

electrons follow circular orbits around the magnetic field lines, yielding a spiral motion towards the detector, along the magnetic field. The isotropic emission has influence on the transmission of the electrons. Only the component parallel to the magnetic field is considered for the transmission, as the electric field is parallel to the magnetic field in the analyzing plane.
With the concept of magnetic adiabatic collimation the resolution of the spectrometer is defined. With the magnetic moment being conserved

$$\mu = \frac{E_\perp}{B} = \text{const.} \tag{3.3}$$

with $E_\perp$ being the kinetic energy of the electron from the motion perpendicular to the magnetic field $E_\perp = E \cdot \cos^2(\theta)$, a weaker magnetic field in the analyzing plane lowers the perpendicular component of the kinetic energy. With energy conservation the total kinetic energy of the electrons must remain constant yielding a boost of the electrons in the direction parallel to the magnetic field. All electrons (independent of their initial direction) will carry most of their kinetic energy in the direction parallel to the magnetic field, this alignment process is indicated by the arrows in the lower line in Fig. 3.1. This alignment depends on the ratio between the maximal magnetic field (where the electrons can be perpendicular to the magnetic field) and the minimal magnetic field (where the electrons are maximally aligned), defining the energy resolution

$$\frac{\Delta E}{E} = \frac{B_{\min}}{B_{\max}}. \tag{3.4}$$

In the case of the KATRIN experiment, an energy resolution of $\Delta E = 0.93\,\text{eV}$ at the end of the tritium spectrum at $E = 18.6\,\text{keV}$ is required [KAT05]. This yields the requirement of the ratio between the maximal and minimal magnetic field of

$$\frac{B_{\min}}{B_{\max}} = \frac{\Delta E}{E} = \frac{0.93\,\text{eV}}{18.6\,\text{keV}} = 5 \times 10^{-5}. \tag{3.5}$$

Not only the magnetic moment, but also the magnetic flux is conserved

$$\Phi = \int \left|\vec{B}\right| \, dA = \text{const.} \tag{3.6}$$

Thus, for a decrease of the magnetic field, the area of the flux tube grows. In order to avoid the electrons hitting the spectrometer walls, the vessel needs to have an inner diameter of 9.8 m and a length of 23.3 m, in order to be able to guide the electrons adiabatically to the detector.
With this understanding, a transmission function of the spectrometer as shown in Fig. 3.2 can be derived to

$$T(E) = \begin{cases} 0 & \text{for } E_\parallel - qU < 0 \\ \dfrac{1-\sqrt{1-\frac{E_\parallel - qU}{E_\parallel}\cdot\frac{B_{\max}}{B_{\min}}}}{1-\sqrt{1-\frac{\Delta E}{E_\parallel}\cdot\frac{B_{\max}}{B_{\min}}}} & \text{for } 0 < E_\parallel - qU < \Delta E \\ 1 & \text{for } E_\parallel - qU > \Delta E \end{cases} \tag{3.7}$$

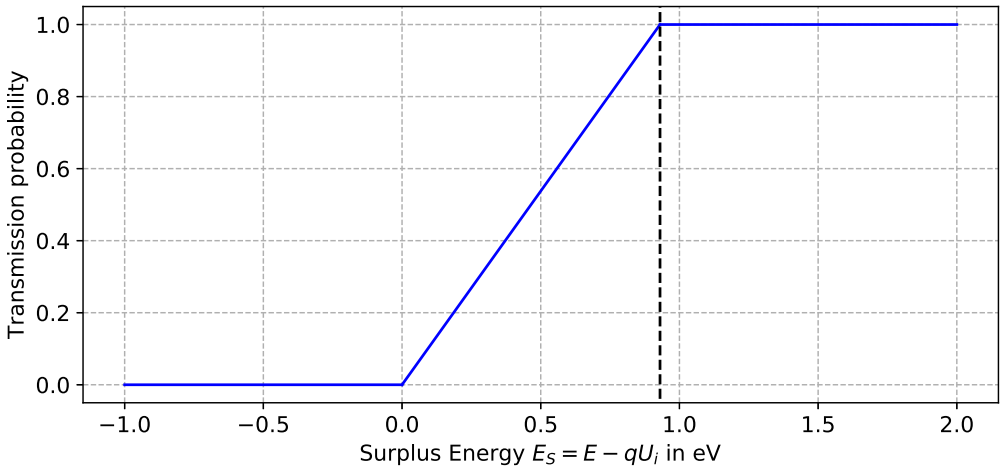

Figure 3.2.: The Spectrometer Transmission Function: As shown in this graphic, the transmission edge of the spectrometer is not perfectly sharp. The slope of the edge is defined by the magnetic field , as denoted in Eq. (3.4) and (3.7). The black dashed line denotes the KATRIN spectrometer resolution of 0.93 eV.

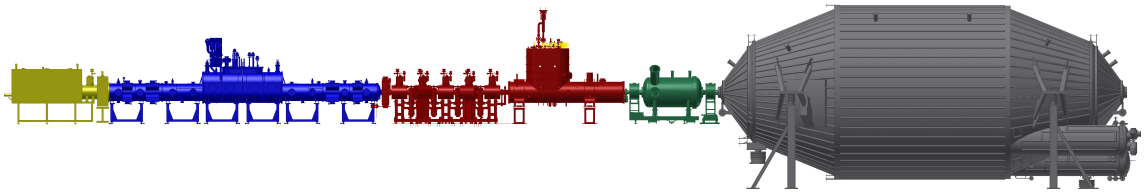

Figure 3.3.: Overview of the Full KATRIN Beamline: This figure shows a schematic drawing of the 70 m long KATRIN beam line. Elements from left to right are the rear section (RS, yellow) for monitoring and calibration of source parameters and the total beam line, the windowless gaseous tritium source (WGTS, blue) followed by the differential and cryogenic pumping sections (DPS and CPS, red) to reduce the tritium flow into the spectrometer section, and finally the pre and main spectrometer (PS, green and MS, grey) with the focal plane detector, FPD at the end of the beam line (not shown in the graphic). Graphic adapted from [Wik].

with the width ΔE of the transmission edge defining the spectrometer resolution. $E_{\parallel} = E \cdot \sin^2(\theta)$ denotes the parallel component of the kinetic energy.

3.3. The Hardware Setup of the KATRIN Experiment

According to its purpose, the 70 m long KATRIN setup can be divided in two main parts, namely the source and transport section (STS) and the spectrometer and detector detection (SDS). The beam line is made up of the different components shown in Fig. 3.3. The setup consists of (from left to right in Fig. 3.3) the rear section (RS) for commissioning of the system, the windowless gaseous tritium source (WGTS) providing β-electrons, the differential and cryogenic pumping sections (DPS & CPS) for tritium reduction outside the WGTS. Further downstream, the pre and main spectrometer (PS & MS) are installed with the focal plane detector (FPD) system containing the silicon detector for counting the transmitted electrons. In this section, the components of the KATRIN setup and their functions are described. This section also takes a brief look at the systematics and requirements for the individual parts of the setup. All information and values from this section are taken from the KATRIN Design Report [KAT05], if not specified differently. Following the beam line, Sec. 3.3.1 describes the tritium related parts of the setup including the second containment and vacuum system, as well as the WGTS and the transport section, followed by the description of the spectrometers and the detector system in Sec. 3.3.2.

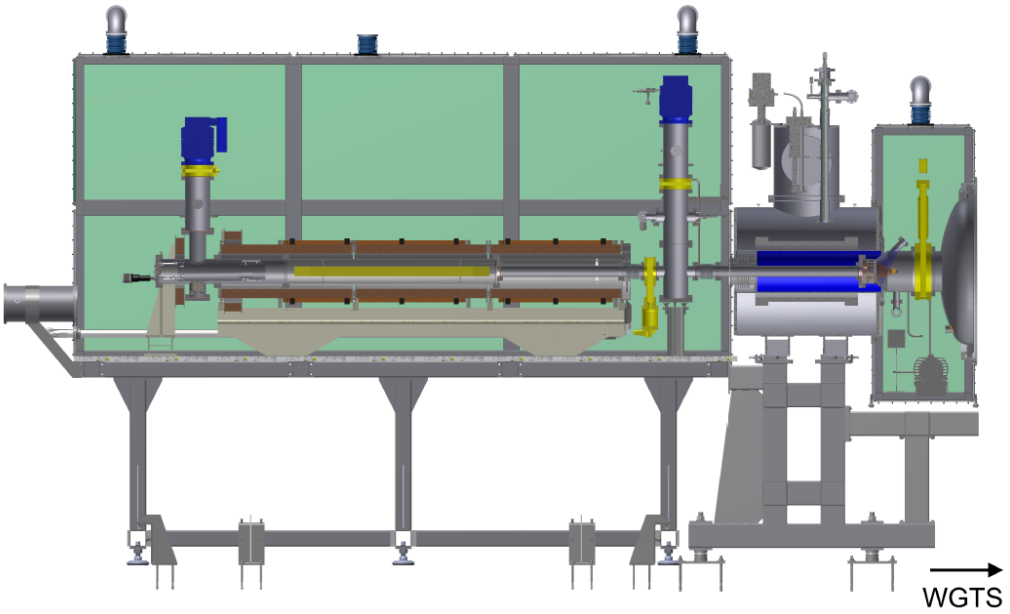

Figure 3.4.: Schematic view of the rear section: The e-gun is located in the large second containment box on the left with its acceleration electrodes. On the right side, the WGTS is connected, separated by the rear wall. Graphic adapted from [Bab14].

3.3.1. Source and Transport Section - STS

The STS is located inside TLK, and contains the tritium related parts of KATRIN. Namely the tritium source (WGTS) as well as the transport and pumping sections (DPS and CPS) between the source and the spectrometer, which reduce the amount of tritium molecules by 14 orders of magnitude in order to minimize the background of decaying particles in the spectrometer. In addition, the KATRIN setup comprises the rear section (RS) for monitoring and calibration measurements. In this section, these elements are described and their main tasks explained.

Second Containment

Due to the high tritium safety requirements all tritium related parts of KATRIN have to be housed in the so-called Second Containment. Having a maximum leakage of 0.1 % of the second containment volume per hour makes sure that no tritium gas is inside the TLK building and the laboratory atmosphere [Bab14]. Additional tritium safety is achieved by setting the second containment under a lower pressure than the laboratory atmosphere. The second containment is indicated in Fig. 3.4 in green.

Rear Section

The KATRIN rear section is built to perform system characterization measurements and to monitor the source activity. One of the major parts included in the RS is the electron gun (or 'e-gun', for short), a monoenergetic electron source. To generate the electrons in photoelectric effect, a gold-plated photocathode is illuminated by UV-light, which leads to electrons being released from the surface. In the next step, these electrons are accelerated by an electrostatic field to a certain kinetic energy. This allows to shoot electrons through the whole KATRIN setup in calibration measurements. The energy of the electrons can be set by adjusting the accelerating voltage, whereas the width of the energy-distribution depends on the energy of the illuminating photons, i.e. the exact wavelengh of the UV-light [Beh16]. This way, many parameters can be verified and monitored, e.g. the column density

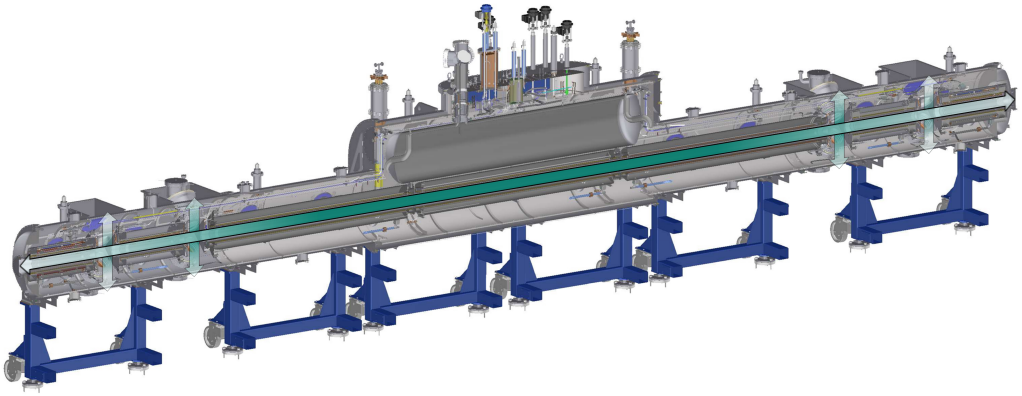

Figure 3.5.: Schematic cross section of the windowless gaseous tritium source of the KATRIN experiment: The tritium gas is injected in the middle of the WGTS, where the density is the highest. The pumping ports are located at both ends of the WGTS. The rear section is connected to the WGTS on the left of this graphic and the downstream beam tube on the right. The tritium density and flow is indicated by the green band. Graphic adapted from [HSM17].

inside the WGTS and the transmission function of the main spectrometer.
Using electrons from the e-gun, the response functions (see Sec. 4.3 and Fig. 4.2) used in this thesis can be determined experimentally by varying the potential difference between the starting potential of the electrons and the retardation potential in the main spectrometer at various column densities.
More details about the rear section and the e-gun are discussed in Sec. 3.4.

Windowless Gaseous Tritium Source

The windowless gaseous tritium Source (WGTS, see Fig. 3.5) is one of the key parts of KATRIN. This is where the tritium is circulated through the beam line, and where the β-electrons are emitted and guided from towards the detector.
The 16 m long and 5 m high WGTS cryostat hosts a central beam tube of 90 mm in diameter and 10 m in length. On the open front-end it is connected to the transport section (i.e. directly to the DPS) and on the rear side it is separated from the RS with a gold-plated Rear Wall. During the neutrino mass measurements, the gas is injected right in the middle of the WGTS with a pressure of $p = 3.4 \times 10^{-6}$ bar, and diffuses towards the ends, where it is pumped out by six turbo molecular pumps (TMPs) on each side [KAT05]. This results in a column density of $\rho d = 5 \times 10^{17} \frac{1}{\mathrm{cm}^2}$ at a temperature of $T = 27\,\mathrm{K}$ [KAT05].
Tritium can decay into helium-3 via ${}^3\mathrm{T}_2 \rightarrow {}^3\mathrm{HeT} + e^- + \bar{\nu}_e$. The occurring β-decay in the WGTS with the nominal column density and tritium purity provides a total source activity of $A = 9.5 \times 10^{10}$ Bq [KAT05].
To guide the electrons adiabatically to the spectrometer and detector, a magnetic field is required. The 3.6 T strong field is produced by seven superconducting solenoid magnets surrounding the central beam tube and the pumping ports [A$^+$18e].
The tritium source is chosen to be windowless, as even a thin closed window would completely absorb the emitted 18 keV electrons. To be able to calculate the energy loss of electrons, traveling through the WGTS and scattering off tritium molecules (see Chap. 4), it is important to have the best possible knowledge about the column density in the source. The experiment requires ρd to be stable in the 0.1 % range [PSB15]. This results in a temperature variation of $\Delta T = 30$ mK or less. This high stability can be achieved by a two-staged cooling, based on liquid neon and helium. To make sure the tritium purity is at the required high level ($> 95\,\%$), the WGTS is supplied with the gas by a closed circulation, the inner loop system. In the inner and outer loop system, the tritium is purified before

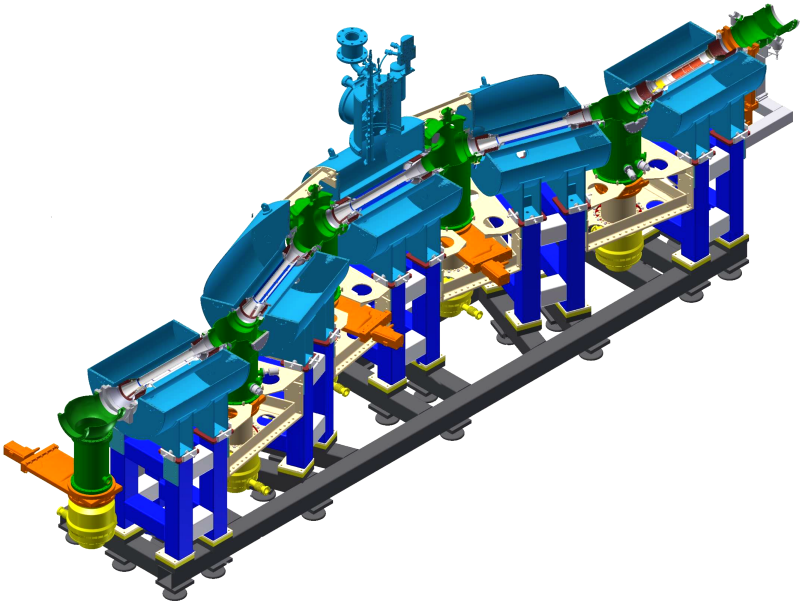

Figure 3.6.: Schematic drawing of the differential pumping section (DPS) for reducing tritium flux in the beam line of the KATRIN Experiment. It is made of five beam tube segments of 1 m length each, tilted against each other by 20°, and turbo molecular pumps between them to pump out tritium gas resulting in a total length of 7.3 m. Five superconducting magnets are installed surrounding the beam line producing a guiding magnetic field of 5.6 T strength. Graphic adapted from [FRS+19].

being injected again. The total throughput of tritium is 40 g/day [PSB15].

Differential Pumping Section

The WGTS is directly connected to the differential pumping section (DPS). The two main tasks of the transport section containing the DPS and the later described cryogenic pumping section (CPS) are to reduce the remaining tritium flow in the beam tube and to guide the electrons towards the spectrometer along magnetic field lines.
The reduction of tritium flux along the transport section is important, as tritium atoms decaying inside the spectrometer would lead to an additional background rate in the measurement, which worsens the neutrino mass sensitivity.
The DPS uses a cascade of four TMPs to reduce the tritium-molecule flux by 5 orders of magnitude in comparison to the amount of tritium in the WGTS. This means an outgoing flux (DPS → CPS) of less than 10^{-7} mbar l/s [LBB+12].
As Fig. 3.6 indicates, the DPS is build of five segments of 1 m length each, tilted against each other by 20°, with a diameter of 75 mm. Between the five segments, four TMP pumping ports are installed, with a pumping speed of >2000 l/s for tritium each.
Each of these segments is surrounded by an individual solenoid magnet, providing a magnetic field of 5.6 T [A+18e]. Again, the magnetic field is needed to adiabatically guide the electrons from the WGTS through the pumping section and into the spectrometer.
In addition to the reduction of neutral tritium flow by the TMPs, the DPS has a ring electrode installed at the last section, in order to reduce positively charged tritium ions. Blocking charged ions leads to a collection of ions between the WGTS and the electrode at the end of the DPS [KG17]. In order to eliminate them, there are four dipole electrodes installed in the DPS to drift out the ions to the DPS walls, where they get neutralized. Then they can be pumped out.

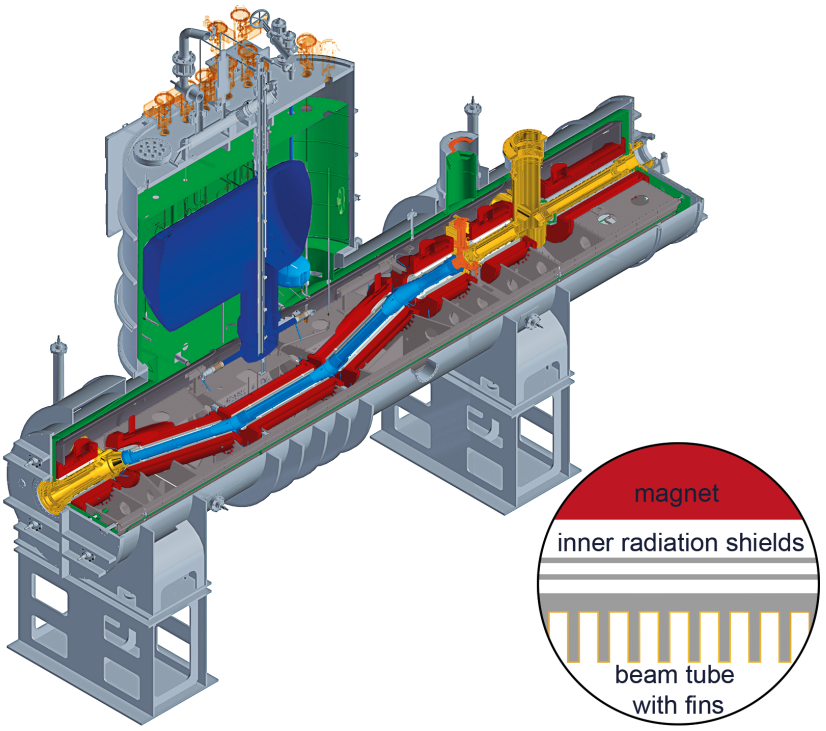

Figure 3.7.: Schematic drawing of the cryogenic pumping section (CPS): It is built from seven beam tube segments: the segments two to five are the cold trap, cooled down to 3 K. Graphic adapted from [FRS+19].

Cryogenic Pumping Section

After being reduced by a factor of 10^7 after the DPS, the tritium flux needs to be further reduced by another seven orders of magnitude in the cryogenic pumping section (CPS). Because of the low pressure at the end of the DPS the TMPs lose their efficiency. To achieve further tritium-flow suppression in a reasonably short distance, cryogenic pumping on precondensed noble gases is used. The CPS uses a 2 µm thin layer of argon, which has two major advantages. On the one hand it increases the surface capacity, and on the other hand it allows for easy regeneration of the cold trap [Jan15].
As shown in Fig. 3.7, the CPS is made of seven beam tube segments, where the first five segments are tilted against each other with an angle of 15°, to avoid direct view from the DPS to the spectrometer and to prevent tritium atoms crossing the CPS without contact with the argon frost covered walls. The cryogenic trap is formed in the beam tube segments 2-5, which are cooled down to 3 K. To achieve the reduction of tritium flow of 10^7, the area of the beam tube's inner surface in the CPS is additionally increased by a fin structure to about 2.7 m^2. To keep the radiative activity of the tritium absorbed in the argon layer below 1 Ci, the frost layer is renewed after 60 days of measurement time by warming up the beam tube to about 100 K and vaporizing the argon. Flushing the tube with helium allows to pump out the remaining trapped tritium at the pumping port inside the CPS and to renew the argon layer.
After passing the DPS and CPS, the tritium flux is reduced by a total factor of 10^{14} in comparison to the starting value in the central WGTS. For the guidance of electrons through the CPS into the spectrometer section, the CPS beam tube is surrounded by superconducting magnets producing a strong longitudinal magnetic field of 5.6 T [A+18e].

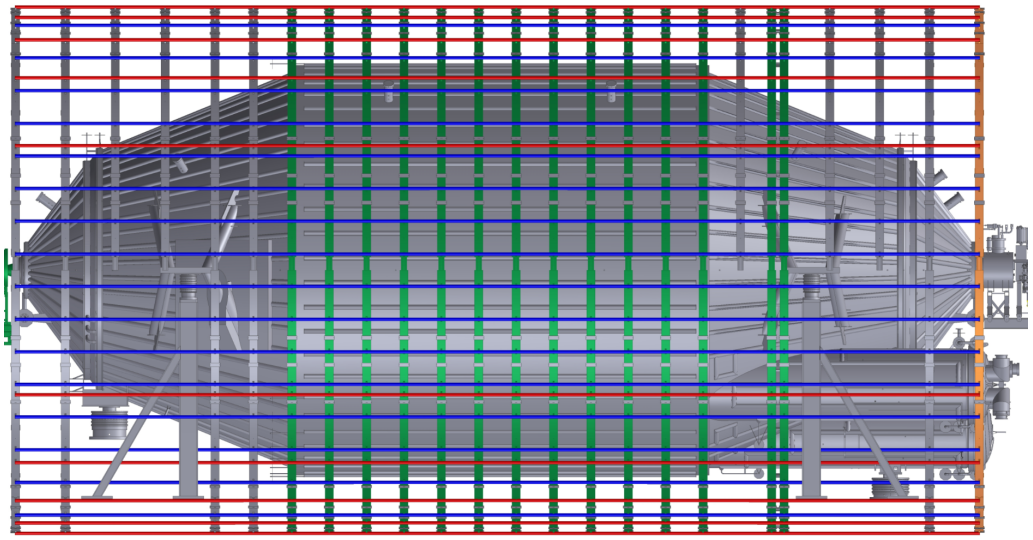

Figure 3.8.: CAD drawing of the Main Spectrometer: Vessel with 23.3 m of length and 9.8 m in diameter. Electrons from the beam line are coming in from the left side, the detector is located at the right. On the right end of the spectrometer, the three pumping ports are located. The horizontal air coils are used for the compensation of the Earth magnetic field. Graphic taken from collaboration database [BSC19].

3.3.2. Spectrometer and Detector Section - SDS

The spectrometer and detector section (SDS) is the part of KATRIN, where the electron energy is determined. The spectrometer filters the incoming electrons according to their energy (see Sec. 3.2), and the detector counts the electrons, which have enough energy to pass the filter potential. This way, it is possible to measure the integrated rate of electrons above a certain filter threshold. The individual parts and their detailed tasks of the SDS are listed and described in the following:

Pre Spectrometer

After passing the transport section (DPS and CPS), the electrons enter the first spectrometer of MAC-E filter type. This pre spectrometer (PS) is used to reduce the incoming flux of electrons into the main spectrometer by a factor of 10^9 by blocking incoming electrons, to minimize the background from secondary electrons in the main spectrometer. To achieve this reduction of electron flux, a retardation energy of 300 eV below the tritium endpoint is typically applied in the pre spectrometer. As the requirements for the pre spectrometer's resolution are not as high as for the main spectrometer, the PS does not require the same size as the main spectrometer. Also, to further reduce the gas flow into the main spectrometer and lower the pressure inside the vessels, there are already two TMPs included into the pre spectrometer, as well as a getter pump system with a pumping speed of roughly 1000 $\frac{\mathrm{m}^3}{\mathrm{s}}$ for hydrogen [Are16].

Main Spectrometer

As described in Sec. 3.2, KATRIN uses the MAC-E filter principle to measure the integral spectrum of tritium β-electrons for the precise investigation of the endpoint of the spectrum and the mass of the electron antineutrino.
The main spectrometer (MS) is a large vacuum vessel with a total length of 23.3 m and a diameter of 9.8 m. Since the magnetically guided flux tube expands to a diameter of about 9 m in the analyzing plane and a total length of 23 m [KAT05], this size is needed in order to ensure the required energy resolution of 0.93 eV, as described in Sec. 3.2. The

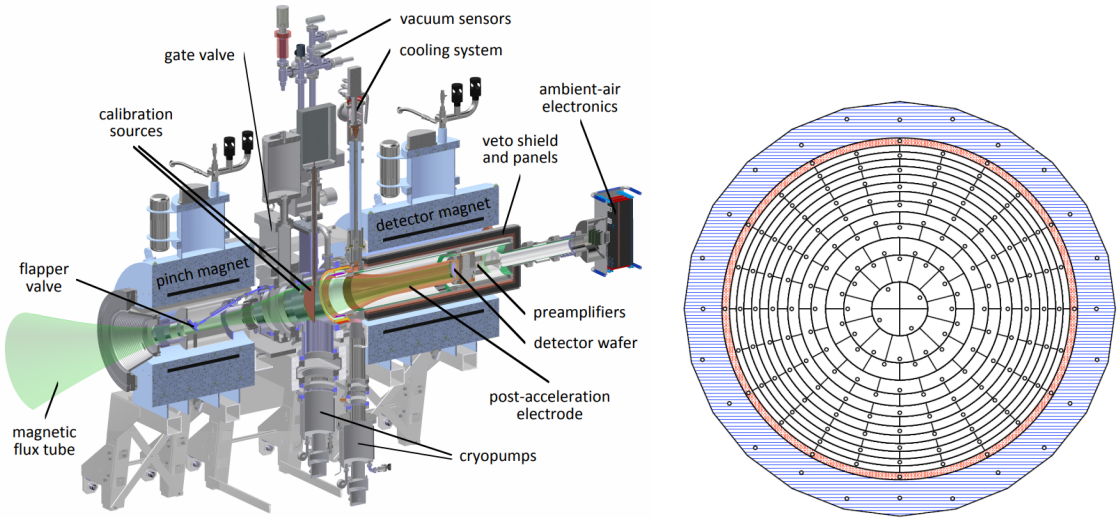

Figure 3.9.: Schematic View of the Focal Plane Detector System: This figure shows the basic components of the focal plane detector system. **Left:** The total FPD system, including post acceleration electrodes and magnets [ABB+15]. **Right:** The layout of the silicon detector wafer, divided into 148 pixels which are arranged in 13 rings [Har12].

large inner surface area of 650 m^2 of the MS is the major challenge for the extreme high vacuum (XHV) of 10^{-11} mbar needed inside the vessel. To ensure the vacuum conditions, three large pumping ports are located at the downstream end of the vessel. With 1.7 m in diameter each, they hold a total of 3000 m of NEG getter pumps with a pumping speed of about 1000 $\frac{m^3}{s}$ for hydrogen. In addition there are TMPs installed in two of the three pumping ports to pump out non-getterable gases from the vessel [A+16b].
For the high precision of the energy of the MAC-E filter well-known and very stable electric and magnetic fields are necessary. To achieve a symmetric magnetic field, in the analyzing plane area of the spectrometer, with still two different fields at the ends of the vessel, a system of 14 air coils with a diameter of 12.6 m is installed around the vessel to compensate this asymmetry and the horizontal component of the Earth's magnetic field. To compensate the Earth's magnetic fields vertical component, additional horizontal coils are installed around the spectrometer, the Earth Magnetic field Compensation System (EMCS). These systems protect the magnetic field inside the spectrometer against the Earth's magnetic field mainly in the analyzing plane, where the B-field is only 3×10^{-4} T and therefore would be significantly deformed by the Earth's magnetic field.
With the given values for the magnetic field at the ends and in the analyzing plane, the resolution of the MS can be calculated to $\Delta E = 0.93$ eV (see section 3.2).

Focal Plane Detector

At the very end of KATRIN, the focal plane detector (FPD) is located. Due to the 6 T strong pinch magnet on the downstream end of the MS, the flux tube is again narrowed down. Behind this 'focal plane' a detector system is installed inside a superconducting magnet generating a magnetic field of 3.6 T to count the electrons which passed the retarding potential of the MAC-E filter. This magnetic field causes the flux tube to be of 90 mm of diameter and ensures a projection of the analyzing plane to the total area of the detector [ABB+15].
A PIN-doped (positive-intrinsic-negative) silicon wafer of 90 mm diameter and 500 µm thickness is used for the detection of the incoming electrons. For an increased spatial resolution, the doping is not constant, but split up into 13 rings. The center ring is separated into four quarters, whereas the other twelve rings are segmented into twelve pixels each,

thus resulting in a total of 148 pixels. With this segmentation it is possible to determine and investigate spatial variations of the electron rate and to take inhomogeneities of the electrostatic and magnetic field in the analyzing plane into account.
Just in front of the detector, there is a post-acceleration system, with the main task of reducing the intrinsic detector background, as it shifts the electrons into an energy region, where the detector background is smaller. The electron energy is typically shifted towards higher energies by 30 keV [Har12].

3.4. The KATRIN Rear Section E-Gun for Commissioning Measurements

As already briefly mentioned in Sec. 3.3.1, the most upstream part in the KATRIN setup is the rear section. This thesis deals with measurements and simulations describing the energy loss of electrons in deuterium and tritium, thus the rear section and its e-gun is of high importance for measurement and simulation parameters. In the following the design parameters of the rear section and the e-gun are described in more detail. A schematic drawing of the rear section is shown in Fig. 3.4.
First, in Sec. 3.4.1, the working principle of the e-gun and the process of creating electrons is described. Sec. 3.4.2 deals with the experimental implementation of the UV-illumination for the e-gun.

3.4.1. Creation of Monoenergetic Electrons

In order to be used for the measurement of the energy loss function, the e-gun has to fulfill some requirements for the properties of the electrons, such as the energy spread being not wider than 0.2 eV in the region of the tritium endpoint, and the angular spread of the emitted electrons being not larger than $\Theta_{\max} = 0.5^\circ$ for zero angle setting [Beh16]. In the case of the KATRIN RS e-gun, the photocathode is plated with gold, with a work function of about $W = 4.5\,\text{eV}$ [Beh16]. The illumination of the gold-covered cathode results in a maximum electron energy of

$$E_{e^-,\max} = h\frac{c}{\lambda} - W \tag{3.8}$$

where h is Planck's constant, c the speed of light in vacuum and λ the wavelength of the UV-light.
When a photon interacts with an electron in the gold cathode, it is absorbed, and thus the electron gains the photon energy. If the photon energy is higher than the electron's binding energy in the material, the electron can be released from the solid body and propagate as a free particle. After being released from the cathode, the electron carries a kinetic energy with a temperature dependent distribution with $0 < E_{\text{kin}} < E_{e^-,\max}$. This distribution is the Fermi-Dirac-distribution $f(E,T)$, describing the energy distribution of identical particles with semi-integer spin in thermal equilibrium, and the density of states inside the material $D(E)$, describing how many different energetic states occur in a given energy-range. Thus the total energy distribution of electrons in the conduction band can be described as $f(E,T) \cdot D(E)$.
The Fermi-Dirac-distribution for $T = 0$ is described by a step function

$$f(E,0) = \begin{cases} 1 & \text{for } E < E_f \\ 1/2 & \text{for } E = E_f \\ 0 & \text{for } E > E_f \end{cases}, \tag{3.9}$$

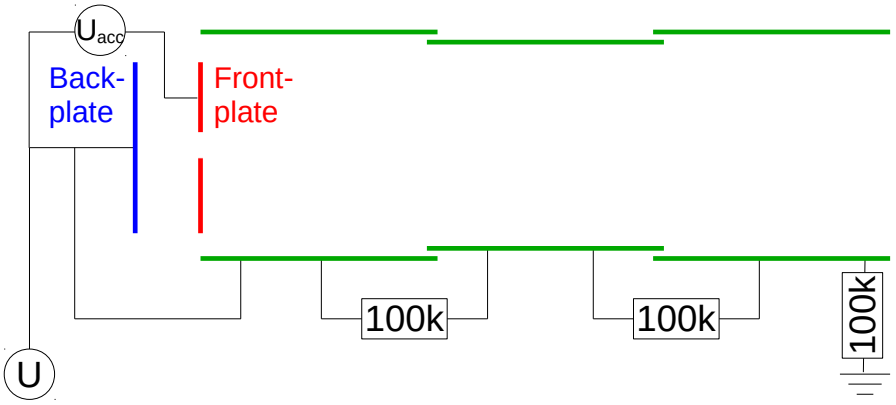

Figure 3.10.: Electron Acceleration in the E-Gun: Schematic drawing of the acceleration cascade in the e-gun. The electrons are emitted at the rear plate (blue) at a potential of U_{start} and accelerated towards the front plate (red). After leaving the e-gun through the hole in the front plate, the electrons are further accelerated by electrodes (green) which are connected to each other via 100 kΩ resistors in order to achieve a linear acceleration.

where E_f denotes the Fermi-Energy. With rising temperature the sharp step is smeared out, following[2]

$$f(E,T) = \frac{1}{\exp\left(\frac{E-E_F}{k_B T}\right)+1}. \tag{3.10}$$

The density of states follows a square-root function $D(E) \propto \sqrt{E}$. This is important, as it describes the distribution of electron energies in the solid body, from which they get separated by getting energy transferred from the photon to the electron during illumination. Therefore, this density of states is important to describe the energy distribution of the outgoing electrons.
To make sure that the electrons do not move back to the cathode, a first electromagnetic field has to be applied close to the surface. This is achieved by an e-gun design with two photocathode-plates. In the first one, the back plate, the photo emission process occurs. This cathode is set on a negative potential U_{start}. The front plate is set to a higher potential $U_{\text{start}} + U_{\text{acc}}$, with $U_{\text{acc}} \approx 6\,\text{keV}$, in order to accelerate the electrons away from the cathode surface, see Fig. 3.10. The front plate has a hole in the middle through which the electron beam leaves the e-gun [Zac15].
The two plates can be tilted by an angle Θ with respect to the magnetic field lines, in order to control the electrons' initial pitch angle relative to the magnetic field lines.
Just after the electrons leave the e-gun through the front plate, they get further accelerated by a series of three electrodes. The kinetic energy of the electrons is only dependent on the difference between the potential at the e-gun, and the general KATRIN ground potential, and especially not on the exact electric field properties along the accelerating electrodes [Bab14]. The splitting of the post acceleration into multiple steps yields a more stable angular distribution of the electrons finally entering the WGTS.
With the tiltable back and front plates and the variable first acceleration voltage, it is possible to set all the required values for the electrons' angular and energy distribution, as described at the beginning of Sec. 3.4.1.

[2] For $T \to 0$, Eq. (3.10) is converging towards (3.9).

3.4.2. The Optical System for E-Gun Illumination

In order to provide enough energy to the electrons to leave the binding potential of the photocathode, the photon energy must be higher than the work function. For a gold cathode with a work function of about 4.5 eV, a UV illumination with a wavelength of below 275 nm is required. To be able to control the energy spread of the created electrons, a tunable light source with wavelengths in the region of 200 nm to 300 nm is needed. The laser-driven light source (LDLS) was chosen to be used as e-gun light source due to its high optical power in the demanded wavelength range [Bab14].
The LDLS is capable to deliver a very broad spectrum of electromagnetic radiation from deep UV-region to high IR wavelengths (roughly 170 nm up to over 2000 nm [ET]). This adjustability, especially in the desired UV-range of 170 nm to 300 nm is important in order to be able to adjust the electron rate and the energy distribution of the emitted electrons. A higher light intensity yields a higher photon rate and thus a higher electron rate.
The other important parameter is the width of the electrons' energy distribution. A sharp match between the work function and the spectral range of the photons with a reasonably high electron rate is what is aimed for. Using the LDLS it is possible to generate a sufficiently high intensity at the required wavelength. In order to not smear the electron energy to much due to a very broad spectrum of the incoming light, a spectral filter, a monochromator, is used between the LDLS and the photocathode. Thus, a range of wavelengths can be chosen with variable central value and width.
After passing the monochromator, the UV light is coupled into an optical fiber and transported into the rear section to the e-gun.
To investigate the response functions for energy loss measurements, the e-gun needs to have a very sharp energy distribution ($\Delta E \approx 0.2\,\mathrm{eV}$), and a well known emittance angle close to zero [KAT05]. The aimed for value for the electron intensity is about 10^4 to 10^5 electrons per second, with a stability of 0.5 per mille on the timescale of several days [KAT05].
In addition to the LDLS, a pulsed laser light-source is installed in the rear section. This pulsed laser can be used for the time-of-flight method for energy loss measurements [Wei18]. This pulsed Nd:YVO_4 laser has a wavelength of 266 nm with a power of 100 mW and a pulse width below 40 ns with a pulse frequency of up to 100 kHz[3].

3.5. Current Status and Milestones of the KATRIN Experiment

From the first ideas for a next generation neutrino mass experiment and the Letter of Intent in 2001 [KAT01], until today, many milestones of the KATRIN experiment were achieved. Three years after the first Letter of Intent, in 2004, the first planning and design period of the KATRIN experiment was finished, resulting in the Design Report [KAT05] which states all design values and parameters for every component of the experimental setup, as well as the goal of a neutrino mass sensitivity of

$$m_{\bar{\nu}_e} = 200\,\mathrm{meV}\ (90\,\%\,\mathrm{CL})\,, \tag{3.11}$$

with the according maximum tolerated systematic uncertainties for every individual part of the measurement (Error Budget).
The following years were spent on building and installing the individual parts of the KATRIN setup, which are described in Sec. 3.3 in detail.
After integrating the whole KATRIN beam line from the WGTS to the FPD, the First Light measurement campaign was performed in 2016, where electrons traversed the entire beam line for the first time [A$^+$18d]. During this measurement campaign, electrons were generated at the rear wall, to investigate the alignment of the beam line, as well as ions

[3] The laser is manufactured by InnoLas (`http://innolas-laser.com`). The values are taken from this specific laser's data sheet.

being injected to the beam tube for background investigations.
In the following year measurements with a gaseous krypton source (GKrS) were performed. The goal of this GKrS measurement was to investigate the properties of the spectrometer section. Investigation of the energy response for the well-known K-32 line yielded information about the spectrometer section and systematic effects occurring in the measurements [A$^+$18d, VSD$^+$18, SDL$^+$18].
The next large step towards the neutrino mass determination was performed, namely the First Tritium measurement campaign in June 2018. For the first time since the installation of the individual components at TLK facility, the beam tube was filled with a low amount of tritium, with gas consisting of DT instead of T_2. In this measurement, again the alignment of the system, as well as some background effects occurring in the experiment could be characterized. First Tritium was considered successful as the first KATRIN tritium β-spectrum could be measured [Sch18].
In September and October 2018, the next system characterization and commissioning campaign was started, the STS-IIIa measurement. These measurements were focused on the commissioning of the tritium related parts of the KATRIN setup, without tritium being circulated through the system. One part of STS-IIIa was the characterization of the RS e-gun and the energy loss measurements, as described in Ch. 6.
Finally, 18 years after the first letter of intent, KATRIN is ready for the first neutrino mass measurements, to be started in 2019.

Chapter 4

ENERGY LOSS PROCESSES OF ELECTRONS IN TRITIUM AND MEASUREMENT PROCEDURE

For a precise determination of the neutrino mass by measuring the β-decay electron spectrum of tritium near to its endpoint, it is crucial to know how much energy the electrons lose while traveling through the 70 m long beam line of the KATRIN experiment. As energy loss happens mainly by the inelastic scattering of electrons off tritium molecules, most energy is lost inside the WGTS, where the gas density of tritium is highest, see Sec. 3.3.
This chapter explains the physics principles of inelastic scattering and molecular excitation in tritium (Sec. 4.1) and describes the currently existing and used models for the energy loss of electrons in tritium (Sec. 4.2). Furthermore, the mathematical principle behind the deconvolution process and the analysis method used in this thesis is described in Sec. 4.3 and 4.4, respectively. Finally, in Sec. 4.5, the latest KATRIN simulation and deconvolution results for the energy loss function are presented, which are the starting point of the work in this thesis.

4.1. The Energy Loss Processes in Gaseous Tritium

In order to describe the energy loss processes occurring in the WGTS, a model is needed. The energy loss function denotes the cross section of electrons for the energy dependent interaction during a single scattering event off a tritium molecule. This energy is lost by the electron and therefore needs to be transferred to the scattering target. To get an energy loss model that describes the scattering processes well enough for reaching the desired neutrino mass sensitivity of 200 meV, it is important to know the energetic structure of the scattering target. In the case of the KATRIN experiment, the targets are free gas molecules. Electrons in these molecules can be excited into higher electronic states, or get completely separated from the molecule which thus gets ionized, also the molecules can get dissociated. These processes happen at a given probability which depends on the amount of energy that is transferred during the scattering process.
The two models used in the preparations for the KATRIN experiment are shown in Fig. 4.1.

Electronic Excitations

As known from molecular physics, electrons in molecules have different discrete energetic states. Absorbing an incoming particles' energy, an electron can be excited to a higher

energetic state through scattering, and the incoming particle loses the amount of energy according to the difference between the two electronic states of the molecule before and after the scattering process.
As the energetic levels of atoms are discrete, the excitation energies also have to be. This results in the line structure in the range of 11 eV to 16 eV of energy loss in the right plot of Fig. 4.1. Each of these lines can be described by one transition between two different energetic electron states in the tritium molecule [ABG80].

Ionization

Every electron in a molecule is bound with a finite energy. When an incoming electron transfers more energy than this binding energy E_B in the scattering process, an electron can be completely separated from the atomic nucleus. This process produces a free electron and a positively charged ion, according to

$$\mathrm{T_2} + \mathrm{e^-} \rightarrow \mathrm{T_2}^+ + 2\mathrm{e^-}. \tag{4.1}$$

In contrast to electronic excitations, the energy of a free electron is not forced to be discrete, which will therefore result in a continuous energy distribution. This ionization tail is shown in Fig. 4.1 in the region of $\Delta E \geq 16\,\mathrm{eV}$. A precise description of this tail will be needed in the analysis for determining the total cross section for inelastic scattering.
As the two outgoing particles are identical, the most energy that can be lost is half of the impact energy, because it is not possible to distinguish the incoming scattered electron and the ionization electron after the scattering process, the higher energetic outgoing electron is always considered to be the incoming particle. This fact yields an endpoint of the energy loss function which can be used for normalization.

Dissociation

In nature, tritium appears in molecular form. This means, it is built up of two atoms in an energetically preferred state. The molecule possesses a binding energy of 4.63 eV [Tan16]. This binding can be broken, and the two tritium atoms can be separated from each other. This process requires energy, that can for instance be transferred into the $\mathrm{T_2}$ system by an impacting electron.

Elastic Scattering

One additional effect in scattering processes is elastic scattering, where a very little amount of energy is transferred from the incoming particle to the target. This effect can be described by a very narrow Gaussian peak in the energy loss function, around zero. With a σ-width of only $\approx 25\,\mathrm{meV}$, elastic scattering can be neglected in the following analyses. Due to the fact that its width is smaller than the binning in the simulations and the spectrometers resolution, taking into account elastic scattering would be strongly overweighted in the analysis. This strong overweighting justifies the neglect of the elastic peak in the energy loss function in the work further described.

4.2. Energy Loss Models and Parameterizations for Electrons in Tritium

Currently, there are three different models used to describe the energy loss of 18 keV electrons in deuterium and tritium: The empirical parametrizations by Aseev [ABB+11] and Abdurashitov [ABC+17] and the model by Glück [HHW+17]. The main difference between these approaches is that the Aseev and Abdurashitov models are parametrized using measurement data, whereas the Glück model is derived from theoretical calculations. These different approaches for the determination of the energy loss function yield models

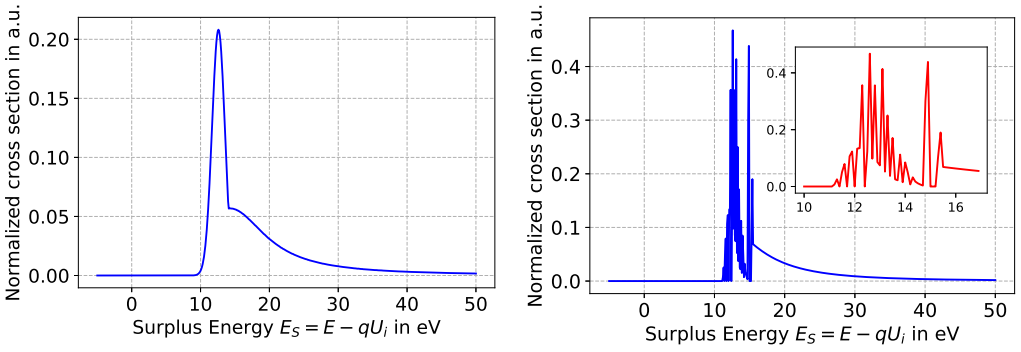

Figure 4.1.: Energy Loss Models for electrons scattering off tritium. **Left:** The Aseev parameterization, measured in the Troitsk neutrino mass experiment and described in [ABB+11]. **Right:** The more detailed Glück model, calculated from molecular models of tritium and its electron shell. The red inset shows the line structure in more detail.

with different features and structures, as can be seen in Fig. 4.1. The Glück model can resolve the individual excitation states of tritium, whereas the models based on measurement data incorporate a smearing of the energy loss function resulting from the experimental setup.
This section gives an overview of the existing models with their advantages and disadvantages.

Glück Model

The energy loss model constructed by F. Glück relies on first-principle calculations. The model is shown in the right plot of Fig. 4.1, with its individual excitation peaks.
In the plot, every individual peak corresponds to one specific electronic or dissociative excitation state of molecular tritium. Here, the first set of lines in the region from 11 eV to 16 eV corresponds to the electronic state excitations of tritium.
This model is the most detailed model that can be used for simulations of the KATRIN experiment.

Aseev and Abdurashitov Parameterizations

One of the predecessor experiments of KATRIN was the Troitsk neutrino mass experiment [BBG+95]. In the course of this experiment, an energy loss function of electrons in tritium was measured and described [ABB+11], and measured again with an increased energy resolution by a factor of 2 in 2017 [ABC+17].
The energy loss spectrum is described by a Gaussian and a Lorentzian distribution, leading a total of six parameters[1]. The Gaussian part of the energy loss spectrum describes the excitation peaks as one single broad distribution with a mean value of 12.6 eV, while the Lorentzian is used to describe the ionization tail of the energy loss distribution.
A new measurement by the Troitsk collaboration in 2017 yielded an updated energy loss parameterization (Abdurashitov et al. 2017).

The fact that both of these approaches have their problems, one not being measured with a high enough energy resolution and the other solely relying on theoretical calculations, requires the KATRIN collaboration to perform its own energy loss measurement and analysis during the operational period for the determination of the energy loss distribution

[1] One of the parameters, the mean value of the Gaussian excitation peak, actually is fixed to its value of 12.6 eV.

$f(\Delta E)$ and the total inelastic cross section σ_{tot}.
For a measurement of the neutrino mass with a sensitivity of 0.2 eV, the requirements for the measurement are very strict. The position of the energy loss peak around 12.6 eV has to be measured with a precision of 5 meV. The KATRIN design report requires a systematic uncertainty for the neutrino mass square due to the energy loss measurement of maximal $7.5 \times 10^{-3}\,\text{eV}^2$ [KAT05, Gro15].
An energy loss function assuming a wrong position of the peak distorts the shape of the measured spectrum, as the reconstruction of the modeled β-spectrum after the convolution with an offset energy loss function will be affected, impacting the reconstructed value of m_ν^2. In the next section, the measurement strategy of this important systematic effect is described in more detail.

4.3. Measurement and Deconvolution of the Energy Loss Function

This thesis describes the investigation and optimization of the deconvolution strategy to derive the energy loss function of electrons scattering off tritium molecules from measurements of the transmission of e-gun electrons through different column densities in the WGTS. This section points out the influence of energy loss on the KATRIN measurement, and describes the measurement procedure and deconvolution process to obtain the energy loss function.
The KATRIN experiment performs an integral measurement of the tritium spectrum. The rate close to the endpoint is very low[2] and thus energy loss has significant influence on the count rate in this region, because only electrons with no inelastic scattering events in the beam tube can be measured in the last 11 eV. With the nominal column density of $5 \times 10^{17}\,\frac{1}{\text{cm}^2}$ the probability for no scattering in the WGTS is 0.18 whereas the probability for one single scattering process is 0.31.
As described in Sec. 3.2, the spectrometer has a certain transmission function, T (see Eq. (3.7) and Fig. 3.2). Any systematic effects occurring between the emission of the electrons in the WGTS and the detection at the FPD have an influence on the measured spectrum of electrons at the detector, and thus will change the transmission function yielding a distortion of the measured spectrum.
Starting with an unperturbed tritium β-spectrum, the response function would be the differential spectrum S_{T_2} convolved with the spectrometer transmission function T multiplied with an additional amplitude factor A:

$$R(E) = A \cdot T(E_S) \otimes S_{T_2}(E), \tag{4.2}$$

where $E_S = E - qU$ is the surplus energy, and E the energy of the electrons. This convolution results in the integral spectrum measured with the MAC-E filter. Introducing further effects, such as energy loss, additional terms must be introduced into the response function $R(E)$ in Eq. (4.2), yielding a different and column scattering dependent response function. In order to take into account energy loss effects, the energy loss function needs to be additionally convolved into Eq. (4.2), changing the spectrometers transmission function into the systems experimental response function.
With an empty source beam tube (i.e. $\rho d = 0\,\frac{1}{\text{cm}^2}$) the experimental response is equal to the spectrometer transmission. Introducing scattering processes due to a non-vanishing WGTS column density, further contributions of single and multiple scattered electrons become important in the response function. When an electron is emitted with a certain kinetic energy E, it is transmitted, if $E_\parallel > qU$ (see Sec. 3.2). When this electron scatters off a tritium molecule and loses energy ΔE before passing the energy filter, the transmission

[2] The count rate in the region of the last eV to the endpoint is about 13 orders of magnitude smaller compared to the total count rate in the entire spectrum.

condition is changed to $E_{\parallel} - \Delta E > qU$.
The contributions of the different multiple scattering processes to the resulting response function can be calculated by a convolution of the spectrometer transmission function with the energy loss function of electrons in tritium, where for each further scattering, the energy loss function needs to be convolved with the previous scattering function once more, i.e. $\epsilon_i = \epsilon_{i-1} \otimes f(\Delta E)$. This recursive approach yields a set of equations for the different scattering functions [HHW+17]:

$$\epsilon_0 = T(E_S) \tag{4.3}$$
$$\epsilon_1 = T(E_S) \otimes f(\Delta E) \tag{4.4}$$
$$\epsilon_2 = T(E_S) \otimes f(\Delta E) \otimes f(\Delta E) \tag{4.5}$$
$$\vdots \tag{4.6}$$

The response function can be derived by adding up the multiple scattering functions ϵ_i with the i-fold scattering probabilities P_i as coefficients, yielding

$$R = \sum_i P_i \cdot \epsilon_i. \tag{4.7}$$

The probability to scatter i times can be calculated with the Poisson distribution in Eq. (4.8), where $\mu(\Theta) = \frac{\rho d \sigma_{\mathrm{tot}}}{\cos(\Theta)}$ is the mean free column density, i.e. the mean column density which an electron can pass without scattering, inside the WGTS:

$$P_i(\mu(\Theta)) = \frac{\mu^i(\Theta)}{i!} \exp(-\mu(\Theta)) \quad \text{with } i = 0, 1, 2, ... \tag{4.8}$$

This gives a total experimental response of

$$T(E_S)_{\mathrm{exp}} = P_0 \cdot T(E_S) + P_1 \cdot T(E_S) \otimes f(\Delta E) + P_2 \cdot T(E_S) \otimes f(\Delta E) \otimes f(\Delta E) + ... \tag{4.9}$$

This way, the influence of the energy loss function on the KATRIN measurement is clearly visible, as the final response function of the experiment is

$$R_{T_2}(E) = A \cdot T(E_S)_{\mathrm{exp}} \otimes S_{T_2}(E). \tag{4.10}$$

From the measured e-gun transmission functions, with the spectrum briefly described in Sec. 3.4.1, scattering functions can be extracted according to the scattering probabilities P_i and the transmission functions using Eq. (4.9). Using the single scattering function

$$\epsilon_1 = T(E_S) \otimes f(\Delta E) \tag{4.11}$$

a single deconvolution is sufficient to determine the energy loss function $f(\Delta E)$.

4.3.1. Integral Measurements to Generate the Energy Loss Function

To experimentally generate the energy loss function $f(\Delta E)$ of electrons in gaseous tritium, the response functions at different column densities (see Fig. 4.2, left) need to be measured. This measurement is performed with the e-gun described in Sec. 3.4.1 due to its adjustable energy and a well-defined energy distribution.
The e-gun is used with an energy of 18.6 keV, according to the tritium endpoint, and a Gaussian profile with σ-width of 200 meV. The spectrometers retardation potential is scanned from 18.605 keV to 18.55 keV resulting in a surplus energy of $E_S = -5$ eV to 50 eV. With discrete voltage set points and step sizes of 100 mV this results in 551 individual data points for every column density setting. This scan is performed with an empty source and with three non-zero column densities. By using a total of 10^7 electrons in every voltage set point, response functions as shown in Fig. 4.2 (left) can be measured. These response functions show the number of electrons transmitted through the spectrometer with a constant number of electrons emitted for every voltage set point.

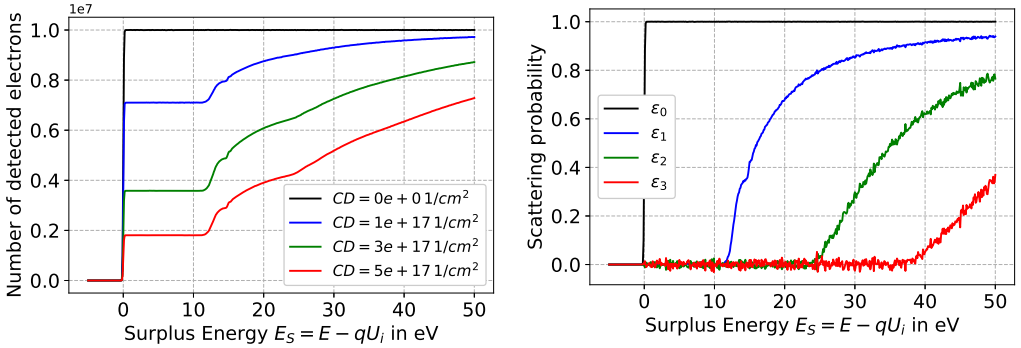

Figure 4.2.: Simulated Response and Scattering Functions for the default column densities ($0\,\frac{1}{\mathrm{cm}^2}$, $1\,\frac{1}{\mathrm{cm}^2}$, $3\,\frac{1}{\mathrm{cm}^2}$ and $5\times10^{17}\,\frac{1}{\mathrm{cm}^2}$), with 10^7 electrons in each surplus energy data point with a scanning voltage step size of 100 mV. **Left:** The response function as it would be directly measured in the experiment. **Right:** The scattering functions ϵ_i that can be added up to the response functions with the scattering probabilities as coefficients.

4.3.2. Deconvolution of the Energy Loss Function

After extracting the single scattering function ϵ_1 from integral measurements performed with the e-gun, the actual deconvolution process has to be performed. As Eq. (4.4) shows, $\epsilon_1 = T(E_S) \otimes f(\Delta E)$, the scattering function is the convolution of the transmission function and the energy loss function

$$\epsilon_1(E_S) = T(E_S) \otimes f(\Delta E) = \int_0^E d(\Delta E)\, T(E_S - \Delta E) \cdot f(\Delta E). \tag{4.12}$$

In the case of discrete data points, as we get them from measurements, the integral in Eq. (4.12) turns into a sum over all N values:

$$\epsilon_1(E - qU_i) = \sum_{j=0}^{N-1} T(E - qU_i - \Delta E_j) \cdot f(\Delta E_j), \tag{4.13}$$

where the index $j = 0, ..., N-1$ counts the data points in the simulated or measured response functions, and i denotes the measured data point. Eq. (4.13) can be expressed in matrix form as

$$\vec{\epsilon_1} = \mathbf{T} \cdot \vec{f}, \tag{4.14}$$

with the vectors $\vec{\epsilon_1}$ and $\vec{f}$ describing the given data points of the scattering and energy loss functions.
The matrix $\mathbf{T}$ will be constructed from the discrete transmission function $T(E_{S,i} = E - qU_i)$, and thus the shape of a quadratic $N \times N$ matrix, where N is the number of data points in our response functions:

$$\mathbf{T} = \begin{pmatrix} T(E_{S,0}) & 0 & & \dots & 0 \\ T(E_{S,1}) & T(E_{S,0}) & 0 & \dots & 0 \\ T(E_{S,2}) & T(E_{S,1}) & T(E_{S,0}) \; 0 \; \dots & & 0 \\ \vdots & \vdots & \vdots \; \vdots \; \vdots & & \vdots \\ T(E_{S,N-1}) & T(E_{S,N-2}) & \dots & & T(E_{S,0}) \end{pmatrix}. \tag{4.15}$$

The zeros in the upper-right part of $\mathbf{T}$ are resulting from the transmission condition $E - qU_i - \Delta E_j \geq 0$. The most intuitive way to obtain a result for the energy loss function is multiplying Eq. (4.14) with the inverse of $\mathbf{T}$ from the left side. However, as many of the values in $\mathbf{T}$ are very close to zero, this matrix is close to be singular, which leads to large numerical noise in the inversion process. Therefore a more suitable method for generating the inverse matrix is needed to solve the problem.

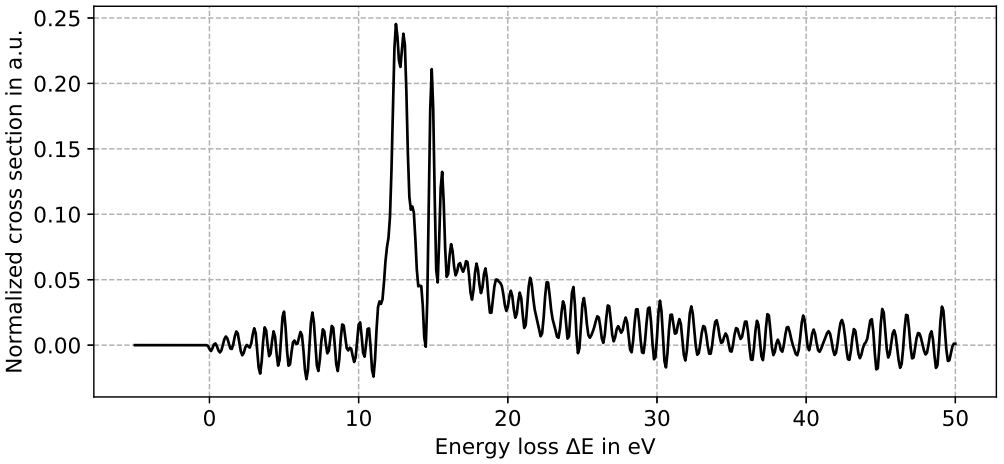

Figure 4.3.: Deconvolution of Energy Loss Function: This figure shows an example of a deconvolution of the energy loss function using KEloss, as described in Sec. 4.3 using a simulation with 10^7 electrons for each voltage set point. This energy loss function is deconvolved from response functions simulated using the Glück energy loss model described in Sec. 4.2. The fine structure of the model cannot be resolved, and additional noise is introduced through the deconvolution process. A comparison between the deconvolved energy loss function and the Glück and Aseev model is shown in the appendix in Fig. A.1.

4.3.3. Singular Value Decomposition

In order to deal with a matrix equation which is numerically close to singular the algebraic method of Singular Value Decomposition (SVD) is applied [Bar04].
This method is based on the theorem that a singular matrix $\mathbf{A}$ can be written as a product of two unitary matrices $\mathbf{U}$ and $\mathbf{V}$ and a diagonal matrix $\mathbf{S}$ as

$$\mathbf{A} = \mathbf{U} \cdot \mathbf{S} \cdot \mathbf{V*}, \tag{4.16}$$

where $\mathbf{V*}$ denotes the adjoint of the unitary matrix $\mathbf{V}$. The diagonal elements of $\mathbf{S}$ are called singular values of $\mathbf{A}$ [Lor03]. The singular values of $\mathbf{A}$, and thus the matrix $\mathbf{S}$, are clearly defined by the matrix $\mathbf{A}$, whereas $\mathbf{U}$ and $\mathbf{V}$ have multiple solutions [Deu08].

$$\mathbf{A}^{-1} = (\mathbf{U} \cdot \mathbf{S} \cdot \mathbf{V*})^{-1} = \mathbf{V} \cdot \mathbf{S}^{-1} \cdot \mathbf{U*}, \tag{4.17}$$

the remaining unknown to be solved for is $\mathbf{S}^{-1}$. As $\mathbf{S}$ is a diagonal matrix, the inverse can be constructed as a diagonal matrix with the inverse elements of $\mathbf{S}$:

$$\mathbf{S} = \begin{pmatrix} \sigma_1 & & \\ & \ddots & \\ & & \sigma_r \end{pmatrix} \Rightarrow \mathbf{S}^{-1} = \begin{pmatrix} \sigma_1^{-1} & & \\ & \ddots & \\ & & \sigma_r^{-1} \end{pmatrix}. \tag{4.18}$$

The advantage of the SVD method is, that it allows to set the elements of $\mathbf{S}^{-1}$ to zero, if the according σ_i is smaller than a chosen threshold value w_{thr}. This way numerical instabilities can be avoided.

4.4. The KEloss Software Package for Energy Loss Simulation and Analysis

To deconvolve the energy loss function from response function measurements with the matrix operations described above, the KEloss software package was developed by Hannen et al. [HHW$^+$17]. In addition to the deconvolution routine, it also provides tools to simulate

response functions and to analyze the quality of the resulting deconvolution of the energy loss function, which are explained in the following.

Response Function Simulation

Using the e-gun as electron source (see Sec. 3.4.1), the energy and angular distribution of the electrons are known. This is not only important for the energy loss measurement but also for the simulations in this thesis, using the design values for the e-gun as input parameters for the simulation. As it was shown in [HHW+17], it is sufficient to consider multiple scattering up to threefold scattering for the deconvolution of the energy loss function in the range of up to $\Delta E = 50\,\mathrm{eV}$. For very large energy windows also higher multiplicities may become relevant. To be able to perform the SVD deconvolution, considering up to threefold scattering, it is required to measure response functions at three different non-zero column densities. The simulation performs the following three steps to generate response functions:

1. **Generation of electrons:** First, electrons are generated, with an initial kinetic energy $E_{\mathrm{kin}}^{\mathrm{init}}$ picked randomly following a Gaussian distribution with a pre-defined width and a pre-defined mean value (see parameters *Electron energy* and *E-gun energy spread* in Tab. 4.1). The electrons have an initial angle against the magnetic field inside the rear section, which again is chosen randomly, according to an isotropic emission with a maximum angle set by *Theta Max* from Tab. 4.1.
2. **Scattering inside the WGTS:** Due to scattering processes, these generated electrons lose energy inside the WGTS. With a scattering probability according to Eq. (4.8) electrons lose energy with a random energy loss ΔE according to the distribution in the selected energy loss model (*UseCSModel* true or false). The electrons now carry a kinetic energy of $E_{\mathrm{kin}} = E_{\mathrm{kin}}^{\mathrm{init}} - \Delta E$.
3. **MAC-E filtering and electron detection:** After the scattering processes in the WGTS the electrons have a kinetic energy E_{kin} and a momentum under a given angle towards the magnetic field lines. This energy and the angle are essential to determine if the electron gets transmitted through the MAC-E filter or not. The angles can be defined by the magnetic fields in the beam tube (B_A, B_{max}, B_S and B_{WGTS}), see Sec. 3.2. If the electron fulfills the transmission condition $E_{\parallel}^{\mathrm{kin}} - qU > 0$, it is registered as transmitted and counted.

This process is repeated for a number of electrons according to a Gaussian distribution of a σ-width of $\sqrt{N}$ and a mean value of N, where N is the *Number of Electrons* simulation parameter, as described in Tab. 4.1. A response spectrum is generated, by repeating this process for many different retardation potentials U_{ret}.

Review of Deconvolution

After performing the SVD deconvolution and gaining an energy loss spectrum from simulated (or measured) response functions, the quality of the deconvolved energy loss function has to be verified, to make sure that the measurement meets the requirements for the KATRIN experiment. A quantitative method to determine the error on the deconvolution is the ensemble test from the KEloss package described in the following:
First, a Monte Carlo simulation of one thousand KATRIN neutrino-mass measurements is performed. It is important to mention that this Monte Carlo simulation assumes massless electron antineutrinos. The resulting spectrum of one of these Monte Carlo simulations is shown in the left plot of Fig. 4.4. For this step, the Glück energy loss model is used, as it

Table 4.1.: Parameters for the Response Function Simulations to generate the data for the deconvolution process. This table shows the parameters as well as their default values and a brief description.

Parameter	Default value	Brief description
Column Density	$[0,\ 1,\ 3,\ 5] \times 10^{17}\ \frac{1}{\mathrm{cm}^2}$	Three non-zero column densities are simulated. These are 100 %, 60 % and 20 % of the nominal column density.
Use CSModel	true	This parameter allows to choose the energy loss model used for the simulation. *True* translates to the detailed Glück model, *False* denotes the measured Asseev parametrization [ABB+11].
Pressure	1×10^{-6} bar	Pressure inside the e-gun chamber of the rear section.
Temperature	27 K	Temperature of the gas inside the WGTS.
Electron energy	18 600 eV	Mean value of the Gaussian energy distribution for simulated electrons from the e-gun.
E-gun energy spread	0.2 eV	Assuming a Gaussian distribution of electron energies coming from the e-gun, this value describes the width σ of the Gaussian energy distribution.
Theta Max	0.5°	Maximum angle at which electrons are emitted from the e-gun. This angle is calculated in relation to the magnetic B-field.
B_A, B_S and B_{WGTS}	1×10^{-4} T, 0.0252 T, 2.52 T and 4.2 T	These values set the magnetic field along the beam tube. The first value in the center column denotes the B-Field in the analyzing plane, the second value is the B-Field at the location of the e-gun, the third and fourth values are the WGTS and pinch magnet field respectively.
Voltage Min and Max	18 550 V to 18 605 V	These two values describe the scanning range of the spectrometer voltage, i.e. the range of simulated surplus energies.
Voltage Steps	0.1 V	This value determines the voltage step size for the response function simulation, i.e. the difference between two voltage values within the range explained above. Smaller energy steps allow a finer scanning of the response functions but need accordingly more measurement time.
Number of Electrons	10^7	The number of electrons simulated for every voltage setting of the spectrometer. More electrons reduce statistical noise at the expanse of measurement time. In the simulation process, this number is statistically smeared by $\sqrt{N}$.

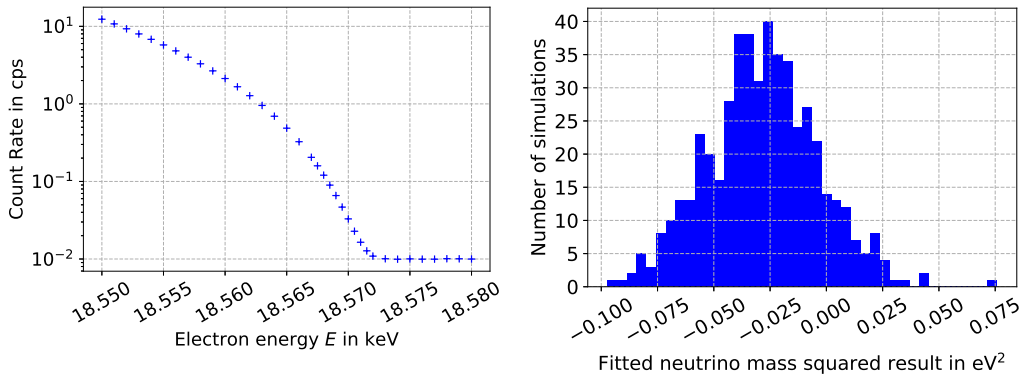

Figure 4.4.: Ensemble Test of a Deconvolved Energy Loss Function: Example data: **Left:** The Monte Carlo simulated KATRIN measurement of the integral tritium spectrum, assuming massless neutrinos. **Right:** Histogram showing the neutrino mass square fit results for simulated integral T_2 spectra for 500 energy loss function deconvolutions.
The mean value of this distribution produced with the default settings listed in Tab. A.1 far away from the target of $m_\nu^2 = 0$, proving that the method of deconvolving the energy loss function needs to be investigated and optimized.

is assumed to be the most accurate description of the effects occurring in the scattering processes, with no systematic uncertainties from a measurement. After generating the spectrum, the simulated data is used as input for a neutrino mass square fit. As the input of the Monte Carlo simulation was a massless neutrino, a good energy loss model would therefore also yield a neutrino mass square of approximately zero as fit result when all other systematic effects are neglected. Using the deconvolution result as energy loss model for the fit, it is possible to estimate the systematic errors, i.e. the neutrino mass square shift, on this deconvolution result. Performing the Monte Carlo and fitting multiple times produces a Gaussian distribution of results, see right plot of Fig. 4.4. The goal is to optimize the measurement time distribution during the response function scans in such way, that a deconvolution of the energy loss function from the response functions matches the input energy loss model. This good correspondence between model and result yields a distribution around $m_\nu^2 = 0$. distribution of results is generated, which is as close to zero as possible, and thus indicates a good measurement and deconvolution process.

4.5. KATRIN Energy Loss Simulation Results

In [HHW+17], simulation results were presented, showing the deconvolution method gives reasonable results for the energy loss function, with a neutrino mass square shift below the error budget of $7.5 \times 10^{-3}\,\mathrm{eV}^2$ [KAT05] for the systematic uncertainty from the determination of the energy loss function. Hannen et al. reported a neutrino mass square shift of (see Fig. 4.5, left plot)

$$\left(\Delta m_\nu^2\right)_{\mathrm{Hannen}} = (5.3 \pm 0.5) \times 10^{-3}\,\mathrm{eV}^2 \tag{4.19}$$

In further investigations in [Tro18], the deconvolution was investigated in terms of statistical fluctuations, yielding a significantly worse result for the mean mass shift of

$$\left(\Delta m_\nu^2\right)_{\mathrm{Trost}} = (-12.5 \pm 3.1) \times 10^{-3}\,\mathrm{eV}^2. \tag{4.20}$$

This result (see Fig. 4.5, right plot) is clearly outside the error budget of $7.5 \times 10^{-3}\,\mathrm{eV}^2$ for the energy loss function, and is nearly using up KATRIN's whole systematic error budget of $17 \times 10^{-3}\,\mathrm{eV}^2$ [KAT05].

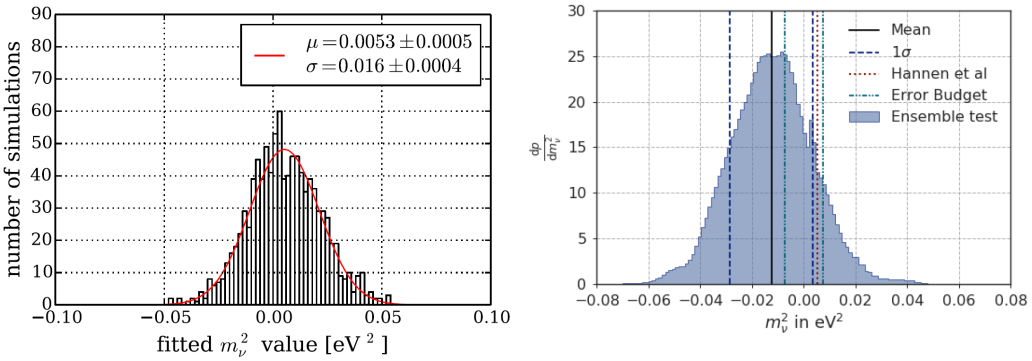

Figure 4.5.: Previous KATRIN Energy Loss Deconvolution Simulations: This graphic shows the resulting neutrino mass square shift distributions while fitting with the deconvolved energy loss function. **Left:** The result presented in the deconvolution paper by V. Hannen et al. states the deconvolution fulfills the error budget requirements from the Design Report of $7.5 \times 10^{-3}\,\mathrm{eV}^2$, graphic from [HHW+17]. **Right:** The investigations by N. Trost, showing that this method needs further investigation, as the result exceeds the error budget, graphic from [Tro18].

This mismatch has to be further investigated and the method of the deconvolution and measurement has to be optimized.
This optimization is the target of this thesis and the focus in the following chapters.

Part II.

Energy Loss Simulations and Measurements

Chapter 5

SIMULATIONS FOR OPTIMIZING THE STRATEGY FOR ENERGY LOSS MEASUREMENT

As discussed in Sec. 4.5, the latest simulations by N. Trost [Tro18] (Fig. 4.5, right) show, that the deconvolution method developed by V. Hannen et al. [HHW$^+$17] does not meet the requirement of a neutrino mass square shift below $7.5 \times 10^{-3}\,\mathrm{eV}^2$ [KAT05]. In this chapter, different strategies are investigated in simulations, for an improvement of the deconvolution of the energy loss function to meet the strict requirements. To be able to perform a large number of simulations with variable parameters (such as number of electrons or measurement time distribution), a new simulation and analysis interface is developed as described in Sec. 5.1.
In Sec. 5.2 the deconvolution results from Hannen and Trost are reconstructed using simulations based on the default setting. Also the merging method described in Sec. 5.1 is tested by merging simulations according to the default setting.
There are two steps of optimization. First, the result needs to be optimized to achieve the requirements according to the error budget. Afterwards, the measurement time should be minimized without significantly compromising the optimized result.
Due to the limited measurement time available during the neutrino mass measurements (as well as during commissioning periods like STS-IIIa, discussed in Ch. 6) a strong increase of the total statistics is not possible, which motivates the investigation of different time saving approaches. The results of different measurement time distributions in the energy loss measurements and scanning strategies are discussed in Sec. 5.3 and show the limits of the SVD deconvolution method and the systematic influence of the measurement strategy.
In Sec. 5.4 the chapter will be concluded by a brief summary of the simulation results and optimization strategy.

5.1. Development of a Simulation and Analysis Interface

Investigation and final optimization of the results from [HHW$^+$17, Tro18] require a detailed investigation of the parameters in the response function simulations.
In order to be able to employ a more detailed and variable measurement time distribution, the simulation and analysis chain has to be extended compared to the default procedure described in Sec. 4.3. Starting with a large set of simulated response functions with

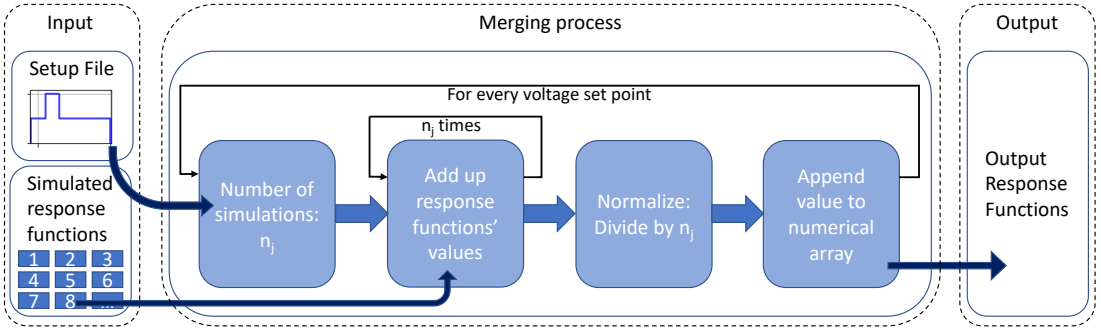

Figure 5.1.: Schematic View of the Merging Process During Simulation: This schematic view shows the merging process as described in Sec. 5.1. A number of simulated response functions according to a given setup file is picked and merged, to obtain higher statistics in certain regions and to be able to quickly simulate different settings. This process takes only several seconds up to a few minutes, depending on the individual setup used.

10^5 electrons per voltage step each, a merging process is introduced, to obtain the desired statistics for each retardation voltage set point individually, from a given setup file where the desired number of electrons is listed for every voltage set point. With these merged files the KEloss analysis chain is followed step by step to investigate the quality of the deconvolved energy loss function as discussed in Sec. 4.4.
Another advantage of the introduced method, compared to simulating every single response function individually, is an improvement of the workflow. As the deconvolution process requires four response functions at different column densities, with the default settings of 10^7 electrons for every voltage set point with voltage steps of 0.1 eV, the simulation process can take up to 28 CPU hours for the nominal column density[1] of $5 \times 10^{17}\ \frac{1}{\mathrm{cm}^2}$, a faster method for the investigation of statistical effects is needed.
Simulated response functions are numerically combined from many response functions with lower statistics, which decreases the simulation time during the investigations, as this merging process can be performed without significant time consumption. The simulation and analysis chain is described in the following and illustrated as a schematic diagram in Fig. 5.1.

Simulation

The first step for investigating the energy loss measurement and deconvolution procedure is the simulation of a large set of response functions. In order to be able to investigate a reasonable range of statistics in each surplus energy data point, these simulations use a mean of 10^5 simulated electrons[2] for each voltage step.
In this chapter every setup is tested with 500 independent deconvolutions. For the investigation of the influence of overall statistics (see Sec. 5.3.1), a maximum of 10^8 electrons in every voltage step is used. With the demand of being able to investigate up to 500 independent response functions with an equivalent of 10^8 electrons in every voltage set point for each of the four column densities, $500 \cdot 10^8/10^5 = 500,000$ simulations with 10^5 electrons per voltage set point are needed. With this large set of simulations, every statistical investigation in the limits of 10^5 to 10^8 electrons is possible.

[1] With a higher column density, more scattering processes occur, thus also the simulation time for the nominal column density of $5 \times 10^{17}\ \frac{1}{\mathrm{cm}}$ is higher, compared to the simulation time with zero or intermediate column densities.
[2] See the parameter *Number of Electrons* in Tab. 4.1 for further explanation.

Merging Process

For investigating different measurement time distributions, the generated response functions of the simulation step described above need to be merged in order to be able to create the desired number of simulated electrons in each individual voltage step.
First, a setup file is needed, to define how many electrons per voltage step should be considered for a given surplus energy range. These setup files consist of two columns, where the first column defines the surplus voltage, and the second one defines the number of response functions to be used for this individual voltage set point.
The merging process is performed for each voltage set point individually. The voltage points are denoted with index j. Reading the number n_j of used simulations from the setup file, a new merged response function file is built by adding up n_j randomly chosen simulated response functions. In order to keep the normalization correct, the transmission probabilities in the response functions need to be divided by n_j as final step of the merging procedure.
This process yields a normalized response function with variable statistics for each voltage set point, according to the loaded setup file. Due to the variation of the overall number of simulated electrons in different regions of the response function, the statistical error also will be larger or smaller in regions with less or more simulated particles, respectively, as $\sigma(n_j) \propto \sqrt{n_j}$ according to Poissonian statistics.
After the merging process, the resulting output response functions are normalized, to give the transmission probability for an electron with a given surplus energy.

Matrix Inversion and SVD Deconvolution

Using these merged files as input, the scattering matrix is inverted, as described in Sec. 4.4. This step generates the required scattering functions ϵ_i, which are mathematically built from a convolution of the spectrometer's transmission function and the energy loss function, that will be deconvolved from the single scattering function ϵ_1.
The single scattering function ϵ_1 is now used as input for the actual deconvolution of the energy loss function. Here again, as described in Sec. 4.4, the numerical deconvolution is performed by singular value decomposition of the matrix describing the convolution process of the e-gun transmission function, which is equivalent to the response function with an empty source, with the energy loss function of electrons in tritium.

Monte Carlo Simulation and Analysis

After the deconvolution was performed, an ensemble test (see Sec. 4.4) of the result is applied to check the result.
First, a series of one thousand Monte Carlo simulations of the total KATRIN neutrino mass measurement period is done, assuming $m_\nu = 0$. This yields tritium β-spectra where the electrons undergo scattering processes and energy loss according to the energy loss model by F. Glück.
These simulated spectra are now fitted with the deconvolved energy loss function as input curve. These fits yield a histogram with the fitted neutrino mass squares. As the Monte Carlo simulation assumed massless neutrinos, the mean value of these fitted masses can be used to assess the quality of the deconvolution result. The goal is to achieve a deconvolution result, yielding a mean value of $\Delta m_\nu^2 = 0\,\mathrm{eV}^2$, which translates to a 'good' deconvolved energy loss function.
For this investigation, only the mean value is important, as the width of the distribution has its origin in the statistical uncertainty of the KATRIN neutrino mass measurement.

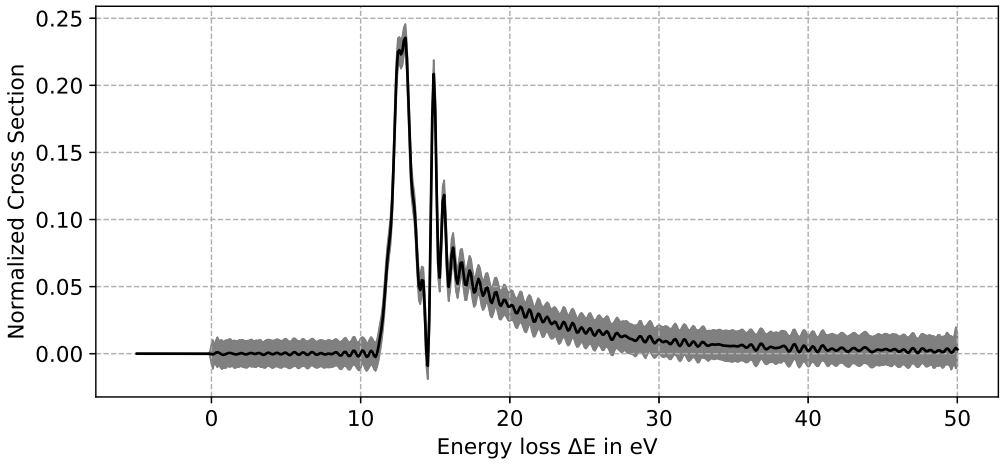

Figure 5.2.: Energy Loss Deconvolution with Error Band: The black curve shows the average of 500 deconvolution results from simulated response functions with 10^7 electrons for every voltage set point. The gray error band shows the statistical standard deviation from the 500 individual deconvolution processes determined for every data point individually. The normalization is chosen according to $\int_{E_{\min}}^{\max} \mathrm{d}\Delta E\, f(\Delta E) = 1$.

Statistical Fluctuations in the Deconvolution Process

In order to investigate the stability of the deconvolution result for a given setting of simulation parameters, the procedure described above is performed 500 times for each tested parameter setting. The results are collected, and can be analyzed in terms of mean neutrino mass square shift and width of the distribution.
For this statistical investigation, the given response functions are merged in different combinations according to the same setup file, i.e. the same measurement time distribution. By using different merged curves, the deconvolution results slightly vary from each other. Various deconvolutions produce different fit results of the Monte Carlo tritium β-spectrum, resulting in again multiple mean values for the fitted neutrino mass squares. The width of the neutrino mass square distribution gives the statistical stability of the deconvolutions with the used measurement time distribution during the energy loss measurements, defined by the setup file applied during the merging process.
Additionally, this procedure allows to give a statistical error band for a deconvolution of a given measurement time distribution, as shown in Fig. 5.2. The error band is calculated for every data point individually and describes the 1σ deviation. This figure shows the mean of 500 deconvolution results for the default settings of 10^7 electrons in every voltage set point and voltage steps of 0.1 eV.

5.2. Deconvolution Results for Default Settings

Before the optimization, the results of the deconvolution using the default settings have to be known for comparison. As described in Sec. 4.5, N. Trost found that the shift of the neutrino mass square caused by the determination of the energy loss function can be described by a Gaussian distribution with a mean value of $\Delta m^2 = -12.5 \times 10^{-3}\,\mathrm{eV}^2$, and a width of $3.1 \times 10^{-3}\,\mathrm{eV}^2$ [Tro18]. The simulation parameters used as default setting as proposed in [HHW$^+$17] are listed in the appendix in Tab. A.1.
First, 500 simulations are performed with 10^7 electrons simulated at once, without the merging process described in Sec. 5.1. Performing the simulations with the default parameters shown in Tab. A.1 yielded a resulting mean for the neutrino mass square shift

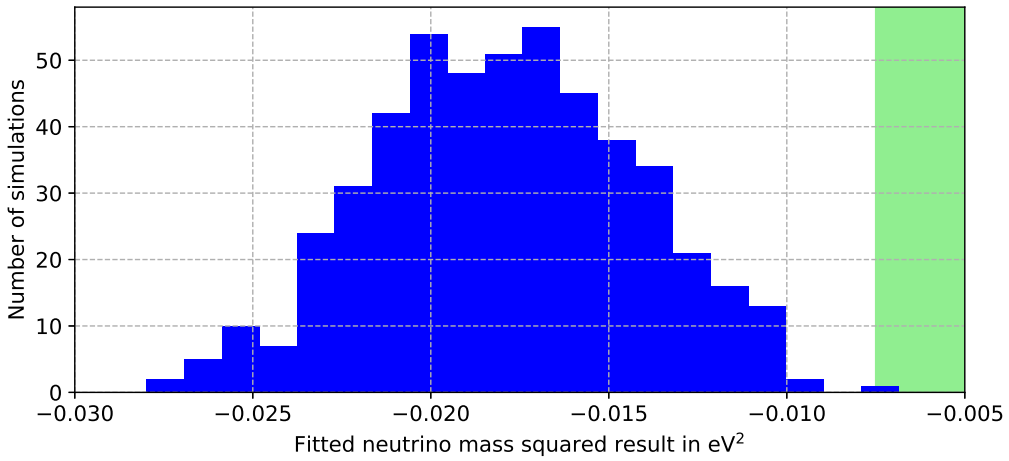

Figure 5.3.: Ensemble Test of Simulations under Default Settings: With a mean neutrino mass square shift of $\Delta m_\nu^2 = -17.9 \times 10^{-3}\,\mathrm{eV}^2$ and a width of the distribution of $3.7 \times 10^{-3}\,\mathrm{eV}^2$, only one of 500 simulations yields a result meeting the error budget of $\pm 7.5 \times 10^{-3}\,\mathrm{eV}^2$, indicated by the green area in the plot. This result confirms the problem found by N. Trost [Tro18], that the deconvolution method does not yield results matching the design report requirements.

of

$$\Delta m^2 = (-17.9 \pm 3.7) \times 10^{-3}\,\mathrm{eV}^2$$

with $\pm 3.7 \times 10^{-3}\,\mathrm{eV}^2$ being the sigma width of the distribution. This result does not match the one by N. Trost exactly, but confirms the problem of not meeting the requirement of $|\Delta m^2| \leq 7.5 \times 10^{-3}\,\mathrm{eV}^2$. This distribution corresponds to only 0.2 % of results being in the required range of the error budget, see Fig. 5.3. Additionally to the number of simulations inside the error budget, the maximum simulated neutrino mass square shift squared is $-28.0 \times 10^{-3}\,\mathrm{eV}^2$, which is about a factor of 4 too high, compared to the error budget.
Also in this step, a check of the merging method, described in Sec. 5.1, was performed, by merging 100 simulations with 10^5 electrons in every voltage set point to obtain the standard setting of 10^7 electrons again. The result of this merged default setting was meeting the results from 10^7 electrons as one single simulation inside their uncertainty. The merged simulations yielded a mean neutrino mass square shift of

$$\Delta m^2 = (-18.6 \pm 4.0) \times 10^{-3}\,\mathrm{eV}^2.$$

This slightly broader distribution leads to 0.6 % of results meeting the error budget, but also to a larger maximum shift of $-29.8 \times 10^{-3}\,\mathrm{eV}^2$.
This result of matching neutrino mass square shifts confirms the software-wise approach to merge files to quickly generate simulated response functions with a high number of electrons.

5.3. Variation of Statistics and Voltage Steps in the Simulated Data

In order to reduce the impact of the deconvolution of the energy loss function on the neutrino mass square result, the two most promising simulation and measurement parameters for adjustment are the number of electrons for every voltage set point, and the size of the voltage steps. The influence of these two parameters are investigated in this section, starting with the investigations of the statistical influence of the total number of simulated electrons for each voltage step in Sec. 5.3.1, followed by a search for ranges in the response functions with the largest sensitivity to statistics in the deconvolution and analysis chain in Sec. 5.3.2. The results with a focused simulation in the regions of high sensitivity are presented in

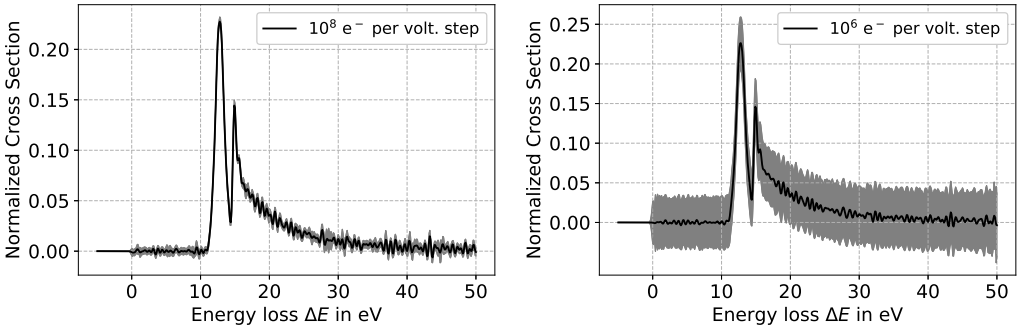

Figure 5.4.: Statistical Variations of Energy Loss Function Deconvolution: Influence of different number of electrons on the deconvolution of the energy loss function. **Left:** 500 deconvolutions with response functions using 10^8 electrons per voltage step. **Right:** 500 deconvolutions with response functions using 10^6 electrons per voltage step. The error band in both cases indicates the standard deviation for every individual data point. This standard deviation is 8 times higher for the smaller total number of simulated electrons.

Sec. 5.3.3. In Sec. 5.3.4, the systematic influence and effects of finer or larger voltage steps are investigated.

5.3.1. Variation of the Overall Statistics

The most straightforward approach to investigate the statistical influence on the neutrino mass square shift is to increase the total statistics in the simulations. With an estimated e-gun electron rate of 25 kcps as was achieved in test measurements, the measurement of 551 voltage set points[3] with 10^7 electrons in every step, the default setting measurement of a response function for one column density would take roughly 2.5 to 3 days, yielding a total measurement time of 10 to 12 days. Increasing this value by a factor of 10 should be avoided. These simulations with total statistics 10 times higher compared to the default setting thus are a proof of principle investigation, to determine if increasing the total statistics could lead to a better result. For the approach with increased measurement time the hardware requirements are more difficult to fulfill, as the electron rate and the rate stability needs to be kept constant over much longer time.
By the simulations performed in this section a minimal required statistical precision to meet the requirements of a neutrino mass square shift smaller than $7.5 \times 10^{-3}\,\mathrm{eV}^2$ can be found.
After the deconvolution of the simulated response functions with 10^6 and 10^8 electrons in every voltage step, this narrower spread of energy loss functions, shown in Fig. 5.4, can be transformed to a narrower distribution of m_ν^2 fit results, as shown in Fig. 5.5. Although the distribution is roughly a factor of 5 narrower (see Fig. 5.5) in the case of 100 times higher statistics in the response function simulations, the position of the mean value remains nearly unchanged. The results of the ensemble tests of these simulations are shown in Tab. 5.1.

Further investigations with other electron numbers in the range of 10^5 to 10^8 electrons, with the neutrino mass square shift shown in Fig. 5.6, also do not show any correlation between the mean neutrino mass square shift and the overall number of electrons simulated in each voltage step in the response functions. This suggests the neutrino mass square shift to occur for systematic reasons arising from the deconvolution process and not due to missing statistics.

[3] 551 data points result from the default settings of a measured range of surplus energy from −5 eV to 50 eV in steps of 0.1 eV

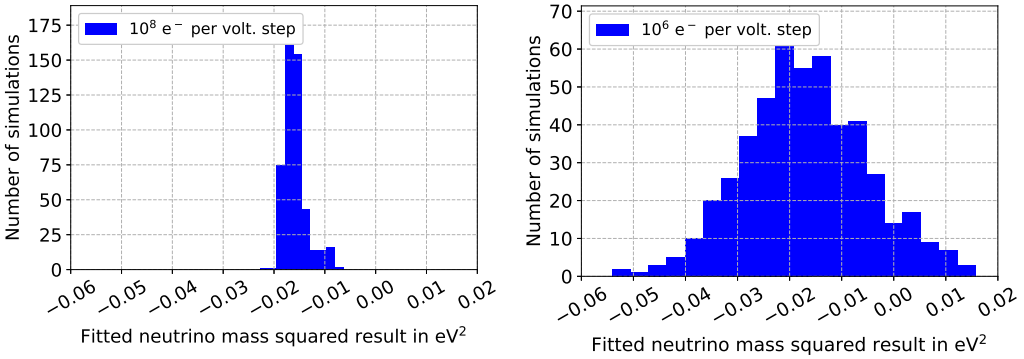

Figure 5.5.: Neutrino Mass Square Fits for High and Low Statistics: Influence of statistical fluctuations in the response functions on the neutrino mass square fit. **Left:** Results of 500 fits with response functions using 10^8 electrons per voltage step. **Right:** Results of 500 fits with response function using 10^6 electrons per voltage step.

Table 5.1.: Ensemble Test Results for 10^6 and 10^8 Electrons in every Voltage Step: This table shows, that increasing the overall amount of simulated electrons for every voltage step does not improve the mean value of the neutrino mass square shift. The σ width of the distribution can be narrowed down by increasing the overall number of electrons simulated in every voltage step of the response functions.

e$^-$ per Volt. Step	Mean Value	σ Width
10^6	$-15.9 \times 10^{-3}\,\mathrm{eV}^2$	$11.9 \times 10^{-3}\,\mathrm{eV}^2$
10^8	$-17.0 \times 10^{-3}\,\mathrm{eV}^2$	$2.2 \times 10^{-3}\,\mathrm{eV}^2$

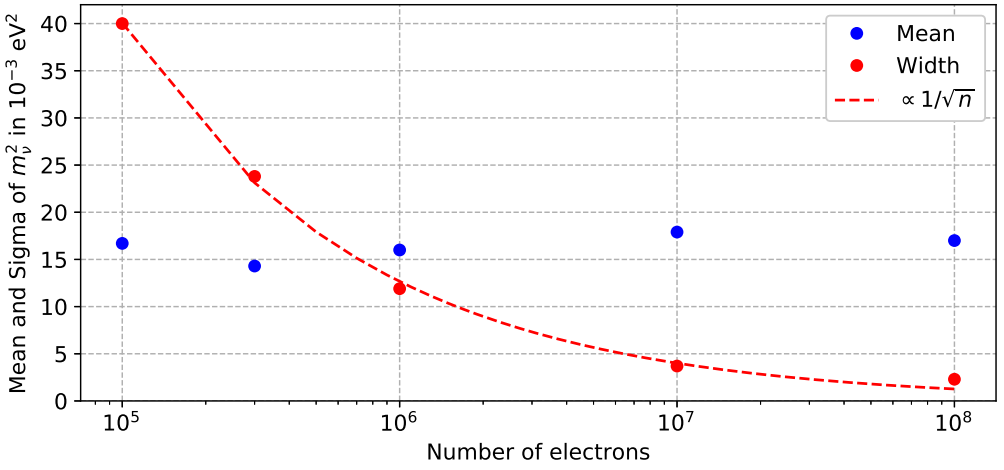

Figure 5.6.: Influence of Overall Statistics on Fit Results: Influence of higher statistic during the energy loss measurement on the neutrino mass square fit result. **Blue:** The mean value of many fits does not change significantly. **Red:** The Gaussian sigma width of the individual distributions gets smaller with higher statistic. As the dashed line indicates, the width of the distribution follows a $\propto \frac{1}{\sqrt{n}}$ relation.

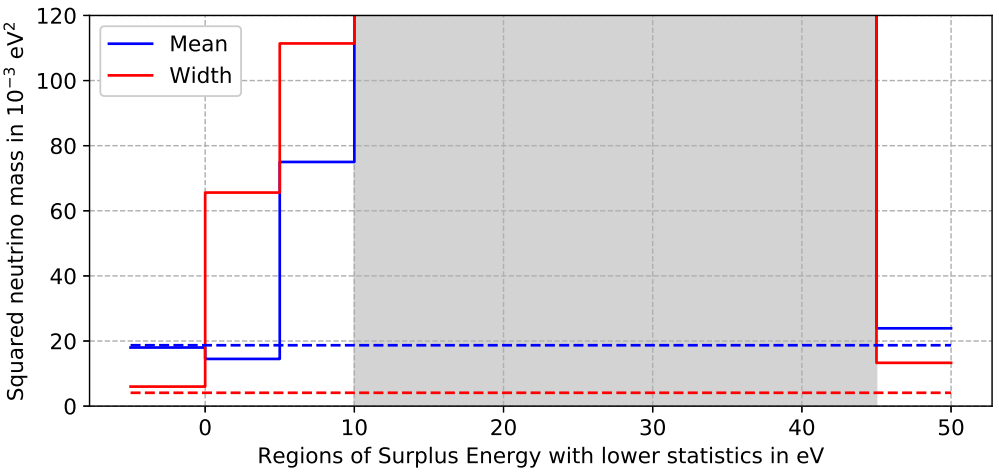

Figure 5.7.: Search for Sensitive Regions in Response Functions: This plot shows the ensemble test results using energy loss functions deconvolved from simulations with lower statistics in 5 eV regions, in order to find sensitive regions of the response functions. **Blue:** Absolute values of the mean values of the mass fit. **Red:** the Gaussian sigma width of the mass fit distribution. The dashed lines show the values obtained without a region with lower statistics, i.e. the default setting. The gray area indicates regions, where lowering the statistics yielded non-converging fits.

As the σ-width of the Gaussian distributions is a statistic effect, the red points in Fig. 5.6 follow roughly a $\propto \frac{1}{\sqrt{n}}$ relation, with n being the total number of electrons.
As shown in Fig. 5.5, even increasing the statistics by a factor of 10 does not yield better results than the default setting, as in this case, not a single result for the neutrino mass square shift is below the error budget of $7.5 \times 10^{-3}\,\mathrm{eV}^2$. Thus increasing the overall statistics is not a sufficient method for the optimization of the measurements with respect to the neutrino mass square shift. Nevertheless, the deconvolved energy loss functions show less fluctuations and noise for a higher number of electrons in the response functions, which can narrow down the distribution of neutrino mass square shifts.

5.3.2. Sensitive Region Investigation

The proposed method by Hannen et al. of equally distributed measurement time over the entire measurement range for each of the four column densities may not be the best strategy in terms of minimizing the neutrino mass square shift. The response functions are suspected to have regions, where very little information about the energy loss function can be extracted (e.g the plateaus in the region of 0 eV to 10 eV). Thus redistributing the measurement time for the standard measurement strategy may increase the quality of the deconvolution by spending most of the total available measurement time in the sensitive regions. For a systematic investigation of an optimized measurement time distribution, dedicated investigations of the contribution of different sections of the response functions are required.
To find these sensitive regions, a scan is performed with lower statistics in short ranges of the response functions of 5 eV each. With the default settings as starting point, the number of electrons simulated in these regions is lowered by two orders of magnitude. Using this approach with such high differences between the higher and lower statistics regions yields very strong differences between the default setting and the modified one. Thus it is possible to search for regions in the response functions, which do not worsen the deconvolution when not measured with high statistics, in order to save measurement time.
As shown in Fig. 5.7, the simulations with lower statistic in most of the regions yield a neutrino mass square shift that is significantly larger than the value for the default setting.

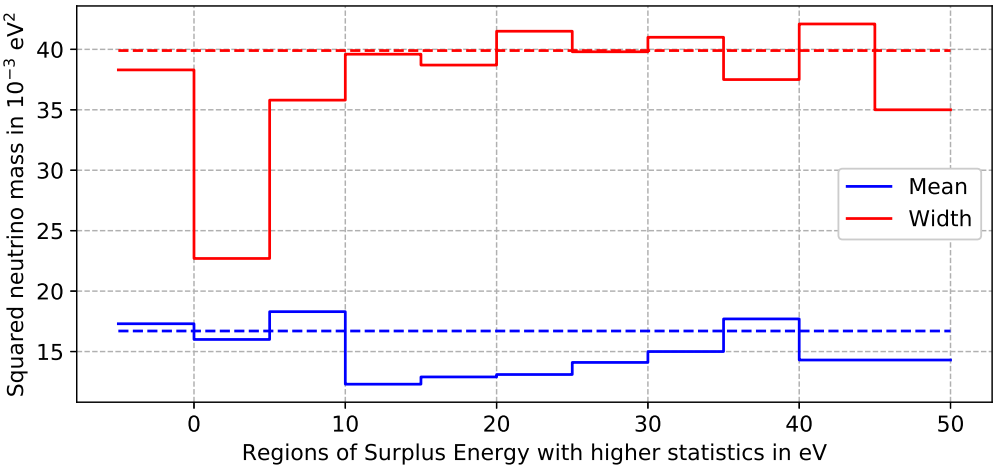

Figure 5.8.: Searching for Sensitive Regions: This plot shows the ensemble test results, when increasing the statistics in 5 eV regions by a factor of 100. **Blue:** Absolute values of the mean values for the mass fit. **Red:** the sigma width of the mass fit distribution. The dashed lines indicate the results with no regions of higher statistics, in this example 10^5 electrons in every voltage set point.

Only the regions below 5 eV and above 45 eV of surplus energy do not change the value significantly. For a lower statistic in the range of 5 eV to 10 eV the deconvolution and ensemble test yields an absolute mean neutrino mass square shift of 75×10^{-3} eV, which is about 4 times higher than the comparison value of 18.6×10^{-3} eV for the default setting. Also Fig. 5.7 shows that lowering the statistic in the regions of 10 eV to 45 eV (again changing the statistics on 5 eV intervals) yields even worse results where the neutrino mass square fits do not converge, indicated by the gray area in Fig. 5.7.
These results do meet the expectations, as the energy loss of electrons, according to the Glück model in the right plot of Fig. 4.1, is mainly in the region of 11 eV to 16 eV. This range translates to a region of 11 eV to 48 eV for triple scattering, which is taken into account by investigating three non-zero column densities (see Sec. 4.3 and [HHW$^+$17]).
In support to this, a similar scan is performed, where 10^5 electrons per voltage step are used as basis setting and the short regions are scanned with higher statistics (10^7 electrons per voltage step). This scan is performed to find 5 eV intervals where higher statistics significantly decreases both, the mean neutrino mass square shift and the width of the distribution. The results are shown in Fig. 5.8.
Fig. 5.8 shows a neutrino mass square shift lowered by 26 % when using higher statistics in the region of 10 eV to 15 eV. Again, this behavior can be explained by the shape of the energy loss function itself, see Fig. 4.1. In the region below 10 eV there is no contribution from inelastic scattering, and thus the region from 11 eV to 22 eV of surplus energy only can be influenced by single scattering processes. As the single scattering function ϵ_1 is used to deconvolve the energy loss function, this has to be known as precise as possible to generate deconvolution results with neutrino mass square shifts meeting the error budget. The results of this investigation show, that a high number of electrons (i.e. high measurement time) in the preferred region of $E_S = 11$ eV to 22 eV should be chosen to decrease the associated neutrino mass square shift, whereas the plateau region of the response functions from 0 eV to 10 eV can be measured with lower statistics, without a significantly higher neutrino mass square shift.

5.3.3. Non-Flat Measurement Time Distributions

Scanning the response functions with a flat measurement time distribution is the simplest possible approach and thus an optimization is assumed by redistributing the given

measurement time with a preference for the sensitive regions. Taking into account the previous results, the next approach is to decrease the statistics in the insensitive regions and increase the number of voltage set points, where significant improvement is expected from the sensitive region scans.
First, as shown in Sec. 5.3.2, the measurement time for energies below $E_{\mathrm{surp}} = 5\,\mathrm{eV}$ can be shortened, with less statistic and less voltage steps, as this region did not cause any significant changes to the ensemble test results, as well as $E_{\mathrm{surp}} \geq 45\,\mathrm{eV}$. Further, a detailed investigation with good resolution and high statistics is aimed for in the region of single scattering, i.e. 11 eV to 22 eV, as the single scattering function is the basis for the deconvolution process (see Sec. 4.3).
With longer measurement time in the single scattering region, time needs to be saved in the rest of the spectrum. It is important to know, how much time can be distributed into the important part of the response function, while keeping the overall measurement time constant. Assuming only the region of 11 eV to 22 eV being measured, it is possible to estimate the maximum number of electrons compared to the default setting in this range to a factor of

$$n_{\mathrm{max}} = \frac{55\,\mathrm{eV}}{12\,\mathrm{eV}} = 4.6 \tag{5.1}$$

with the very optimistic assumption, that the other regions do not contribute to the result at all and thus do not need to be measured, which is of course not the case, as shown in Fig. 5.7 and 5.8. Nevertheless, the factor calculated in Eq. (5.1) can be used as an approximation, when the rest of the response function is measured with 100 times less electrons in each voltage steps.
Integrating the number of electrons in each voltage set point over the total measurement range gives a good estimation of the measurement time, with normalization to the default measurement with 10^7 electrons every 0.1 V. For two different ranges, the relative change of measurement time can be calculated via

$$t/t_0 = \frac{N_1}{N_0} \cdot \frac{(\Delta U)_1}{(\Delta U)_{\mathrm{tot}}} + \frac{N_2}{N_0} \cdot \frac{(\Delta U)_2}{(\Delta U)_{\mathrm{tot}}}, \tag{5.2}$$

where t_0 is the measurement time needed for the default setting, $N_{1,2}$ are the numbers of electrons in units of the number in the default setting (i.e. 10^7). The fraction $(\Delta U)_{1,2}/(\Delta U)_{\mathrm{tot}}$ denotes the length of the regions compared to the total measurement range with $(\Delta U)_{\mathrm{tot}} = (\Delta U)_1 + (\Delta U)_2$. This equation can be extended to any number of individual regions. With the above mentioned example of high statistics in the region of only single scattering, one can calculate the maximum number of electrons in the remaining regions in dependence of the number of electrons in the focused single scattering region to

$$N_2 = \frac{55\,\mathrm{eV}}{43\,\mathrm{eV}} - N_1 \cdot \frac{12\,\mathrm{eV}}{43\,\mathrm{eV}}. \tag{5.3}$$

From the investigations and results described in Sec. 5.3.2 - 5.3.4 different measurement time distributions are derived as shown in the appendix.
According to Eq. (5.3), an increase of the overall statistics in the most sensitive regions (see Fig. 5.8) of the spectrum is not possible if the total measurement time should remain constant. Using this equation in an adjusted form to calculate the maximum factor of statistics for an increase in the region 10 eV to 15 eV, as shown in Sec. 5.3.2, a maximum statistics rise to a factor of 11 would be possible without increasing the overall measurement time. The redistributed simulations presented in Sec. 5.3.2 using 10^8 electrons in the focus region of 10 eV to 15 eV and 10^6 electrons in the rest of the response spectrum, as indicated in Fig. 5.9, will take the same amount of time as measuring a uniformly distributed number of 10^7 electrons, according to Eq. (5.2). The measurement focused on one region yet does not yield strongly improved results in comparison to the constant distribution with the

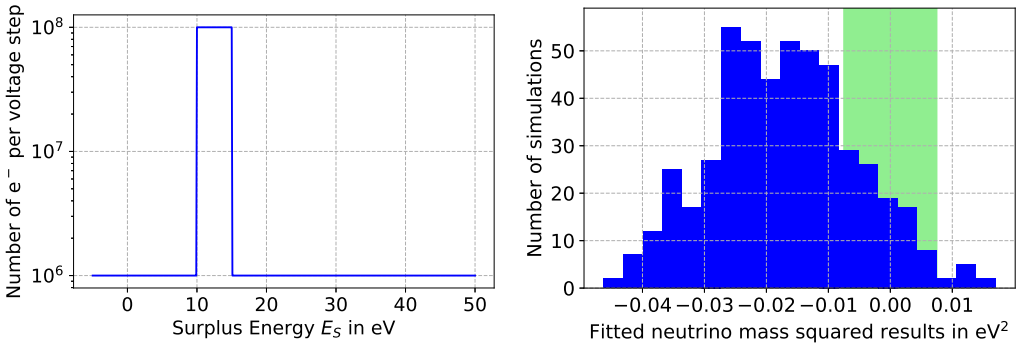

Figure 5.9.: Focused Measurement Time Distribution: Result of a focused measurement time distribution during the energy loss measurement. **Left:** The measurement time distribution with 10^8 electrons in the range of 10 eV to 15 eV and 10^6 electrons in the rest of the spectrum, resulting in a total measurement time equivalent to a measurement with 10^7 electrons over the total spectrum. **Right:** The ensemble test results for this distribution shows a broader distribution of neutrino mass square shifts, compared to the default setting. About 19 % of the simulations are inside the error budget indicated by the green area.

same total time. In this case, the optimal region with increased statistics as described in Sec. 5.3.2 results in a neutrino mass square shift of

$$\Delta m_\nu^2 = (-17.1 \pm 11.6) \times 10^{-3}\,\mathrm{eV}^2,$$

whereas the flat distribution with the same overall time yields $\Delta m_\nu^2 = (-17.9 \pm 3.7) \times 10^{-3}\,\mathrm{eV}^2$. The simulation with a constant amount of electrons over the entire spectrum thus gives a much narrower distribution of neutrino mass square shift results, with a slightly higher mean value.

In a further analysis, the full region where only single scattering occurs (11 eV to 22 eV), was scanned with an increased statistics of 10^8 electrons. By increasing the statistics in this region by a factor of 10 compared to the default settings, and lowering the statistics in the rest of the spectrum by a factor of 10, the total measurement time is increased by a factor of 2 according to Eq. (5.2). Scanning this broader range of the response functions with higher statistics yields similar results of $\Delta m_\nu^2 = -17.6 \times 10^{-3}\,\mathrm{eV}^2$ with a sigma width of $11.5 \times 10^{-3}\,\mathrm{eV}^2$ (see Fig. 5.10), and thus also is not sufficient for a good investigation of the energy loss function. Other distributions were tested but showed inferior results and therefore are not discussed here, even though a brief summary is given in the appendix in Tab. A.3.

These results demonstrate that varying only the number of electrons for individual voltage set points is not the best way to achieve better deconvolution results, since the trade off between having more statistics in the region of interest than in the other regions of the transmission causes an unpredictable change of the width of the distribution. As the simulations show, the broadening due to lower statistics dominates and makes the results even worse compared to a flat measurement time distribution. Although the focusing on the most sensitive region of 10 eV to 15 eV shows 19.5 % of the simulations being inside the error budget, which is more than for the default setting, the largest simulated neutrino mass square shift is $-47.7 \times 10^{-3}\,\mathrm{eV}^2$, which is significantly larger than the maximum shift for the default setting of $-28.0 \times 10^{-3}\,\mathrm{eV}^2$ and thus this approach is not a useful improvement to the default setting.

With no improvement achieved by redistributing the measurement time onto the given voltage set points, the second approach is to redistribute the individual voltage data points. In order to be able to vary the voltage steps by applying the simulation method as described in Sec. 5.1 for the variation of the number of electrons in each voltage step, the voltage

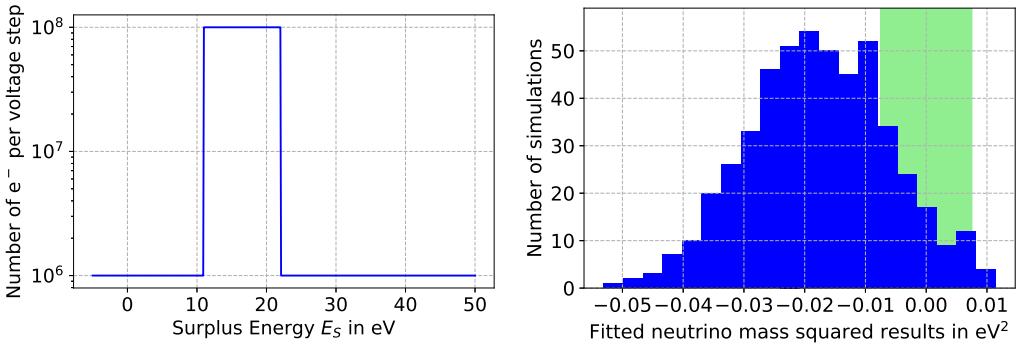

Figure 5.10.: Focused Measurement Time Distribution: Result of a focused measurement time distribution during the energy loss measurement. **Left:** The measurement time distribution with 10^8 electrons in the range of 11 eV to 22 eV and 10^6 electrons in the rest of the spectrum, resulting in a total measurement time a factor of 2 higher than for default settings. **Right:** The ensemble test results for this distribution shows a broader distribution of neutrino mass square shifts, compared to the default setting. About 21.5 % of the simulations are inside the error budget indicated by the green area.

set points not used need to be interpolated from the neighboring ones. The reason for this approach is that the deconvolution process requires the four input response functions binned in exactly the same way. This means either all four response functions need to have a broader binning in the same range, or single response functions with broader binning need to be interpolated in between.
The best tested setup is not an improvement to the neutrino mass square shift results, but shows potential to decrease the measurement time dramatically by a factor of two by leaving out many measurement points in the spectrum. The approach is to measure only the transmission edge and the single scattering processes. Thus, the regions of the response functions that do not need a fine scanning are considered to be measured with voltage steps of $\Delta E = 1\,\mathrm{V}$. These regions are the area below the transmission edge ($E_{\mathrm{surp}} < -0.5\,\mathrm{eV}$), the plateau from 0.5 eV to 11 eV of surplus energy and the region of $E_{\mathrm{surp}} > 30\,\mathrm{eV}$, where single scattering contributes to the energy loss only in the region of the ionization tail. The number of electrons simulated is assumed to be constant for the entire spectrum with 10^7 electrons for every voltage set point.
Further tested settings and measurement time distributions are briefly summarized in the appendix with the results in Tab. A.3 and shown in Fig. A.5 - A.7.

5.3.4. Variation of Voltage Steps in Scanning

As shown in Sec. 5.3.1, even a dramatic overall increase of statistics by a factor of 10 compared to the default setting cannot decrease the neutrino mass square square shift significantly. Therefore another approach for optimization is investigated, which is to set finer or larger voltage steps for the measurement of the response functions. Finer voltage steps are supposed to provide a more detailed energy resolution of the different features of the response function, such as the influence of the excitation states of tritium molecules occurring in the energy loss function.
To investigate the influence of finer voltage steps in the response functions, additional simulations are needed. Similar to the approach for the investigation of different overall statistics (Sec. 5.3.1), three settings with different voltage steps are tested. Starting with the default value of $\Delta U_{\mathrm{spec}} = 0.1\,\mathrm{V}$ one setting with finer binning (0.05 V) and one setting with larger steps (0.2 V) are checked. For this investigation, 10^6 electrons were used in each voltage set point. Although the default value for comparison is 10^7, the analyses in Sec. 5.3.1 showed, that a reduced statistics does not change the mean value of the neutrino

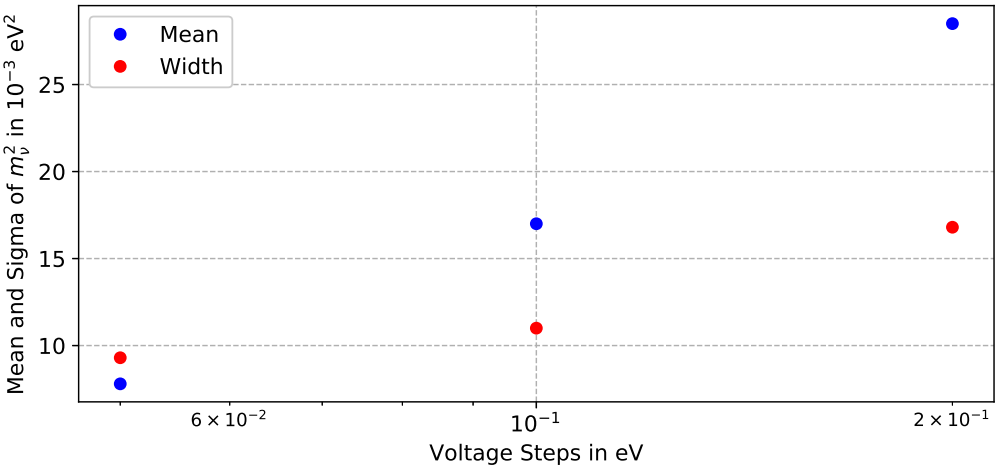

Figure 5.11.: Influence of Voltage Step Size on Fit Results: Influence of finer and larger voltage steps during the energy loss measurement on the neutrino mass square fit result. **Blue:** The mean value of 500 fits gets smaller with finer voltage steps. **Red:** The statistical sigma width of the individual distributions gets smaller with finer voltage steps.

mass square shift significantly, thus using only 10^6 electrons is justified for the reason of saving simulation time. The results of the ensemble tests are shown in Fig. 5.11, indicating a lowered mean value and narrower distributions for finer binning, as one would expect from the finer sampling.
Performing again 500 neutrino mass square fits with the deconvolutions generated from response functions with 10^6 electrons and a finer binning of 50 meV, the mean value of the neutrino mass square distribution is

$$\Delta m^2 = (-7.8 \pm 9.3) \times 10^{-3}\,\mathrm{eV}^2.$$

This translates to 42 % of results being inside the error budget of $\pm 7.5 \times 10^{-3}\,\mathrm{eV}^2$, which is already an improvement of factor 2, compared to the default setting, even though the overall statistic is still a factor 5 lower. From these results, it can already be concluded, that the best way to measure and deconvolve the energy loss function yielding neutrino mass square shifts within the error budget is a combination of high statistics and fine voltage scans, under the condition of keeping the total measurement time the same as for the default settings.
This optimal ratio between fine scanning of the spectrum and measuring every point with high statistics has to be found and investigated further. Therefore, five sets of 500 simulations each are performed, using a total measurement time that remains constant and equivalent to 10^6 electrons per voltage step with voltage steps of 0.1 V. The measurement time is distributed towards more statistics per bin or more voltage steps with lower statistics. Choosing again 10^6 electrons, for the reasons mentioned above, in voltage steps of 0.1 V as starting point, provides a total measurement time that is proportional to the statistic in every voltage set point and also to the inverse of the voltage step size yielding $\Delta U_{\mathrm{spec}} \propto n$. Figure 5.12 shows the ensemble test results for constant total measurement time resulting in voltage step size antiproportional to the number of electrons in every voltage set point. For the investigation of the voltage step size yielding zero neutrino mass square shift, an overall statistics of 10^6 is sufficient, as Sec. 5.3.1 showed no difference in the mean value of the distribution. Lower statistics was chosen in this step, as varying the voltage step size needs new simulations for every data point, and thus an equivalent of 10^7 electrons would increase simulation time by a factor of 10.
As can be seen in Fig. 5.12, the mean value of the distribution of fit results crosses zero at voltage steps of about 40 mV. This value, corresponding to 4×10^5 electrons in every

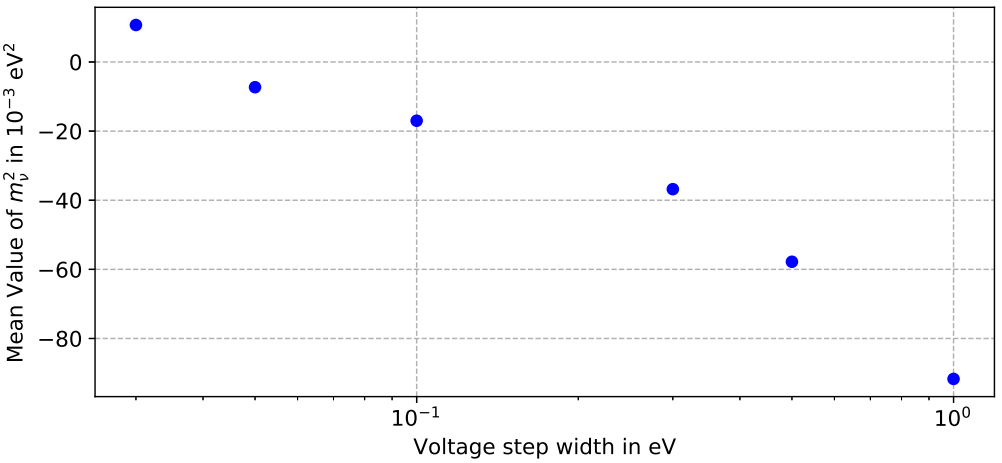

Figure 5.12.: Ensemble Test Results for Constant Measurement Time with Variable Voltage Steps: Mean neutrino mass square shift for a total number of electrons in the whole response spectrum equivalent to 10^6 electrons with voltage steps of 0.1 eV. In this graphic, finer voltage steps correspond to less electrons per voltage step.

voltage set point, is expected to be the best setting and thus this setup is validated with simulations with voltage steps of 40 mV and 4×10^6 electrons per bin, resulting in a total measurement time equivalent to the default setting, with the results shown in Fig. 5.13. The results in Fig. 5.13 show a distribution of neutrino mass square shifts with a mean value of

$$\Delta m^2 = (3.1 \pm 4.5) \times 10^{-3}\,\mathrm{eV}^2,$$

with the uncertainty again denoting the sigma width of the distribution. Checking again, how many results are inside the given error budget shows this best setting to have 83.4 % of the neutrino mass square shift results inside the error budget, which is an improvement by a factor of over 100 in comparison to the default setting of 10^7 electrons each 0.1 eV with 0.6 % meeting the requirements.
This result turned out to be the best setting for an integral energy loss measurement as investigated in this thesis, as it preserves the total time of measurement, and significantly increases the number of simulation results inside the error budget compared to the default strategy.

Hardware Limitations

Due to the hardware setup for controlling and monitoring the main spectrometer retardation voltage, the voltage step size is limited and it may not be realistically viable to chose the voltage steps as fine as the simulation results suggest as the best possible setting.
According to [A+18c], stability at the 3 ppm level is achieved, resulting in a minimal stable voltage step of 60 mV at 18.6 keV, considering the total measurement chain of the spectrometer's high voltage. Due to the coupling and common ground setting of the e-gun and the main spectrometer, this limit can be further improved and measurement with voltage steps of 40 mV can be performed. Nevertheless, this is just at the limit of stable high voltage operation in the spectrometer and thus may cause residual instabilities and uncertainties in the reconstruction of the same voltage set points for every column density.

5.3.5. Interpolation of the Zero Column Density Measurement

During the development of an optimized measurement strategy, another approach of minimizing the measurement time was found in the assumption that for vanishing column

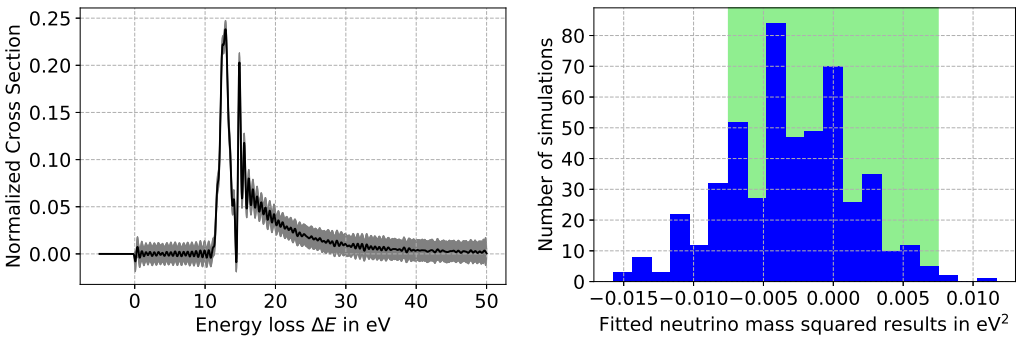

Figure 5.13.: Results for the Best Combination of Voltage Steps and Statistics: The deconvolution and ensemble test results for the best strategy to combine fine voltage steps and large statistics in every data point. With 4×10^6 electrons simulated every 40 mV, achieving the same total measurement time as for default setting. **Left:** 500 deconvolved energy loss functions, averaged with error band. **Right:** Ensemble test result from these 500 deconvolutions with a mean neutrino mass square shift of only $3.1 \times 10^{-3}\,\mathrm{eV}^2$ and a width of $4.5 \times 10^{-3}\,\mathrm{eV}^2$. The green area indicates the region inside the error budget. 83.4 % of the results are inside this green region.

density all electrons meeting the transmission condition of the main spectrometer will reach the detector, i.e. no effects like back-scattering off the detector wafer etc. occur, that would cause an energy dependent slope of the rate above the transmission edge[4]:

$$T(E > E_{\mathrm{spec}}) = 1. \tag{5.4}$$

With this assumption, an interpolation of the response function measurement at zero column density is justified, where the region between a surplus energy of 1.5 eV and the last simulated data point is not measured but interpolated. This yields a time saving of 22 %. As the experimental transmission function is not a perfect step function, but features a smearing from the energy distribution of the electrons and a finite spectrometer energy resolution, the interpolation is performed only between a surplus energy of 1.5 eV and the last simulated data point in the response spectrum. Using the same simulated data, once with interpolation and once without, the influence of the interpolation on the deconvolution is investigated. As it is shown in the left plot of Fig. 5.14, the deconvolution results of the interpolated and the fully simulated response functions do not differ more than the expected statistical fluctuations.
The right plot of Fig. 5.14 shows the ensemble test results of both deconvolutions. The two histograms show the same width of $11.9 \times 10^{-3}\,\mathrm{eV}^2$, and are shifted against each other by only $0.07 \times 10^{-3}\,\mathrm{eV}^2$, both yielding a mean value for the neutrino mass square shift of $17.0 \times 10^{-3}\,\mathrm{eV}^2$ and $17.1 \times 10^{-3}\,\mathrm{eV}^2$, respectively. The small difference in the neutrino mass square shift indicates that the response function with $\rho d = 0$ does not need to be measured exactly in every voltage set point but can be interpolated in between the transmission edge and a surplus energy set point at the far end of the spectrum. This interpolation yields up to 22 % less measurement time for the entire energy loss measurement, that can be distributed into larger statistics or finer voltage steps in the non-zero column density measurements.

5.4. Summary of Different Optimization Approaches

In a short summary, the most important results of this chapter are the following:

[4] This is only valid in first approximation, as the transmission edge and the electron energy distribution both have a certain finite width.

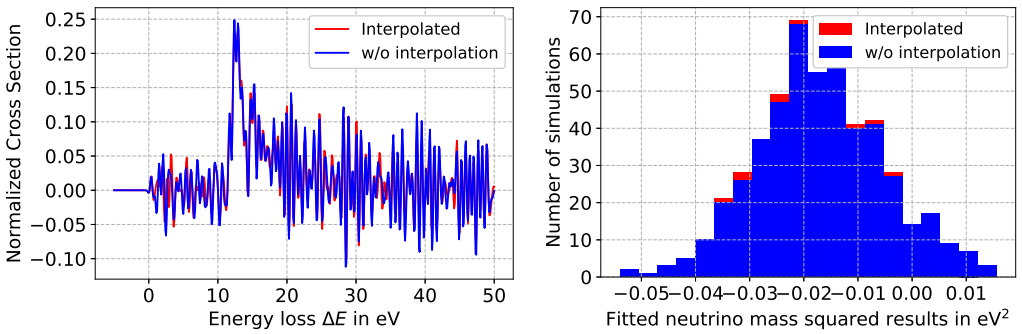

Figure 5.14.: Influence of Interpolation on the Deconvolution: Interpolating the response function measurement/simulation for zero column density has no significant influence on the deconvolution results and can thus be a valid means to reduce the overall measurement time. **Left:** The deconvolved energy loss function performing a simple interpolation of the data points between 1 and 50 eV surplus energy (red), compared with the deconvolution result without interpolation (blue), both with 10^6 electrons simulated for every voltage set point. **Right:** The results of the ensemble test performed with the two sets of response functions.

- Increasing the overall statistics by a factor of 10 can narrow the distribution of neutrino mass square shifts down to only $3 \times 10^{-3}\,\mathrm{eV}^2$ for 10^8 electrons in every voltage set point, but does not change the mean squared neutrino mass square shift.
- A redistribution of measurement time on different regions of the response functions for deconvolving the energy loss function does not yield any improvement of the neutrino mass square shift.
- Increasing the number of simulated data points and measuring with a smaller voltage step size while scanning the response functions leads to smaller neutrino mass square shifts.
  With simulations of 4×10^6 electrons in voltage steps of 40 meV a result of a neutrino mass square shift of $(3.0 \pm 4.5) \times 10^{-3}\,\mathrm{eV}^2$ was achieved. This is the best tested setting, with no significant improvement being possible without increasing the measurement time significantly.
- A detailed measurement of the response function for zero column density in the region between the transmission edge and the last voltage set point is not needed and can be interpolated in order to save 22 % of measurement time.

These results indicate that the deconvolution method from response function measurements may not be sufficient to determine the energy loss function of electrons in tritium gas to the desired accuracy level. This method nevertheless is applied during the STS-IIIa measurement campaign for commissioning, for testing and characterization reasons.
The following Ch. 6 describes the energy loss results gained from this measurement campaign.

Chapter 6

ENERGY LOSS MEASUREMENTS AND DECONVOLUTION AT THE STS-IIIA MEASUREMENT CAMPAIGN

In September and October of 2018, the source and transport section of KATRIN was commissioned with important characterization measurements performed during the so-called STS-IIIa measurement campaign. In this measurement period, also the first energy loss measurements in the KATRIN source were performed at different column densities of deuterium (D_2). These initial energy loss measurements offered the opportunity to further investigate the measurement strategy and to optimize the procedure. This chapter presents preliminary energy loss results and shows challenges and problems in the data taking that occurred during the measurements.
In Sec. 6.1 the NoiseEater system for the stabilization of the light intensity of the laser driven light source used for the e-gun illumination is presented. The experimental setup during the STS-IIIa campaign is described in Sec. 6.2 including the e-gun characterization, a new method for measuring response functions and simulations using the column densities as measured during STS-IIIa. The measured response functions are analyzed to deconvolve the energy loss function. The preliminary results of this analysis are presented in Sec. 6.3 with a description of the analysis strategy and the applied data corrections including light intensity, time synchronization and pile-up effects. A summary of the integral energy loss measurements during the STS-IIIa measurement campaign is given in Sec. 6.4.

6.1. Preparations for the Energy Loss Measurements During the STS-IIIa Measurement Campaign

During the preparations for the commissioning campaign, the optical system for the e-gun illumination (see Sec. 3.4.1) was optimized. One big problem was reaching the demanded intensity and the required long term stability of the electron rate, which is driven by the properties of the illumination. Therefore the properties of the illumination were investigated in a test setup outside the TLK without a connection to the entire KATRIN setup. The test setup is shown in Fig. A.3.

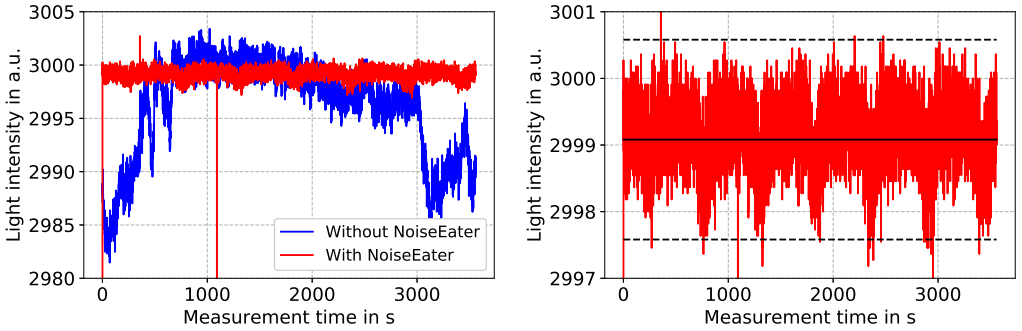

Figure 6.1.: Effect of the NoiseEater System: The results of the NoiseEater test measurement performed in preparation of the STS-IIIa measurements. Both plots show the same data set recorded using the LDLS as light source at 275 nm. **Left:** The light intensity using the NoiseEater system (red) is more stable especially in a long term observation, compared to the intensity without the NoiseEater (blue). **Right:** The data in a close-up view of the ±0.05 % region around the mean value. Using the LDLS as light source, the stability meets the Design Report requirements of 0.05 %, the solid black line shows the mean value of the measurement, the two dashed lines indicate the ±0.05 % range. The NoiseEater settings used for this graphs are given in Tab. A.2

Light Intensity Stabilization of the LDLS

The stability of the light intensity for the e-gun illumination exhibited large instabilities of over 1 %, as shown in the blue curve of the left plot in Fig. 6.1. This is above the required value of 0.05 % [KAT05], and thus needs considerable improvement. In order to achieve a better long-term stability, the so-called NoiseEater[1] has been installed and tested.
The principle of this NoiseEater is a PID (proportional–integral–derivative) controlled electrical loop. A PID controller is a feedback loop that compares a measured value (in the case of the NoiseEater a voltage corresponding to the light intensity) with a given set point. The proportional part sets the regulation intensity proportional to the difference between the measured value and the set point. Additionally, the long term deviation is worked against with the integral component of the PID controller by applying the corrections proportional to the integral of the deviation from the set value over a given time period. The derivative component aims to flatten the deviation to a constant value and thus is not suitable for reaching a certain value, but can be used for stabilization [ACL05]. The NoiseEater has two major components: the first component is a variable aperture system for the modulation of the light intensity (see Fig. A.2 in the appendix), the second component is a photodiode for monitoring the light intensity. This photodiode is connected to the regulation system which again controls the aperture. A desired signal voltage is set software-wise and the system regulates long term deviations from this set point within its working range.
To measure the effect of the NoiseEater, the beam is split into two paths with a 80/20 fiber splitter[2], with the major part being guided to the NoiseEater, and the minor part being monitored without the NoiseEater stabilization. This way, the influence of the NoiseEater on the stability of the UV light illumination can be demonstrated.
Figure 6.1 shows the measured diode signal with and without the NoiseEater. It shows a significant improvement of the short term stability, as well as the long term stability: fluctuations are reduced from about 1 % peak-to-peak to below 0.1 % peak-to-peak. As the right plot in Fig. 6.1 shows, the fluctuations of the signal are within the design report requirement of 0.05 % within 1 hour of measurement. The negative spikes, occurring

[1] Custom built by *TEM Messtechnik*, `http://www.tem-messtechnik.de/noiseeater.htm` accessed on April 3rd, 2019.
[2] Produced by FONT Canada, `https://fontcanada.com/`.

periodically due to the PID settings (see Tab. A.2) in the NoiseEater corrected signal do not affect the deconvolution result significantly, as they are still below the limit of 0.05 %. Following these results, using the NoiseEater system is a suitable method to stabilize the light intensity of the e-gun illumination with the LDLS and thus also the electron rate emitted from the e-gun.

6.2. The STS-IIIa Measurement Setup

During the commissioning of the e-gun at the beginning of STS-IIIa (see Sec. 6.2.1) it was found out, that not all parameters fulfill the design report requirements. Instead of the expected electron rate of about 50 kcps, which already was achieved during test measurements [Sac18], with the LDLS at 250 nm only a rate of 2.1 kcps was achieved. The reason for this dramatic drop is probably a change in the mounting of the e-gun fibers when the system was moved to its position at TLK. Also a drift of 0.2 $\frac{\%}{\mathrm{h}}$ towards lower rates was detected, which is not correlated to the light intensity and cannot be explained at the moment.
In order to achieve higher rates again, the pulsed UV laser was used as light source instead of the LDLS, reaching much higher rates of about 10 kcps. The stability of only about 10 % within 12 h of the pulsed laser is not sufficient for the measurement of response functions at four different column densities [BDL$^+$19]. As the stability of the used laser as light source is not as good as required for the initially planned measurement procedure, the process of scanning the surplus energy spectrum needs to be accelerated. Therefore a new scanning method was developed which is less prone to long-term fluctuations. By a fast scanning of the spectrum in up and down direction the long term fluctuations affect every part of the spectrum in the same manner and therefore do not distort the spectral shape. This fast scanning needs to be done by ramping the e-gun energy up and down, as the spectrometer takes 20 s to 30 s for setting the exact retardation voltage whereas the e-gun energy is ramped continuously. Each of these individual scans takes only 30 min and is performed repeatedly for every column density in up and down direction, as described in more detail in Sec. 6.2.2.
In addition to the problems with the e-gun and the changed strategy, the column densities achieved in the laboratory were not exactly the same as the ones assumed in the simulations. With 5 %, 36 % and 87 % instead of 20 %, 60 % and 100 % of the nominal column density of $\rho d = 5 \times 10^{17}\ \frac{1}{\mathrm{cm}^2}$ [Mar18] all column densities were below the originally planned values. Due to the different column densities, especially because of the lowest column density with only 5 % instead of 20 % of the nominal column density, the deconvolution result is more prone to statistical fluctuations in the measured response functions compared to the design values (see Sec. 6.2.3).

6.2.1. Characterization of the Rear Section E-Gun

The goal of the first phase of STS-IIIa was to obtain the real e-gun characteristics as built in order to implement these parameters into the simulation model. In this characterization, two properties are of high importance. The first is the electron rate, to set the total number of simulated electrons, the second is the energy distribution.
During the STS-IIIa measurement period the e-gun did not perform as expected. The electron rate using the LDLS at a wavelength of 250 nm was about 2.1 kcps [BDL$^+$19], which is significantly lower compared to the minimal needed value of about 20 kcps [Bab14]. The low rate of 2.1 kcps would correspond to an increase of measurement time of a factor of 25 compared to 50 kcps in order to achieve reasonably high statistics and cannot be compensated by the measurement time optimizations investigated in Ch. 5. In order to keep the measurement time at a realistic level, a pulsed UV laser is used as light source,

providing an electron rate of up to several 100 kcps. For the measurements, rates of 9 kcps to 12 kcps were chosen, which is sufficient for the STS-IIIa commissioning measurements. This higher rate was achieved at the expense of long-term stability. The electron rate was determined to be drifting nearly 10 % within 12 h. Also the fluctuations of about ±1 % peak-to-peak recorded with the pulsed UV laser as light source are too high for the precision measurements of the response functions required for the energy loss deconvolution.
Due to the fact that the UV laser is a pulsed light source and not a continuous light source as the LDLS, the NoiseEater can not be used to improve the stability as tested in advance (see Sec. 6.1). The reason for not being able to stabilize the UV laser with the NoiseEater is that the amplifier can only have a much smaller amplification to not be in the overload region. Having only an average voltage of about 100 mV provided from the amplifier, the 0.05 % range results in 5×10^{-5} V which is below the resolution of the 16 bit ADC of the NoiseEater. Therefore the NoiseEater did not improve the stability of the electron rate produced with the pulsed laser [BDL$^+$19]. To be able to measure response functions anyway, the fast-scanning mode was developed, and is described in Sec. 6.2.2.
The remaining drift and fluctuation in the intensity can be corrected by monitoring the light intensity with a photodiode. As a clear correlation between the diode signal and the detected electron flux is visible, the diode signal is used to normalize the individual data points in the analysis of the response functions to the light intensity and thus makes the measurement independent of light intensity fluctuations.
During the commissioning measurements, the energy width of the e-gun was determined by investigating the transmission edge with an empty WGTS. From the width of the transmission edge the energy spread of the e-gun was derived to $\sigma = 0.128$ eV at 250 nm [BDL$^+$19] using the LDLS as light source. This result is slightly better than the value of 0.2 eV that is assumed in the simulations, therefore it is sufficient for satisfactory results in the further measurements. A similar result of 0.11 eV was measured using the UV laser instead of the LDLS. This result indicates that further measurements with the UV laser are possible in terms of the electron energy spread. The problem of long and short term stability still needs to be handled; therefore a new method of scanning is introduced, as described in Sec. 6.2.2.

6.2.2. Fast Scanning Mode: A New Method for Response Function Measurement

The original measurement strategy was to keep the electron energy constant, while scanning the surplus energy spectrum by ramping the main spectrometer voltage in given discrete steps. This scanning was planned to be done by one single long scan of the retardation voltage for every column density value.
The demanded rate stability is not given while using the UV laser as light source. These instabilities, especially the observed long-term drifting behavior, have strong negative effects on the measured response function, since they distort the response function shape and therefore affect the deconvolution results. In order to eliminate these effects, a new method for the measurement of the response functions was introduced during STS-IIIa. The so-called fast-scanning mode is described and explained in this section with its advantages and disadvantages.
With the long term drifting behavior of the electron rate, the problem occurs that voltage set points at the upper end of the surplus energy spectrum (to be measured 2-3 days later) have a different number of initially emitted electrons than voltage set points in the lower range, which obviously would deform the response functions. Therefore, a faster scanning is desired, to reduce the distortion of the response function. These shorter runs are then repeated multiple times. To limit the impact of long-term drifts, the scanning direction is alternated, i.e. the response functions are repeatedly scanned up and down and the counts

of alternating scan directions will be added.
The main spectrometer takes ≈20 s to 30 s to set a stable voltage value in the desired voltage steps resulting in 30 min of measurement time for one scan from −5 V to 55 V, therefore fast scanning is not possible using the main spectrometer. This is the reason why the measurement principle was changed: Instead of keeping the electron energy constant and scanning with the main spectrometer, the energy of the electrons is changed and the spectrometer potential is kept fixed, since the acceleration voltage of the e-gun can be changed continuously. This has the benefit, that no measurement time is required to set the correct surplus energy values. During the STS-IIIa measurements, the e-gun starting potential is scanned with a speed of 33 $\frac{\text{mV}}{\text{s}}$. During data analysis, an additional linear fit has to be performed in order to determine the surplus energy value from the recorded measurement time.
The advantages of the fast scanning mode are summarized:

- **Continuous scanning** of the spectrum in fast scanning mode gives the possibility of choosing the data binning as desired. By the ramping, the analysis is not fixed to the discrete voltage steps as it is the case in the planned spectrometer measurements. Also the binning can be chosen even finer than the smallest possible voltage steps of the main spectrometer and its hardware limits.
- **Time saving** due to continuous scanning, and no extra time needed for setting the retardation voltage. This way, an overall of 20 h can be saved, in comparison to the originally proposed strategy.
- **Long-term drift** of the electron rate has lower impact on the measurement results by scanning the response functions repeatedly in up and down direction.
- **Short-term fluctuations** also do not worsen the results, as the measurement is performed multiple times, yielding a good overall average and thus compensating errors in single measurements by short term variations of the electron flux.
- **Online monitoring** is greatly facilitated by having a complete response spectrum available after 30 min of measurement. This allows to check the measured response functions on the run and saves time if any adjustments are required. Additionally, hardware failures that could corrupt measurements do not affect multiple days of measurement but only a short 30 min run which then can be repeated.

Although the mentioned advantages do support the fast scanning mode, there are also some disadvantages to be mentioned in this context:

- **The total cross section** for electrons scattering off molecules is slightly depending on the energy of the incoming particles as discussed in [Tro18]. Therefore, increasing the electron energy may also slightly distort the response function due to the energy dependent scattering probability. This effect can be calculated to a difference of roughly 0.5 %.
- **Measurement time distributions** as described in Ch. 5 cannot be applied, as no individual surplus voltage values are set in the measurement, but the electron energy is scanned continuously.
- **Further analysis steps** are needed, as the data of every scan first needs to be binned and later the different runs are stacked into one single response function for higher statistics.

Nevertheless, the advantages out weigh the disadvantages of the fast scanning and it was found to be working well for the STS-IIIa measurements (see Sec. 6.3). More importantly, it was the only way to measure response functions at different column densities, due to the above mentioned problems with the e-gun characteristics.

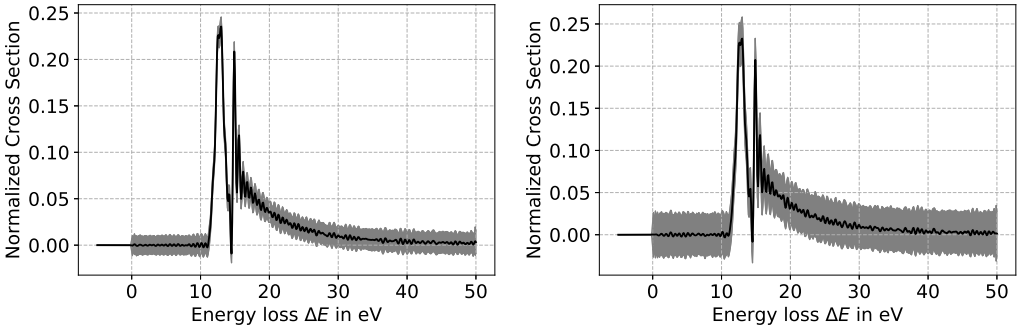

Figure 6.2.: Comparison of deconvolutions from simulations at the originally planned column densities and the column densities actually used during STS-IIIa. **Left:** The deconvolution of simulated response functions with original column densities of 0 %, 20 %, 60 % and 100 % of the nominal column density. **Right:** Deconvolution of simulated response functions with 0 %, 5 %, 36 % and 87 % of the nominal column density, as measured in STS-IIIa. The right plot shows a stronger statistical fluctuation in the deconvolutions with the measured column densities.

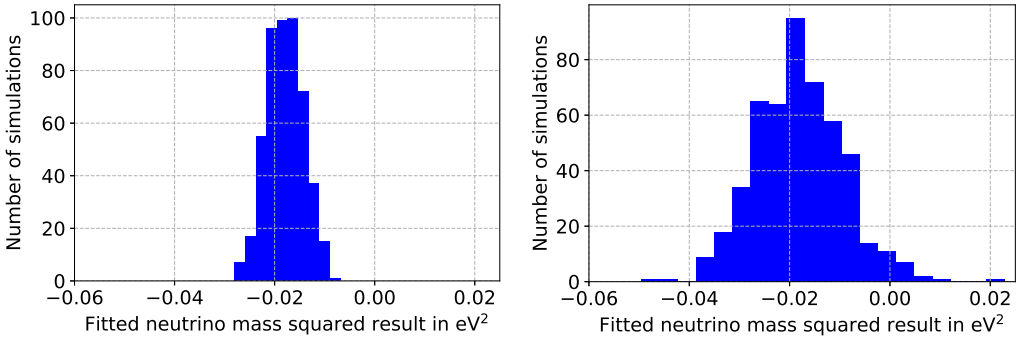

Figure 6.3.: Comparison of the ensemble test results for the two different column density settings with 500 simulations each. **Left:** The originally planned column density values, **Right:** the column density values used during STS-IIIa. The distribution in the STS-IIIa case is much broader due to the higher fluctuations in the energy loss functions from the changed column densities.

6.2.3. Simulations with STS-IIIa Settings

During the STS-IIIa measurements, the column densities were 0 %, 5 %, 36 % and 87 % of the nominal column density and thus below the levels as the simulated default values from the KEloss simulations. The effect of this discrepancy on the resulting energy loss deconvolution is investigated in the following. Therefore, simulations with the actual STS-IIIa column densities are performed and an energy loss function is deconvolved from those simulated response functions with 10^7 electrons in every voltage set point.
As shown in Fig. 6.2, the differing column densities have a negative influence on the stability of the deconvolution. For the same number of simulated sets of response functions, the deconvolution in the case of the measured STS-IIIa column densities shows a visibly larger fluctuation around the central value than for the designed ρd values.
This can be explained with the low $\rho_1 d$ of only 5 % of the nominal column density. This leads to a very small distinction between the response function with empty source and for the lowest non-zero column density, since only 9 % of the particles undergo scattering. This leads to strong fluctuations and high statistical noise in the single scattering function ϵ_1, which is used for the deconvolution process. This larger fluctuation in the deconvolution results in a broader distribution of neutrino mass square shifts after performing the ensemble test with both column density settings, as Fig. 6.3 illustrates. The Gaussian fit results give

sigma widths of

$$\sigma(\Delta m^2) = 3.6 \times 10^{-3}\,\mathrm{eV}^2 \text{ and } 8.8 \times 10^{-3}\,\mathrm{eV}^2$$

for the default values and STS-IIIa measured column densities, respectively. As the average of the energy loss functions for both deconvolutions are very similar, the mean values of the two mass shift distributions only differ by 0.5 %, being $-17.9 \times 10^{-3}\,\mathrm{eV}^2$ and $-18.0 \times 10^{-3}\,\mathrm{eV}^2$. A column density setting corresponding to the default values is therefore recommended to achieve a narrow distribution of neutrino mass square shifts.
Furthermore, simulations were performed after the e-gun commissioning with known total numbers of electrons for every simulated voltage step, the measured energy spread of the e-gun of 0.11 eV and the actual column densities. These simulations are performed to determine the best results for the given setup without any systematic effects. After finishing again 500 simulations and deconvolutions, an ensemble test is performed, to check how good the deconvolution matches the energy loss model. This ensemble test yielded a result of

$$\Delta m_\nu^2 = (97 \pm 116) \times 10^{-3}\,\mathrm{eV}^2$$

with only 9.2 % of the results being inside the error budget. The large uncertainty can be explained with the measured low column densities, as well as with the lower statistics compared to the default settings of 10^7 electrons in every voltage step.
With the given properties of the column density and electron rate, this is the best possible result with no additional systematic effects.

6.3. Preliminary Results from Energy Loss Measurement Using the Deconvolution Method

This section shows the results of deconvolving the energy loss functions from measured response functions during STS-IIIa. First, in Sec. 6.3.1, the analysis chain is described, as the measurement procedure has to be changed compared to the initially planned method. The analysis of the data followed by a deconvolution of the energy loss function is discussed in Sec. 6.3.2. The systematics and challenges occurring in the analysis process are investigated and discussed in Sec. 6.3.3 in order to improve the deconvolution result. The deconvolution result including the data corrections is discussed in Sec. 6.3.4.

6.3.1. Analysis Strategy and Deconvolution Process

Due to the fact that the measurement strategy was changed from scanning with the main spectrometer to fast scanning mode with the e-gun energy, some parts of the deconvolution process and analysis chain had to be adapted to this change in order to use KEloss for the deconvolution of the energy loss function. The two analysis steps that needed to be added are binning of the continuous ramps and the stacking of the short scans. This additional analysis framework is implemented in the EgunTools[3] software package as part of KASPER, developed by the authors of [BDL+19].

Binning

The first step that needs to be performed in order to deconvolve the energy loss function from measured data is the binning of the recorded voltage and count rate in the ramping processes. These ramps need to be known to be able to generate data which combines the count rate at the FPD recorded in time with the energy of the e-gun electrons and thus the surplus energy. This synchronization between timestamp and surplus energy is done in individual runs, where each run is alternately an up or down scan (indicating an increasing or decreasing sequence of the electrons' surplus energy). In this step, the choice of the

[3]Internal KATRIN access: `https://nuserv.uni-muenster.de:8443/katrin-git/EgunTools`

Table 6.1.: Numbers of Runs During STS-IIIa: This table shows how many runs at a given electron rate were measured during the STS-IIIa campaign for each column density. The last column shows the according overall number of electrons assuming voltage steps of 100 mV as used in the default settings.

Column Density	Number of Runs	Electron Rate	Electrons for 0.1 V Steps
0 %	27	12 kcps	1.0×10^6
5 %	98	6 kcps	1.7×10^6
36 %	76	12 kcps	2.7×10^6
87 %	88	12 kcps	3.2×10^6

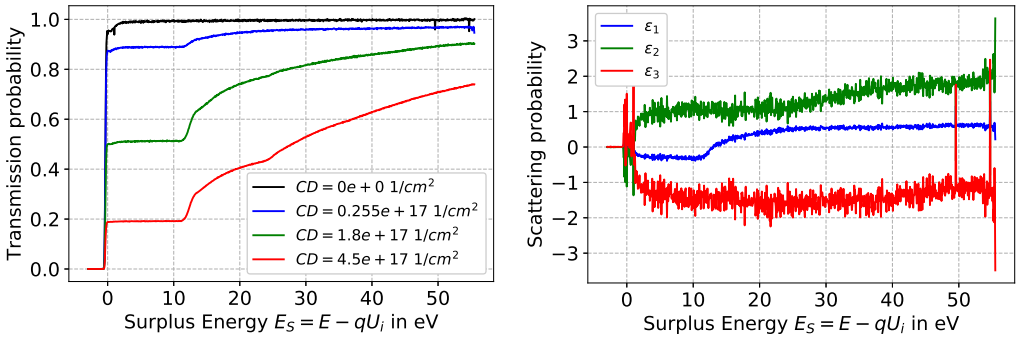

Figure 6.4.: Raw Data Response and Scattering Functions: Binning the continuous ramps into 60 mV bins. **Left:** The response functions measured during the STS-IIIa campaign. It is clearly visible that some systematic effects occur, and cause the transmission edge to be cut in the upper end of the $\rho d = 0$ curve. This effect is considered to be due to detector pile-up. **Right:** The scattering functions after the matrix inversion of response functions on the left. The scattering functions are not only very noisy, but also ϵ_2 is larger than 1, and ϵ_3 is negative, which indicates strong systematics in the data.

performed binning defines the voltage steps in the further analysis from the continuously ramped energy. This binning of course also affects the number of measured electrons for every surplus energy bin, yielding higher statistical noise for finer binning and vice versa.

Stacking

With this binning performed for every fast up and down scan, the data needs to be stacked in order to achieve the highest possible overall statistics, comparable to one single scan of the entire spectrum.
After stacking the measured and binned data and thus generating the response functions for the given experimental conditions, the deconvolution is performed. As first step, before executing the SVD deconvolution, the data from the STS-IIIa measurement needs to be processed to the structure of KEloss.
This step needs to be performed for every column density individually. Because data is recorded at different column densities with a different number of runs (see Tab. 6.1), these discrepancies have to be corrected.

6.3.2. First Analysis and Deconvolution Without Data Corrections

Performing the binning with bins of 60 mV, corresponding to 10^5 to 10^6 electrons in each bin[4], yields the response and scattering functions shown in Fig. 6.4.
The response functions in the left plot show a significant lack of counts on the upper end

[4]Different number of runs for different column densities yield different maximum overall statistics, see Tab. 6.1.

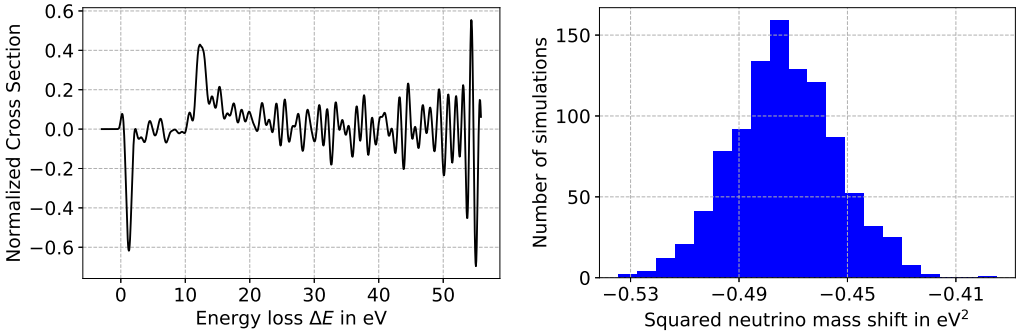

Figure 6.5.: First Deconvolution of Raw Data from the STS-IIIa measurement: **Left:** the deconvolution from the STS-IIIa response functions. The deconvolution is performed from data shown in Fig. 6.4. **Right:** The results of the ensemble test of 500 tritium spectrum simulations for the deconvolution result shown in the left plot. No data corrections such as pile-up effects were introduced into the data.

of the transmission edge. This effect can be clearly seen in the transmission with zero column density, and gets smaller for higher column densities, pointing towards this effect being dependent of the detector count rate. This lack of counts can be explained by pile-up effects. Because of the focusing of electron emission into 18 ns short pulses, the chance of two or more electrons arriving at the detector within its time resolution is much higher compared to a continuous wave (CW) light source with the same rate. The pile-up effects are enhanced in the region of the transmission edge, as the electrons with close to zero surplus energy are very slow in the analysis plane of the spectrometer. This yields many electrons with a slightly higher energy (inside the e-gun's energy spread) to catch up with the slower electrons and thus arrive at the detector in a very short time (smaller than the time resolution). This missing count rate is also visible in the 5 % and 36 % column density measurements to a lesser degree.
In the right-hand plot of Fig. 6.4 the extracted scattering functions from the measured data are shown. Here the influence of systematic effects is very dramatic, as the scattering functions extracted from the data are significantly above 1 (ϵ_2) and significantly below 0 (ϵ_3), which of course are not physical values. The systematic effects leading to these results are investigated in Sec. 6.3.3.
Using the single scattering function in Fig. 6.4 as input, the deconvolution of the energy loss function yields the result shown in Fig. 6.5. As shown in the left plot, the peak of the energy loss function is clearly visible, but only a rough shape of the energy loss function can be reconstructed. In the region of the ionization tail (at $\Delta E > 16\,\mathrm{eV}$), the deconvolution result starts to strongly oscillate, and significant noise occurs. Also, a strong negative peak in the region of the transmission edge ($\Delta E \approx 0$) is visible, which points out, that the recorded data is affected by pile-up effects.
Using the deconvolved energy loss function in an ensemble test comparing it to the Glück model leads to a very large neutrino mass square shift, shown in the right plot of Fig. 6.5 of

$$\Delta m^2 = (-473 \pm 19) \times 10^{-3}\,\mathrm{eV}^2. \tag{6.1}$$

This value is far away from the requirements for the KATRIN experiment of $\pm 7.5 \times 10^{-3}\,\mathrm{eV}^2$. In this step of analysis, it is still assumed, that the Glück model describes the energy loss of electrons in deuterium best. Nevertheless, the ensemble test is only sensitive to differences between the input model in the Monte Carlo simulation and the deconvolution result. By comparing these two models, a precise statement about the quality of the deconvolution is only valid under this assumption.
By investigating systematic effects during the measurements, the measured response functions can be corrected with respect to systematic effects, as described in the following.

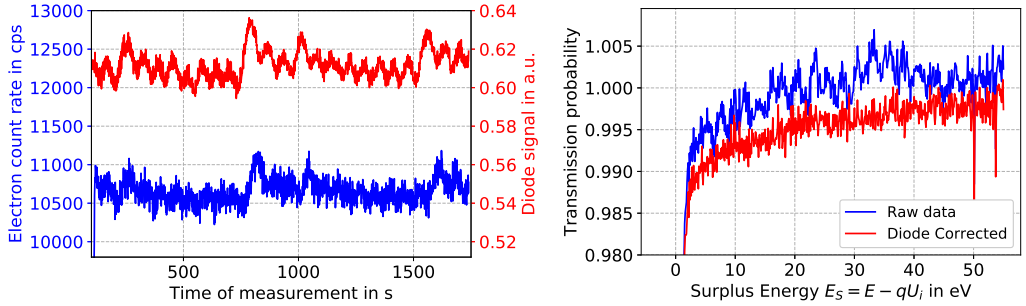

Figure 6.6.: Diode Signal Correlation to Electron Rate: By monitoring the light intensity, the rate of emitted electrons is corrected. **Left:** The plot shows a clear correlation between the electron rate measured in full transmission at the FPD (blue) and the light intensity monitored by a photodiode (red). **Right:** Comparing the response function with zero column density with (red) and without (blue) diode signal correction shows less fluctuations in the FPD signal (run # 43411) after applying the light intensity normalization.

6.3.3. Data Post-Processing and Correction to Systematic Effects

As mentioned in the previous section, various systematic effects are present which yield a worse deconvolution result, compared to the optimal results as gained from the simulations described in Sec. 6.2.3. Investigating these systematic effects and correcting for them is therefore crucial in order to improve the deconvolution result, and therefore is of high importance in the analysis procedure. The most important effects are the laser intensity fluctuation, detector pile-up and the time synchronization between the voltage supply readout at the e-gun and the FPD. These effects are discussed in this section.

Light Intensity Normalization

For monitoring the light intensity, the light beam is split up into two parts with a 80/20 fiber splitter, where the major part is directly fed onto the e-gun photocathode, and the minor part is connected to a photodiode. By comparing the electron rate in full transmission with the photodiode signal, a clear correlation is found, as shown in the left plot of Fig. 6.6. Normalizing the electron count rate with the diode signal thus allows to correct the systematic effect of light intensity fluctuations as well as long-term drift behavior to a large extend, as shown in Fig. 6.6.
With the diode signal correction, the rate is more stable (statistic fluctuations of below 0.5 %) and does not show the short term fluctuations of up to 1 % in 5 min arising from the light intensity instabilities, see right plot in Fig. 6.6. The blue curve shows the response function for zero column density above the transmission edge, stacked from all up and down scans. It is clearly visible, that the uncorrected data suffers from light intensity fluctuations and instabilities, showing large spikes in the response curves, which disappear almost completely when the light intensity normalization is applied.

Time Synchronization

Having multiple data acquisition instances spread along several buildings requires a good time synchronization. This synchronization is usually provided by using a time server. Due to the preliminary working setup in the data acquisition system of the rear section being still under construction, a time shift between the time stamps of the count rate taken at the detector and the voltage measured at the e-gun occurred. This faulty synchronization causes problems, especially in the fast scanning method described in Sec. 6.2.2, as a shift of the times for the rear section and the FPD in a constant direction causes opposite shifts for

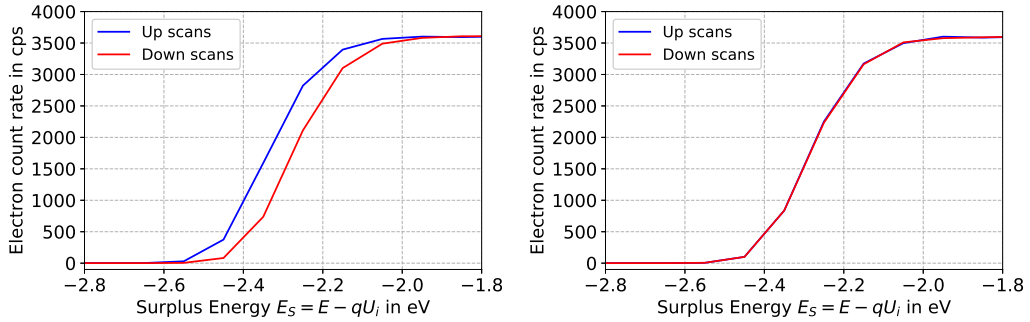

Figure 6.7.: Time Synchronization in STS-IIIa Data: This graphic shows the transmission edge in the performed scans at 87 % column density with increasing (blue) and decreasing (red) surplus energy. **Left:** the unsynchronized data shows a shift of about 60 meV between the up and down scans. **Right:** With corrected time synchronization, no shift is visible.

the surplus energy in the binning process for up and down scans, and therefore effectively doubles the energy smearing. This problem is graphically described in Fig. A.4.
Without correcting for the time shift, the up and down scans have a significant shift of about 50 mV (left plot in Fig. 6.7). The binning used for this analysis is 60 mV, the time synchronization thus yields voltage shift in the order of one voltage bin. With the data being stacked this way, it causes a smearing of the transmission edge and of the features of the energy loss function which are included in the analysis in Sec. 6.3.2. By shifting the time stamps of the voltmeter data used to monitor the electrons' starting energy, the position of the transmission edge can be adjusted to match the position of the other scans, as shown in Fig. 6.7.
Time synchronization of the individual runs thus yields a better energy resolution for the further analysis steps.
These synchronization problems also occur between the individual up scans as well as in the down scans. All of this is considered in the analysis, whereas, for the sake of clarity of the description, only the difference between the stacked up and down scans is shown here.

Pile-Up Correction

The last significant systematic effect that can be corrected in order to improve the deconvolution of the data is the detector pile-up. If the electron rate gets too high, multiple electrons arrive within the time resolution of the detector. The pile-up will lead to recording a lower rate than the actual one. These effects are responsible for the strong deformation of the response function just above the transmission edge (see Fig. 6.4). A dedicated pile-up correction for the pulsed laser was developed by S. Enomoto (University of Washington) which enabled to resolve pile-up events and reconstruct the actual rate. The details of the pile-up correction are not described in detail here.
The effect of the pile-up correction is shown in Fig. 6.8. As can be seen in these two plots, the effect is much stronger with high electron rates (left plot) than with lower electron rates (right plot) as expected. The left plot in Fig. 6.8 shows that the correction still is not perfect, and causes a slight overestimation of the rate close to the transmission edge and therefore needs to be further improved. But since the absolute difference to the expected plateau with a transmission probability of 1 is in the permille range and therefore much smaller compared to the uncorrected data, the pile-up correction is applied for the following analysis.

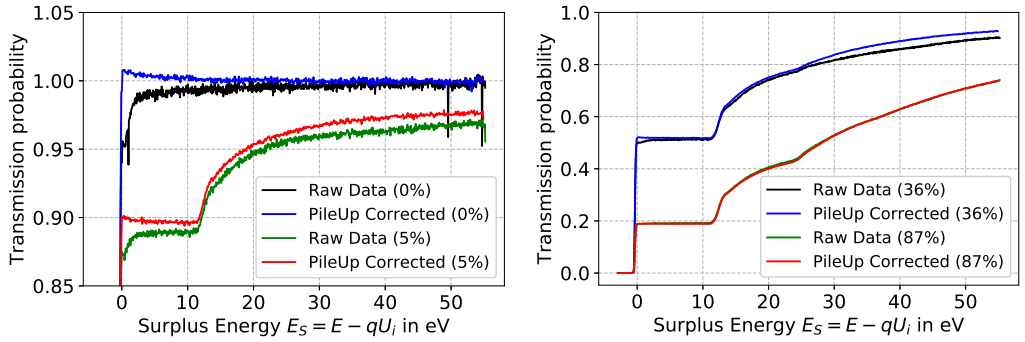

Figure 6.8.: Influence of Pile-Up Correction: These plots show the influence of detector pile-up on the response functions. **Left:** The raw data and the pile-up corrected data for the two lower column densities (0 % and 5 % of nominal column density). **Right:** The raw data and the pile-up corrected data for the two higher column densities (36 % and 87 % of nominal column density). As shown in the left plot, the influence of detector pile-up is very strong in regions with high count rates. With lower count rates due to high column density the pile-up effect decreases (right plot).

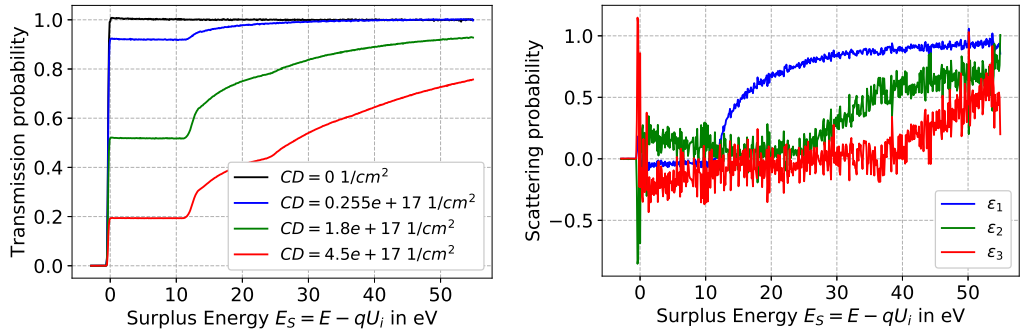

Figure 6.9.: Corrected STS-IIIa Data: Improved response and scattering functions after applying light intensity normalization, time synchronization and pile-up correction to the STS-IIIa data. **Left:** Response functions after applying the corrections. **Right:** The scattering functions extracted from the corrected response functions.

6.3.4. Deconvolution of Processed Data

After applying the time synchronization, light intensity normalization and pile-up correction, another analysis is performed. The corrected response functions are shown in the left plot of Fig. 6.9. Compared to the raw data in Fig. 6.4, the response functions are less noisy and the missing corner close to the transmission edge is mostly recovered. The response function for 5 % column density now reaches full transmission and approaches the curve of the zero column density measurement at about 30 eV surplus energy. This is a clear improvement compared to the uncorrected data, where the 5 % column density curve does not reach 1 within the measurement range unlike the expectations and simulations.
The improvement of the data processing is even more visible when looking at the scattering functions gained from matrix inversion, see right plot in Fig. 6.9. The single scattering function ϵ_1 (blue) looks very similar to the simulated curves (see again Fig. 4.2). Despite the noise, the shape of the single scattering function obtained from simulations is very well visible and the curve does not drop significantly below 0 (as it does in the raw data in Fig. 6.4), and reaches 1 towards the end with no further increase. The double and triple scattering functions $\epsilon_{2,3}$ also look as expected from the simulations. The double scattering function starts to rise just above 20 eV, as predicted from the energy loss model. The main problem with the scattering functions is the still not perfect pile-up correction which is visible in the multiple scattering functions in the region from 0 eV to 10 eV. The functions

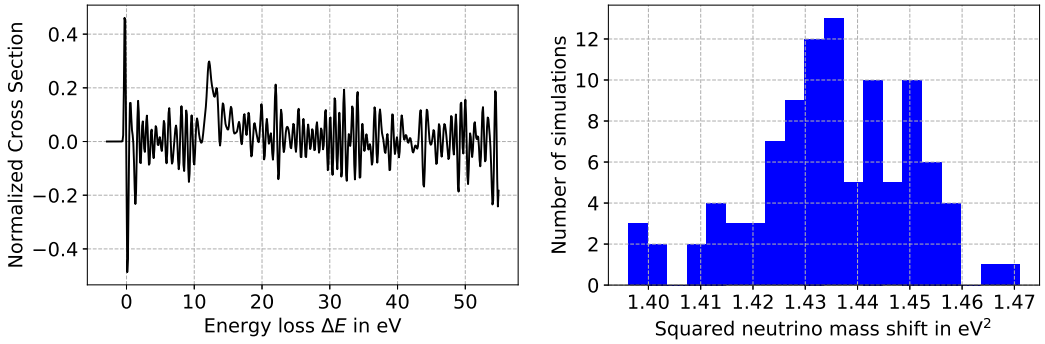

Figure 6.10.: Deconvolution with Data Corrections: The measured electron rate can be corrected as described in 6.3.3. **Left:** The resulting energy loss function from the deconvolution of the corrected response and scattering functions. **Right:** The ensemble test result from this deconvolution. The neutrino mass square shift of over $1.43\,\mathrm{eV}^2$ is a factor of 200 above the allowed error budget.

should be zero here but they are not exactly vanishing, but slightly above (ϵ_2) and below (ϵ_3), which can be explained by the overestimation of the pile-up corrected rate as discussed in Sec. 6.3.3.

After applying the corrections to the data, the single scattering function is deconvolved to generate the energy loss function, and further again an ensemble test is performed. The results are shown in Fig. 6.10.

As can be seen in the left plot of Fig. 6.10, the strong negative peak occurring in the deconvolution of the raw data (see Fig. 6.5) is smaller and the strong increase of numerical noise towards the upper end of the spectrum is decreased. The excitation peak is clearly visible, and significantly above the noise level.

Although the deconvolved energy loss function shows less numerical artifacts compared to the raw data deconvolution, the result of the ensemble test is not improved compared to the result in Eq. (6.1). After the Monte Carlo simulation and neutrino mass square fit, a shift of the neutrino mass square with a mean of

$$\Delta m^2 = (1.43 \pm 0.02)\,\mathrm{eV}^2 \tag{6.2}$$

is found. The standard deviation of $0.015\,\mathrm{eV}^2$ results from the statistics underlying the Monte Carlo simulation performed in the ensemble test. This result is a factor of 200 higher than the error budget of $7.5 \times 10^{-3}\,\mathrm{eV}^2$, which is unacceptable for the neutrino mass square analysis of KATRIN.

Investigating this discrepancy between data corrected with respect to systematic effects and worse results yields a few possible explanations.

The easiest explanation approach, is the possibility that due to statistical fluctuations in the measurement, the measured response functions are just a set of data that yields a result far at the end of the simulated neutrino mass square shift distribution. With simulated response functions using voltage steps of 60 mV and 1.5×10^5 electrons in every voltage step, according to the settings used for the analysis of the corrected response functions, the neutrino mass square shift of $(97 \pm 116) \times 10^{-3}\,\mathrm{eV}^2$ is achieved. Also, 1 % of the ensemble test results are outside of $\pm 1\,\mathrm{eV}^2$, showing that a result as high as $1.43\,\mathrm{eV}^2$ is unlikely, but still possible.

The second possible explanation, why the corrected data might generate worse results than the raw data influenced by systematic errors, can be found in the ensemble test procedure. This test only checks the agreement between the input energy loss model in the Monte Carlo simulation and the deconvolved energy loss function from the response functions. Assuming, the Glück model used for the Monte Carlo simulations has some

slight uncertainties and errors, leads to the effect of a deconvolution from the raw data being in fact worse compared to the real energy loss processes in the WGTS but closer to the model than the corrected data being closer to the real energy loss processes. The ensemble test results are therefore inconclusive for reviewing the measurement and only used to support the simulation results which show, that the results of the integral energy loss measurement based on the deconvolution technique used in the work at hand are not sufficient for the high demands of KATRIN.

6.4. Conclusions and Outlook from the STS-IIIa Measurement Campaign

After testing the deconvolution method during the STS-IIIa measurement campaign, there are a few important conclusions that need to be pointed out with regard to future energy loss measurements:

- **Fast-scanning mode** can be applied to measure the required response functions and has some significant advantages compared to the originally planned spectrometer scanning method (see Sec. 6.2.2).
- **The Glück model** may still have problems that need to be further investigated in order to use this model, e.g. for ensemble testing measured energy loss functions in the neutrino mass measurements.
- **Ensemble testing** should be replaced or at least complemented by a more suitable assessment method to incorporate systematic uncertainties on the neutrino-mass inference from the β-spectrum.
- **The deconvolution method is working**, but the fundamental difficulty of this principle is the demanded high statistics and the needed small voltage steps for good results. With too low statistics the results are far beyond the expectations and KATRIN requirements.
- **Column density settings** of the WGTS are very important and should be kept at the design report values of 0 %, 20 %, 60 % and 100 % of the nominal column density (see Sec. 6.2.3), to provide the best insight into the scattering induced energy loss.
- **Correction of systematic effects**, such as time synchronization, light intensity monitoring and pile-up corrections, have been implemented into the analysis and improved the measurement results (see Sec. 6.3.3).
- **Time of flight** has been tested as an alternative method for the measurement of the energy loss function and yielded very promising initial results, which appear to fully satisfy the KATRIN requirements of energy loss determination.

Although the result of the response function measurements and deconvolving the energy loss function did not meet the expectations, the data taken for the integral energy loss measurement can be used for other approaches like fitting a model to the data and extracting the energy loss model from the fitting results (see [Sch]). Also a new method, the so-called 'Time of Flight energy loss' was tested, which enables to provide a differential energy loss spectrum by investigating the time of flight of electrons undergoing scattering in the source (see [Sac, Rod]). The results from both, Time of Flight and model fitting, are very promising and are currently being investigated further.

Chapter 7

CONCLUSION AND OUTLOOK ON FUTURE ENERGY LOSS MEASUREMENTS

The KATRIN experiment aims to measure the effective mass of the electron antineutrino with a sensitivity of 200 meV (90% CL.). This can be achieved by a precision measurement of the energy of electrons produced in the β-decay of tritium. To be able to perform a measurement of this precision, it is necessary to characterize the systematic effects and uncertainties occurring in the 70 m long experimental setup. One of the key systematic effects in KATRIN is the energy loss of the emitted electrons due to inelastic scattering off the source gas molecules within the 10 m long source beam tube. To measure the energy loss function with the KATRIN setup, a method of deconvolving the energy loss function from measurements of response functions with a dedicated monoenergetic electron source at different column densities was developed by Hannen et al. After the very promising results presented in [HHW$^+$17], the deconvolution method was further investigated in [Tro18], where it was shown, that the deconvolution results do not meet the error budget requirements of a neutrino mass square shift of smaller than $7.5 \times 10^{-3}\,\mathrm{eV}^2$. As m_ν^2 is one of the fit parameters of the KATRIN measurement, this quantity should not be shifted due to systematic effects if a high sensitivity to the effective mass of the electron antineutrino is demanded. Thus this method of deconvolving the energy loss function needs to be further improved. In this thesis the response function measurements are optimized for the deconvolution process in simulations and tested with data recorded during the STS-IIIa measurement campaign (end of 2018).
With a simulation result of

$$\Delta m_\nu^2 = (-17.9 \pm 3.7) \times 10^{-3}\,\mathrm{eV}^2$$

for the default settings, proposed in [KAT05] and [HHW$^+$17], the mass shift is by a factor of 2.5 too large compared to the requirements, with only 0.2 % of the performed simulations yielding a result inside the error budget. The approach clearly needs to be optimized in order to achieve the demanded neutrino mass sensitivity.
The influence of the overall number of electrons in the response function measurement was investigated on the basis of simulated response functions. This research with the according deconvolution and ensemble test process described in Ch. 5 showed no influence on the mean value of the distribution of neutrino mass shifts. With higher statistics the distribution only got narrower with an unchanged mean value, yielding

$$\Delta m_\nu^2 = (-15.9 \pm 2.2) \times 10^{-3}\,\mathrm{eV}^2.$$

This result corresponds to not even one single simulation out of 500 fulfilling the KATRIN requirements. With no optimization being possible by raising the overall statistics, the second approach for increasing the percentage of results inside the error budget was found in the finer scanning of the response functions. A finer binning with smaller voltage steps in the measurement yields a smaller neutrino mass square shift. Scanning the response function with voltage steps of 100 mV as planned from −5 eV to 50 eV of surplus energy yields 551 data points. With 10^7 electrons in every voltage step and an expected e-gun rate of 25 kcps this measurement takes an overall time of 20 d for all four column densities. With the condition of keeping the measurement time the same as with the default setting, the number of electrons in every voltage step needed to be adjusted for every size of voltage steps. The best simulation results were achieved with voltage steps of 40 mV and simulating 4×10^6 electrons for every voltage set point. This setting yielded 83.4 % of simulations inside the design report requirements and resulted in a squared neutrino mass shift of

$$\Delta m_\nu^2 = (-3.1 \pm 4.5) \times 10^{-3}\,\mathrm{eV}^2.$$

Nevertheless, scanning the spectrum in steps of 40 mV is very close to the limits of the spectrometer high voltage supply and can cause yet unknown systematic uncertainties and errors, especially considering the reproducibility of the exact same voltage setting for all four column densities needed for the deconvolution process. Improving the deconvolution by scanning the response functions with finer voltage steps caused the smallest simulated neutrino mass shift.
For further minimization of the measurement time in regions that do not have a significant influence on the deconvolution result, investigations with a non-flat measurement time distribution were performed. With reducing the statistics in regions with low sensitivity, measurement time could be saved, but no significant improvement to the neutrino mass shift results could be reached. Interpolating the measurement of the response function at zero column density is a tested way to minimize the measurement time without worsening the neutrino mass square shift incurred. With the interpolation of the zero column density measurement, about 22 % of measurement time can be saved and redistributed into other important regions or into setup and preparation processes.

This method of measuring response functions at multiple column densities and deconvolving the energy loss function was applied and tested during the STS-IIIa commissioning campaign in the fall of 2018. After the needed stability of the e-gun electron rate of 0.05 % was not achieved in the first commissioning measurements, the fast-scanning mode was developed to reduce the impact of the rate drift on the measurement results, by bringing the required measurement time down from roughly 5 d to only 30 min per scan.
Due to the electron rate from the e-gun being lower than expected, the overall number of electrons was not as high as previously demanded. These issues notwithstanding, the measured data was analyzed and deconvolved. As expected from the lower statistics, the resulting energy loss function does not reach the desired precision and therefore the simulated neutrino mass shift does not meet the error budget.
With a strong noise and fluctuation visible in the deconvolved energy loss function, and a resulting squared neutrino mass shift of

$$\Delta m_\nu^2 = (1.435 \pm 0.014)\,\mathrm{eV}^2$$

after applying data corrections considering detector pile-up effects, time synchronization in the data acquisition and normalization of the electron rate using the light intensity, this method is found not to be practicable for a neutrino mass determination.

During the STS-IIIa measurements, another method of measuring the energy loss function of electrons in the gaseous was tested. This time-of-flight method uses a pulsed light source for generating electrons with the e-gun. Recording the time of flight of the electrons through the source and transport section and spectrometers, gives an additional parameter, that can be used for differential energy loss measurements that do not rely on a deconvolution of integral response functions. The advantage of this method, besides the results meeting the KATRIN requirements, is the very fast determination of the energy loss function with only a few hours of measurement needed to determine the energy loss function up to energies of 50 eV with a higher precision compared to the deconvolution process.

The measurements performed with deuterium during STS-IIIa are now repeated with tritium as source gas. Also the time-of-flight method can be further improved besides already fulfilling the KATRIN requirements. With the results obtained from the simulations performed in this thesis, and from the STS-IIIa measurements, it is suggested to use the time-of-flight method for the energy loss function determination in future measurements.

Appendix A

APPENDIX

A.1. Parameters in Default Setup Analysis

Table A.1.: This table shows all parameters used for the check of the results by Hannen and Trost [HHW+17, Tro18] for the simulations and analysis with the default proposed settings and measurement strategy.

Parameter	Value
Number of electrons per voltage step	10^7
Voltage steps	0.1 V
Voltage range	18 550 V to 18 605 V
Threshold in SVD-deconvolution	0.3 %
Number of deconvolutions performed	10^3
Number of Monte Carlo simulations for each deconvolution	10^3
Squared neutrino mass shift result	$(-17.9 \pm 3.7) \times 10^{-3}\,\mathrm{eV}^2$

A.2. Energy Loss Model Comparison to Deconvolution

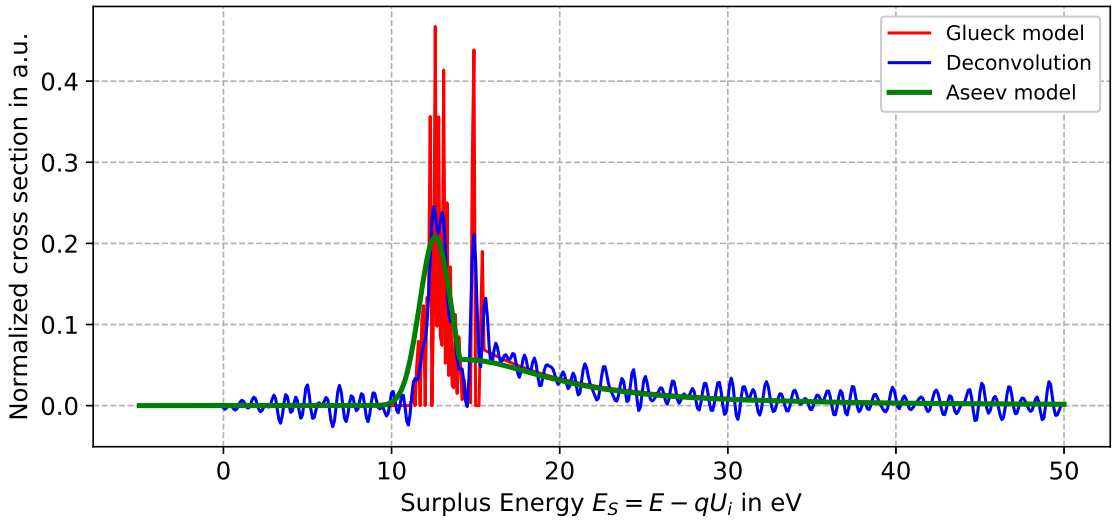

Figure A.1.: Energy Loss Model Comparison to Deconvolution: The Glück and Aseev model in comparison to the deconvolution generated from the default setting simulation.

A.3. NoiseEater

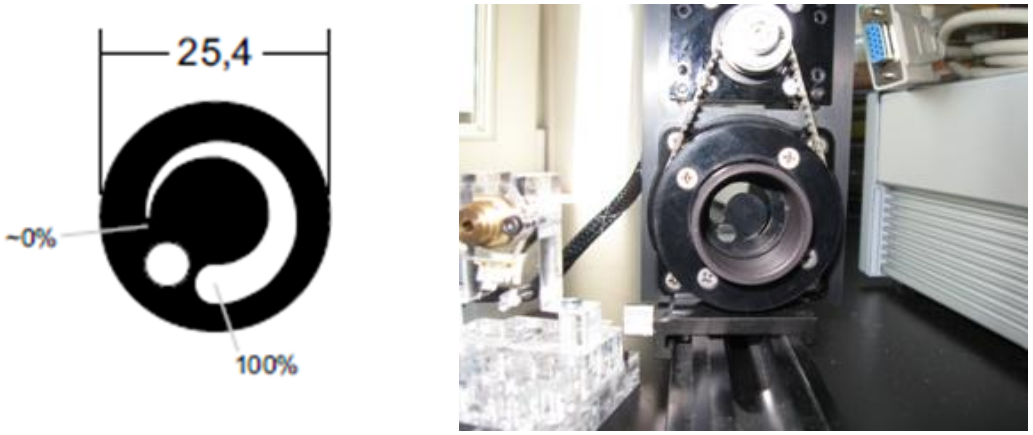

Figure A.2.: The NoiseEater Hardware: Left: Schematic view of the used aperture in the NoiseEater system. Depending on the measured value, the regulation rotates this aperture to increase or decrease cross section of the transmitted beam and thus the light intensity. **Right:** A photograph of the aperture.
Both images are provided by TEM Messtechnik, `http://www.tem-messtechnik.de/noiseeater.htm`.

Table A.2.: NoiseEater Settings: PID and monochromator settings during the presented stability test in Sec. 6.1. The *Reg. P* value gives the PID controller's proportional controlling constant, the *Reg. I* denotes the integral part of the PID controller. The dT gives the regulation time step, i.e. how often the controller acts.

Wavelength	Bandwidth	Reg. P	Reg. I	dT
275 nm	3 nm	10	20	0.03 s

A.4. Optical Test Setup

A.5. Time Synchronization

A.6. Different Tested Measurement Time Distributions

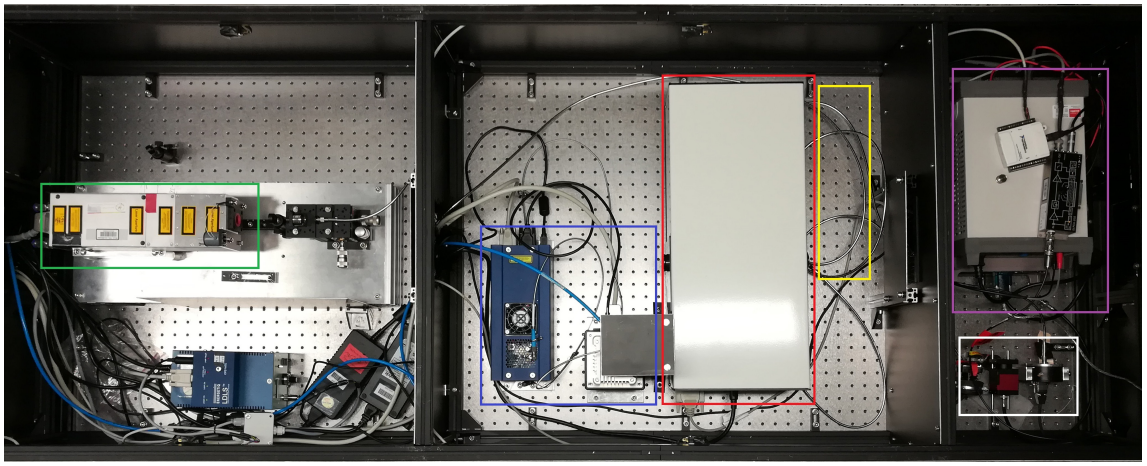

Figure A.3.: Optic Box Test Setup: This Setup is used for the e-gun illumination. The photograph was taken in advance without connection to the KATRIN setup, during optimization measurements. The green box shows the pulsed laser, the LDLS is surrounded in blue. The monochromator for filtering the LDLS spectrum is inside the red box. The light intensity is monitored by the photodiodes in the white box and the amplifier and data acquisition connected to the computer in purple. The NoiseEater System yet is not installed in the picture and is located behind the monochromator in the yellow box. Picture provided by L. Schimpf.

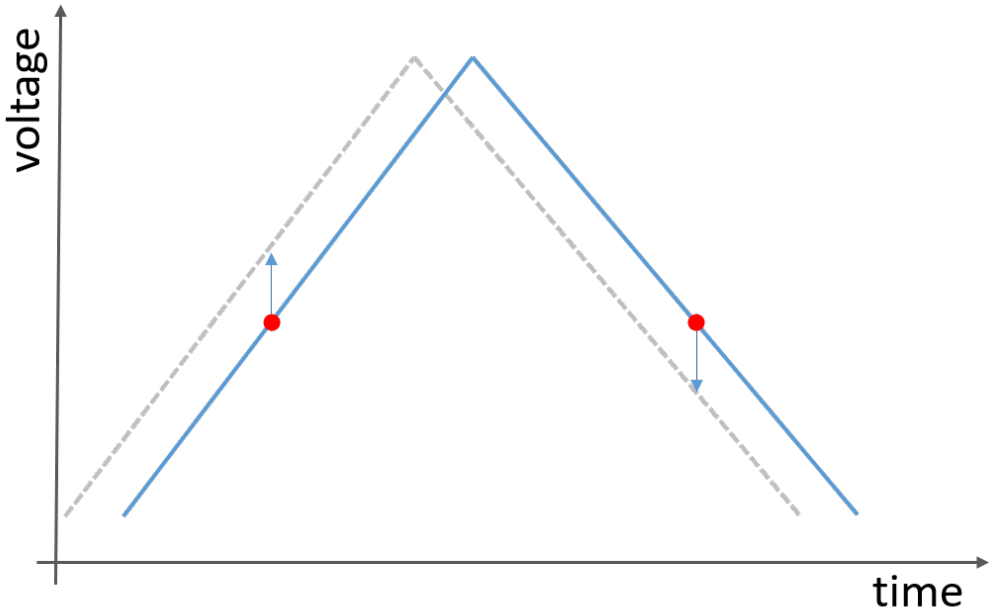

Figure A.4.: Time Synchronization Problem: This graphic shows, how bad time synchronization between the rear section and the focal plane detector can worsen the measured response functions. Assuming, the dashed gray line describes the actual time stamp of the e-gun voltage, and the solid blue line describes the time stamp that is assumed by the synchronization system coupled to the detector. After performing an up and a down scan, the difference between two identical values will be recorded as the double synchronization error. This effect leads to a significant smearing in the data.

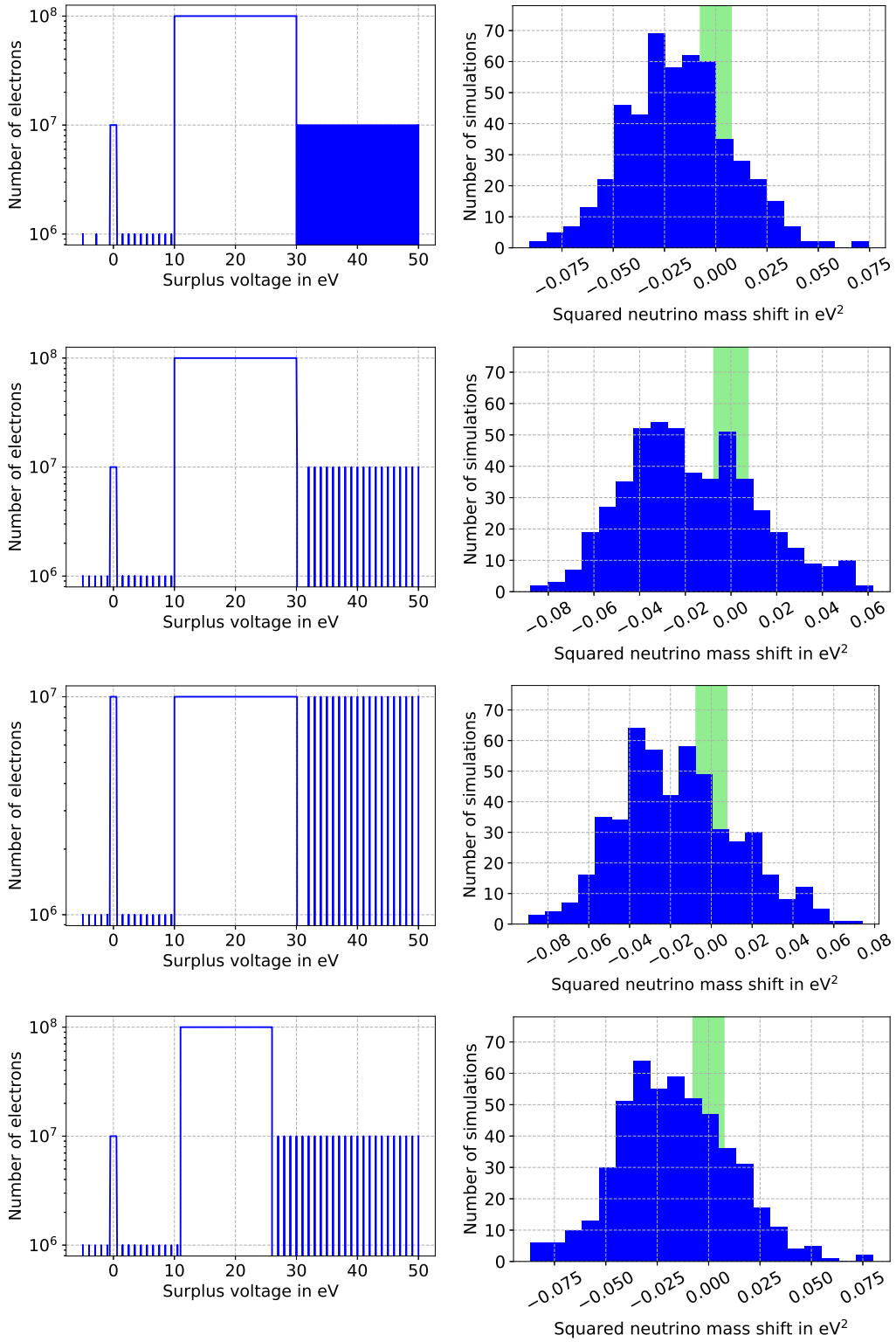

Figure A.5.: The tested measurement time distributions are shown in the left, with their according ensemble test results on the right. Tested setups A, B, C and D.

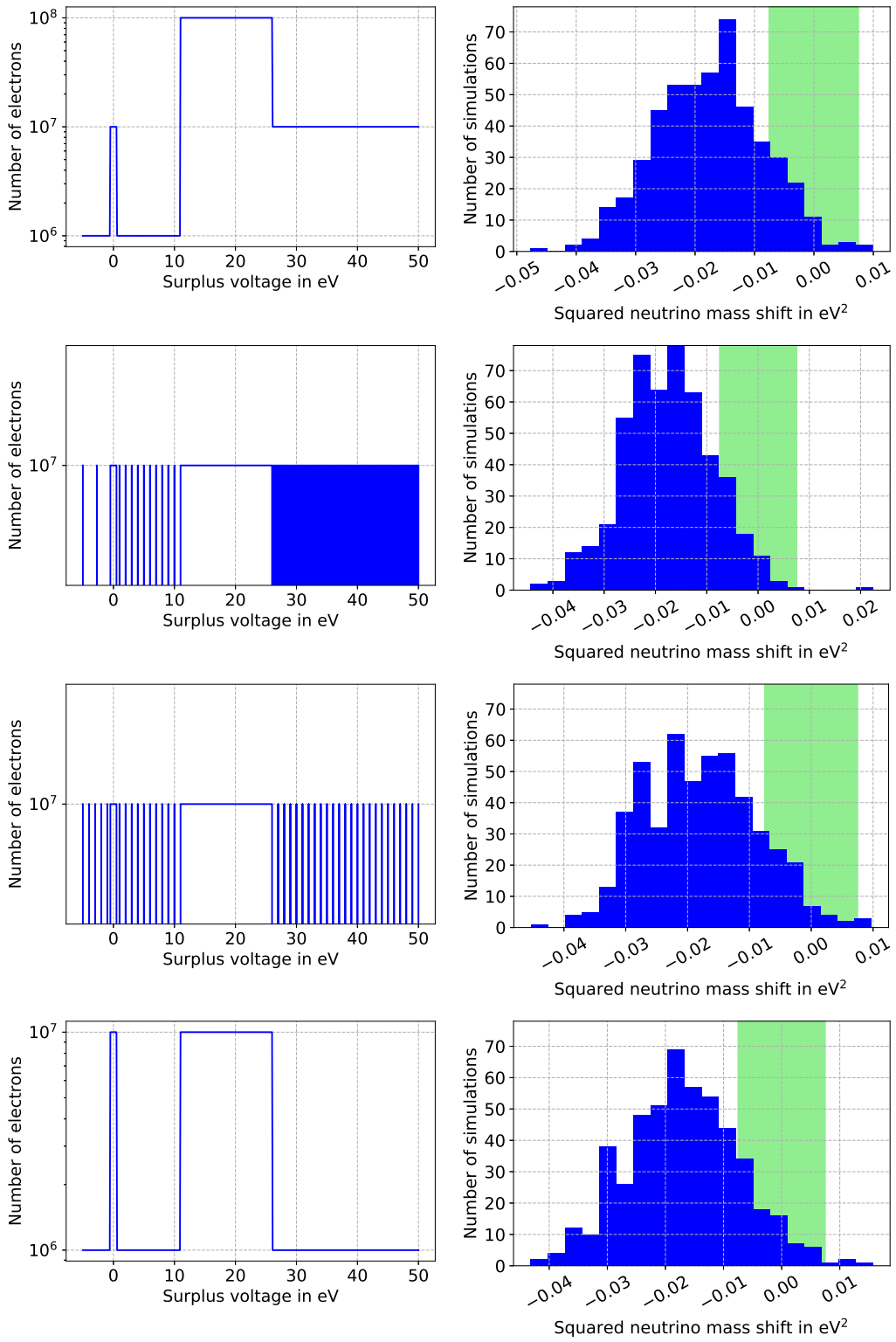

Figure A.6.: The tested measurement time distributions are shown in the left, with their according ensemble test results on the right. Tested setups E, F, G and H.

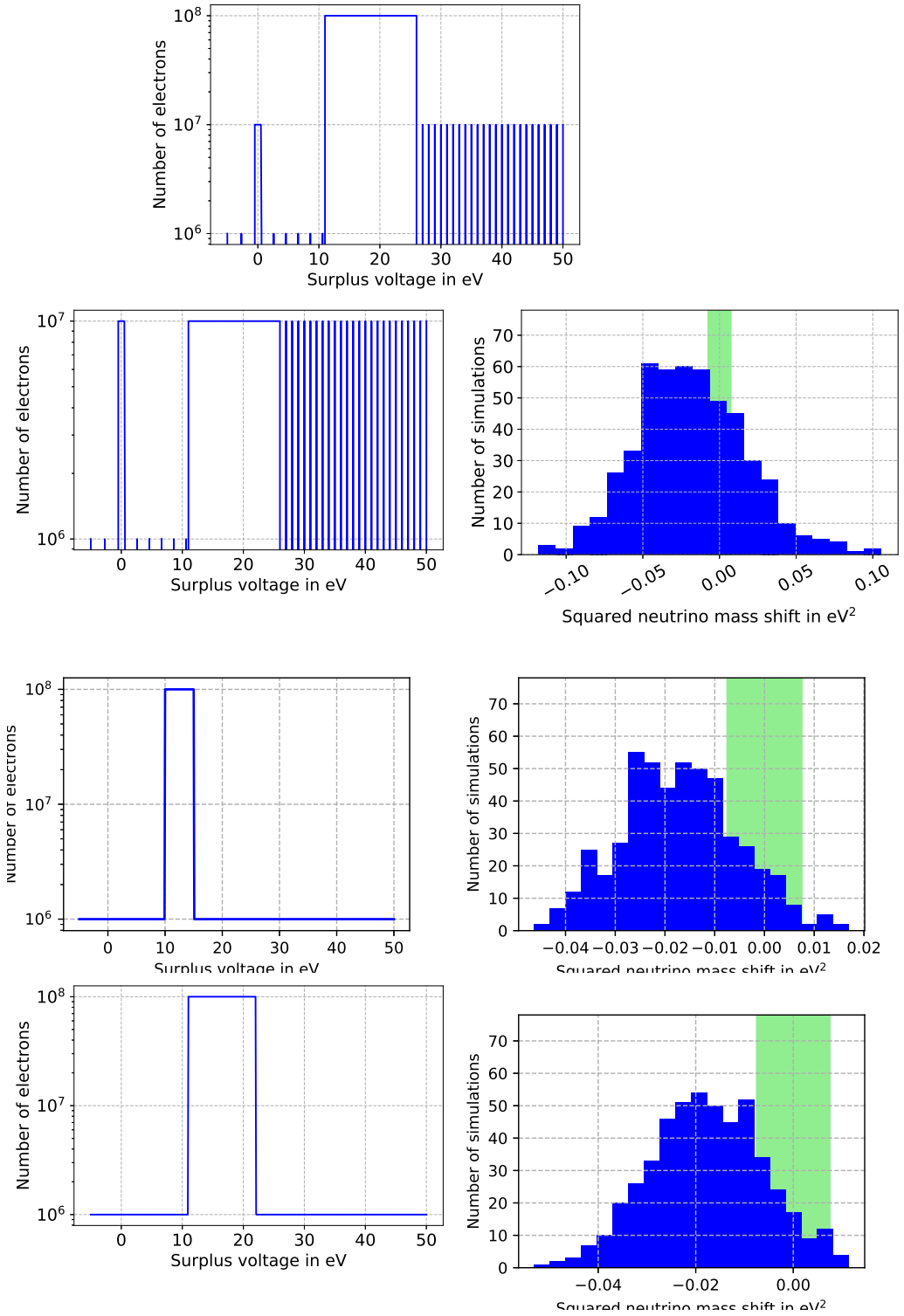

Figure A.7.: The tested measurement time distributions are shown in the left, with their according ensemble test results on the right. Tested setups I, J, K and K+

Table A.3.: This table shows different tested settings for the determination of the optimal measurement time distribution of response for the deconvolution of the energy loss function. The best tested settings are described in more detail in Ch. 5. The Total time is compared to the total time needed for the default settings. Each individual setting is further shown in Fig. A.5 - A.7.

Setup	**Total time**	**Mean Δm_ν^2**	**Width of distribution**
A	× 4.0	$-18.9\,\mathrm{eV}^2$	$24.5\,\mathrm{eV}^2$
B	× 4.0	$-16.9\,\mathrm{eV}^2$	$25.9\,\mathrm{eV}^2$
C	× 0.4	$-16.9\,\mathrm{eV}^2$	$25.4\,\mathrm{eV}^2$
D	× 2.8	$-17.2\,\mathrm{eV}^2$	$26.2\,\mathrm{eV}^2$
E	× 3.2	$-17.5\,\mathrm{eV}^2$	$8.9\,\mathrm{eV}^2$
F	× 0.5	$-17.7\,\mathrm{eV}^2$	$8.4\,\mathrm{eV}^2$
G	× 0.4	$-17.9\,\mathrm{eV}^2$	$9.0\,\mathrm{eV}^2$
H	× 2.8	$-17.0\,\mathrm{eV}^2$	$8.5\,\mathrm{eV}^2$
I	× 2.8	*Fit not converged*	
J	× 0.3	$-18.1\,\mathrm{eV}^2$	$33.2\,\mathrm{eV}^2$
K	× 1.0	$-17.1\,\mathrm{eV}^2$	$11.9\,\mathrm{eV}^2$
K+	× 1.9	$-17.6\,\mathrm{eV}^2$	$11.5\,\mathrm{eV}^2$

BIBLIOGRAPHY

[A+01] Q. R. Ahmad et al. Measurement of the rate of $\nu_e + d \rightarrow p + p + e^-$ interactions produced by ^8b solar neutrinos at the sudbury neutrino observatory. *Phys. Rev. Lett.*, 87:071301, Jul 2001.

[A+12] G. Aad et al. Observation of a new particle in the search for the Standard Model Higgs boson with the ATLAS detector at the LHC. *Physics Letters B*, 716(1):1–29, Sep 2012.

[A+13] M. Agostini et al. Results on Neutrinoless Double-β Decay of ^{76}Ge from Phase I of the GERDA Experiment. *Physical Review Letters*, 111(12), Sep 2013.

[A+16a] Fengpeng An et al. Neutrino physics with JUNO. *Journal of Physics G: Nuclear and Particle Physics*, 43(3):030401, Feb 2016.

[A+16b] M. Arenz et al. Commissioning of the vacuum system of the KATRIN main spectrometer. *Journal of Instrumentation*, 11(04):P04011–P04011, Apr 2016.

[A+16c] R. Arnold et al. Measurement of the double-beta decay half-life and search for the neutrinoless double-beta decay of ^{48}Ca with the nemo-3 detector. *Phys. Rev. D*, 93:112008, Jun 2016.

[A+18a] K. Abe et al. Atmospheric neutrino oscillation analysis with external constraints in super-kamiokande i-iv. *Phys. Rev. D*, 97:072001, Apr 2018.

[A+18b] N. Aghanim et al. Planck 2018 results. VI. Cosmological parameters, 2018.

[A+18c] M. Arenz et al. Calibration of high voltages at the ppm level by the difference of ^{83m}Kr conversion electron lines at the KATRIN experiment. *The European Physical Journal C*, 78(5):368, May 2018.

[A+18d] M. Arenz et al. First transmission of electrons and ions through the KATRIN beamline. *Journal of Instrumentation*, 13(04):P04020–P04020, Apr 2018.

[A+18e] M. Arenz et al. The KATRIN superconducting magnets: overview and first performance results. *Journal of Instrumentation*, 13(08):T08005–T08005, Aug 2018.

[ABB+11] V. N. Aseev, A. I. Belesev, A. I. Berlev, E. V. Geraskin, A. A. Golubev, N. A. Likhovid, V. M. Lobashev, A. A. Nozik, V. S. Pantuev, V. I. Parfenov, A. K. Skasyrskaya, F. V. Tkachov, and S. V. Zadorozhny. Upper limit on the electron antineutrino mass from the troitsk experiment. *Phys. Rev. D*, 84:112003, Dec 2011.

[ABB+15] J.F. Amsbaugh, J. Barrett, A. Beglarian, T. Bergmann, H. Bichsel, L.I. Bodine, J. Bonn, N.M. Boyd, T.H. Burritt, Z. Chaoui, S. Chilingaryan, T.J.

Corona, P.J. Doe, J.A. Dunmore, S. Enomoto, J. Fischer, J.A. Formaggio, F.M. Fränkle, D. Furse, H. Gemmeke, F. Glück, F. Harms, G.C. Harper, J. Hartmann, M.A. Howe, A. Kaboth, J. Kelsey, M. Knauer, A. Kopmann, M.L. Leber, E.L. Martin, K.J. Middleman, A.W. Myers, N.S. Oblath, D.S. Parno, D.A. Peterson, L. Petzold, D.G. Phillips II, P. Renschler, R.G.H. Robertson, J. Schwarz, M. Steidl, D. Tcherniakhovski, T. Thümmler, T.D. Van Wechel, B.A. VanDevender, S. Vöcking, B.L. Wall, K. L. Wierman, J.F. Wilkerson, and S. Wüstling. Focal-plane detector system for the KATRIN experiment. *Nuclear Instruments and Methods in Physics Research Section A: Accelerators, Spectrometers, Detectors and Associated Equipment*, 778:40–60, 2015.

[ABC+17] D. N. Abdurashitov, A. I. Belesev, V. G. Chernov, E. V. Geraskin, A. A. Golubev, G. A. Koroteev, N. A. Likhovid, A. A. Nozik, V. S. Pantuev, V. I. Parfenov, A. K. Skasyrskaya, and S. V. Zadorozhny. Electron scattering on hydrogen and deuterium molecules at 14–25 keV by the "Troitsk nu-mass" experiment. *Physics of Particles and Nuclei Letters*, 14(6):892–899, Nov 2017.

[ABG80] G.P. Arrighini, F. Biondi, and C. Guidotti. A study of the inelastic scattering of fast electrons from molecular hydrogen. *Molecular Physics*, 41(6):1501–1514, Dec 1980.

[ACL05] Kiam Heong Ang, G. Chong, and Yun Li. PID control system analysis, design, and technology. *IEEE Transactions on Control Systems Technology*, 13(4):559–576, Jul 2005.

[Ade14] Ade, P. et al. (Planck Collaboration). Planck 2013 results. XVI. cosmological parameters. *Astronomy and Astrophysics*, 571:66, 2014.

[AEE08] Frank T. Avignone, Steven R. Elliott, and Jonathan Engel. Double beta decay, Majorana neutrinos, and neutrino mass. *Reviews of Modern Physics*, 80(2):481–516, Apr 2008.

[Are16] Arenz, M. et al. (KATRIN Collaboration). Commissioning of the vacuum system of the KATRIN main spectrometer. 2016.

[Bab14] Martin Babutzka. *Design and development for the Rearsection of the KATRIN experiment*. PhD thesis, Karlsruher Institut für Technologie (KIT), 2014.

[Bah64] John N. Bahcall. Solar neutrino cross sections and nuclear beta decay. *Physical Review*, 135(1B):B137–B146, Jul 1964.

[Bar04] J. R. Barnes. Deconvolution of high-resolution spectra as a signal-to-noise ratio enhancement method. *Monthly Notices of the Royal Astronomical Society*, 348(4):1295–1300, Mar 2004.

[BBG+95] A.I. Belesev, A.I. Bleule, E.V. Geraskin, A.A. Golubev, N.A. Golubev, O.V. Kazachenko, E.P. Kiev, Yu.E. Kuznetsov, V.M. Lobashev, B.M. Ovchinnikov, V.I. Parfenov, I.V. Sekachev, A.P. Solodukhin, N.A. Titov, I.E. Yarykin, Yu.I. Zakharov, S.N. Balashov, and P.E. Spivak. Results of the Troitsk experiment on the search for the electron antineutrino rest mass in tritium beta-decay. *Physics Letters B*, 350(2):263–272, May 1995.

[BDL+19] J. Behrens, K. Debowski, B. Lehnert, A. Lokhov, C. Rodenbeck, R. Sack, and L. Schimpf. Report on RS e-gun measurements in STS-IIIa. Internal document, 2019.

[Beh16] Jan D. Behrens. *Design and commissioning of a mono-energetic photoelectron source and active background reduction by magnetic pulse at the KATRIN spectrometers*. PhD thesis, Westfälische Wilhelms-Universität Münster, 2016.

[BEL04] A. BELLERIVE. Review of solar neutrino experiments. *International Journal of Modern Physics A*, 19(08):1167–1179, Mar 2004.

[Ber14] Christoph Berger. *Elementarteilchenphysik : Von den Grundlagen zu den modernen Experimenten*. Springer-LehrbuchSpringerLink : Bücher. Springer Spektrum, Berlin, Heidelberg, 3. Aufl. edition, 2014.

[BP34] H. Bethe and R. Peierls. The "neutrino". *Nature*, 133(3362):532–532, Apr 1934.

[BPT80] G. Beamson, H.Q. Porter, and D.W. Turner. The collimating and magnifying properties of a superconducting field photoelectron spectrometer. *Journal of Physics E: Scientific Instruments*, 13(1):64, 1980.

[BSC19] BSCW: KATRIN Collaboration Database, 2019.

[Cha14] J Chadwick. Intensitätsverteilung im magnetischen Spectrum der β-Strahlen von Radium B + C. *Verhandl. Dtsc. Phys. Ges.*, 16:383, 1914.

[Deu08] Peter Deuflhard. *Numerische Mathematik: Eine algorithmisch orientierte Einführung (de Gruyter Lehrbuch) (German Edition)*. Walter de Gruyter, 2008.

[DGG+62] G. Danby, J.-M. Gaillard, K. Goulianos, L. M. Lederman, N. Mistry, M. Schwartz, and J. Steinberger. Observation of High-Energy Neutrino Reactions and the Existence of Two Kinds of Neutrinos. *Physical Review Letters*, 9:36–44, July 1962.

[DHH68] Raymond Davis, Don S. Harmer, and Kenneth C. Hoffman. Search for Neutrinos from the Sun. *Physical Review Letters*, 20(21):1205–1209, May 1968.

[EHM87] S. R. Elliott, A. A. Hahn, and M. K. Moe. Direct evidence for two-neutrino double-beta decay in Se82. *Physical Review Letters*, 59(18):2020–2023, Nov 1987.

[ET] Inc. Energetiq Technology. *Technical data sheet of the EQ-99X LDLS: http://www.energetiq.com/DataSheets/EQ99X-Data-Sheet.pdf*.

[Fer34] E. Fermi. Versuch einer Theorie der β-Strahlen. *Zeitschrift für Physik*, 88(3–4):161–177, 1934.

[FRS+19] F. Friedel, C. Röttele, L. Schimpf, J. Wolf, G. Drexlin, M. Hackenjos, A. Jansen, M. Steidl, and K. Valerius. Time-dependent simulation of the flow reduction of D2 and T2 in the KATRIN experiment. *Vacuum*, 159:161 – 172, 2019.

[GGS58] M. Goldhaber, L. Grodzins, and A. W. Sunyar. Helicity of neutrinos. *Physical Review*, 109(3):1015–1017, Feb 1958.

[Gro15] Stefan Groh. *Modeling of the response function and measurement of transmission properties of the KATRIN experiment*. PhD thesis, Karlsruher Institut für Technologie (KIT), 2015.

[Har12] Fabian Harms. Assembly and first results of the KATRIN focal-plane detector system at KIT. Diploma thesis, Karlsruher Institut für Technologie (KIT), 2012.

[HHW+17] V. Hannen, I. Heese, C. Weinheimer, A. Sejersen Riis, and K. Valerius. Deconvolution of the energy loss function of the KATRIN experiment. *Astroparticle Physics*, 89:30 – 38, 2017.

[HSM17] Florian Heizmann and Hendrik Seitz-Moskaliuk. The Windowless Gaseous Tritium Source (WGTS) of the KATRIN experiment. *Journal of Physics: Conference Series*, 888(1):012071, 2017.

[Jan15] Alexander Jansen. *The Cryogenic Pumping Section of the KATRIN Experiment - Design Studies and Experiments for the Commissioning.* PhD thesis, Karlsruher Institut für Technologie (KIT), 2015.

[Kaj99] Takaaki Kajita. Atmospheric neutrino results from Super-Kamiokande and Kamiokande — Evidence for ν_μ oscillations. *Nuclear Physics B - Proceedings Supplements*, 77(1):123 – 132, 1999.

[KAT01] KATRIN collaboration. KATRIN: A next generation tritium beta decay experiment with sub-eV sensitivity for the electron neutrino mass, 2001.

[KAT05] KATRIN collaboration. KATRIN design report. *FZKA scientific report*, 7090, 2005.

[KBB+05] Ch Kraus, B. Bornschein, L. Bornschein, J. Bonn, B. Flatt, A. Kovalik, B. Ostrick, E. W. Otten, J. P. Schall, Th Thümmler, and Ch Weinheimer. Final results from phase II of the Mainz neutrino mass search in tritium β decay. *The European Physical Journal C*, 40(4):447–468, Apr 2005.

[KG17] Manuel Klein and Ferenc Glück. Tritium ion blocking and detection in the KATRIN experiment. *Journal of Physics: Conference Series*, 888:012073, Sep 2017.

[KUA+01] K. Kodama, N. Ushida, C. Andreopoulos, N. Saoulidou, G. Tzanakos, P. Yager, B. Baller, D. Boehnlein, W. Freeman, B. Lundberg, J. Morfin, R. Rameika, J.C. Yun, J.S. Song, C.S. Yoon, S.H. Chung, P. Berghaus, M. Kubantsev, N.W. Reay, R. Sidwell, N. Stanton, S. Yoshida, S. Aoki, T. Hara, J.T. Rhee, D. Ciampa, C. Erickson, M. Graham, K. Heller, R. Rusack, R. Schwienhorst, J. Sielaff, J. Trammell, J. Wilcox, K. Hoshino, H. Jiko, M. Miyanishi, M. Komatsu, M. Nakamura, T. Nakano, K. Niwa, N. Nonaka, K. Okada, O. Sato, T. Akdogan, V. Paolone, C. Rosenfeld, A. Kulik, T. Kafka, W. Oliver, T. Patzak, and J. Schneps. Observation of tau neutrino interactions. *Physics Letters B*, 504(3):218–224, Apr 2001.

[LBB+12] S. Lukić, B. Bornschein, L. Bornschein, G. Drexlin, A. Kosmider, K. Schlösser, and A. Windberger. Measurement of the gas-flow reduction factor of the KATRIN DPS2-F differential pumping section. *Vacuum*, 86(8):1126–1133, 2012.

[Lor03] Falko Lorenz. *Lineare Algebra.* Spektrum, Akad. Verl., Heidelberg, 2003.

[Mar18] A. Marsteller. KATRIN Collaboration Meeting 35: Loop Performance, 2018.

[MS86] S. P. Mikheyev and A. Yu. Smirnov. Resonant amplification of ν oscillations in matter and solar-neutrino spectroscopy. *Il Nuovo Cimento C*, 9(1):17–26, Jan 1986.

[Noba] Nobelprize Homepage: Physics Nobelprize 1988: https://www.nobelprize.org/prizes/physics/1988/, accessed 06 Dec, 2018.

[Nobb] Nobelprize Homepage: Physics Nobelprize 2002: https://www.nobelprize.org/prizes/physics/2002/, accessed 02 Mar, 2019.

[Oli16] K.A. Olive. Review of particle physics. *Chinese Physics C*, 40(10):100001, Oct 2016.

[PHM17] Tilman Plehn and Stephanie Hansmann-Menzemer. Lecture: Standardmodel of particle physics, university of heidelberg, 2017.

[PKW64] W.E.F. Pauli, R. Kronig, and V.F. Weisskopf. *Collected scientific papers*. Wiley Interscience, New York, NY, 1964. Offener Brief an die Gruppe der Radioaktiven bei der Gauvereinstagung zu Tübingen (datiert 4. Dez. 1930).

[Pov15] Bogdan Povh. Particles and nuclei : An introduction to the physical concepts, 2015.

[PSB15] Florian Priester, Michael Sturm, and Beate Bornschein. Commissioning and detailed results of KATRIN inner loop tritium processing system at Tritium Laboratory Karlsruhe. *Vacuum*, 116:42–47, Jun 2015.

[RC53] F. Reines and C.L. Cowan. Detection of the free neutrino. *Physical Review*, 92:830–831, 1953.

[Rod] Caroline Rodenbeck. *Time of flight energy loss measurements in the KATRIN neutrino mass experiment*. PhD thesis, Westfälische Wilhelms-Universität Münster. In preparation.

[Rut99] E. Rutherford. VIII. Uranium radiation and the electrical conduction produced by it. *The London, Edinburgh, and Dublin Philosophical Magazine and Journal of Science*, 47(284):109–163, Jan 1899.

[Sac] Rudolph Sack. *Time of flight energy loss measurements in the KATRIN STS-IIIa campaign*. PhD thesis, Westfälische Wilhelms-Universität Münster. In preparation.

[Sac18] R. Sack. KATRIN Collaboration Meeting 34: Rear Section Electron Gun, 2018.

[Sch] Lutz Schimpf. *Integral energy loss measurements in the KATRIN neutrino mass experiment*. PhD thesis, Karlsruher Institut für Technologie. In preparation.

[Sch16] Kerstin Schönung. *Development of a Rear Wall for the KATRIN Rear Section and investigation of tritium compatibility of Rear Section components*. PhD thesis, Karlsruher Institut für Technologie (KIT), 2016.

[Sch18] M. Schloesser. Collaboration Meeting 35: First Tritium Summary, 2018.

[SDL+18] J. Sentkerestiová, O. Dragoun, O. Lebeda, M. Ryšavý, M. Sturm, and D. Vénos. Gaseous ^{83m}Kr generator for KATRIN. *Journal of Instrumentation*, 13(04):P04018–P04018, Apr 2018.

[SDS85] J. J. Simpson, W. R. Dixon, and R. S. Storey. End-point energy of H3 beta decay. *Physical Review C*, 31(5):1891–1895, May 1985.

[SZ01] J. Studnik and M. Zralek. Parametrization of the energy spectrum in the tritium beta decay, 2001.

[Tan16] Tetsuo Tanabe. Characteristics of tritium. In *Tritium: Fuel of Fusion Reactors*, pages 27–48. Springer Japan, Dec 2016.

[Tho97] J. J. Thomson. XL. cathode rays. *The London, Edinburgh, and Dublin Philosophical Magazine and Journal of Science*, 44(269):293–316, Oct 1897.

[Tro18] Nikolaus Trost. *Modeling and measurement of Rydberg-State mediated Background at the KATRIN Main Spectrometer*. PhD thesis, Karlesuher Institut für Technologie, 2018.

[VEŠ16] J. D. Vergados, H. Ejiri, and F. Šimkovic. Neutrinoless double beta decay and neutrino mass. *International Journal of Modern Physics E*, 25(11):1630007, Nov 2016.

[VSD+18] D. Vénos, J. Sentkerestiová, O. Dragoun, M. Slezák, M. Ryšavý, and A. Špalek. Properties of ^{83m}Kr conversion electrons and their use in the KATRIN experiment. *Journal of Instrumentation*, 13(02):T02012–T02012, Feb 2018.

[Wan13] Nancy Wandkowsky. *Study of background and transmission properties of the KATRIN spectrometers.* PhD thesis, Karlsruher Institut für Technologie (KIT), 2013.

[Wei18] Christian Weinheimer. Direct determination of the energy loss spectrum by applying a single time-of-flight cut, 2018. Internal Document.

[Wik] KATRIN Wiki: Resources: https://neutrino.ikp.kit.edu/katrin/index.php/Resources, accessed on 23 Nov, 2018.

[Wol78] L. Wolfenstein. Neutrino oscillations in matter. *Physical Review D*, 17(9):2369–2374, May 1978.

[Zac15] Michael Zacher. *High-field electrodes design and an angular-selective photoelectron source for the KATRIN spectrometers.* PhD thesis, Westfälische Wilhelms-Universität Münster, 2015.

[Zub12] Kai Zuber. *Neutrino physics.* MyiLibrarySeries in high energy physics, cosmology, and gravitation. CRC Press, Taylor & Francis Group, Boca Raton, second edition, 2012.

ACKNOWLEDGMENT

This last page is dedicated to all the people who made this thesis possible and helped me throughout the last months and years.
Without the support of all the people at the institute but also in my private life, I could not write this thesis and look back on the time of my studies. In general I want to thank everyone who supported me during the last years but of course especially in the past twelve months at ETP. In particular:

- First of all I want to express my deepest thanks to Prof. Dr. Guido Drexlin for accepting me as a master's student in his KATRIN group at KIT, giving me the possibility to spend a very interesting and educating year working on a great project.
- Also greatest thanks to Prof. Dr. Ulrich Husemann for agreeing to act as second reviewer of this thesis.
- Special thanks go to Lutz Schimpf, for his supervision and for answering many questions about the topic of energy loss. Also for the great support during my first weeks at KATRIN and for various inspiring conversations during the work and writing of this thesis, as well as for proofreading these pages.
- Dr. Kathrin Valerius and Dr. Hendrik Seitz-Moskaliuk for proofreading this thesis, and for their many helpful comments also related to general KATRIN topics.
- Florian Heizmann and Manuel Klein for sharing the office and making the daily work very pleasant.
- Prof. Dr. Christian Weinheimer for the invitation to Münster for a very interesting and fruitful week of analysis work at WWU.
- The whole KATRIN group at KIT for the great and enjoyable activities in and outside the office work, as well as many helpful discussions, but also the whole KATRIN collaboration for making such a complex experiment work.
- Last but not least I would like to thank my family and friends for their support during my studies, and especially in this final phase recorded in this thesis.